Measurement of the Branching Fractions of the Tau into Leptons with the L3 Detector at LEP

D I S S E R T A T I O N

zur Erlangung des akademischen Grades

d o c t o r r e r u m n a t u r a l i u m

(Dr. rer. nat.)

im Fach Physik

eingereicht an der

Mathematisch-Naturwissenschaftlichen Fakultät I

der Humboldt-Universität zu Berlin

von

Frank Ziegler

geboren am 2. Juli 1967 in Berlin

Präsident der Humboldt-Universität zu Berlin
Prof. Dr. Dr. h.c. Hans Meyer

Dekan der Mathematisch-Naturwissenschaftlichen Fakultät I
Prof. Dr. Jürgen Rabe

Gutachter: 1. Prof. Dr. Thomas Hebbeker
2. Prof. Dr. Martin Pohl
3. Prof. Dr. Paul Söding

Tag der mündlichen Prüfung: 20.04.2000

Zusammenfassung

In dieser Arbeit werden die Zerfälle des schwersten bekannten Leptons, des Tau, in die beiden leichteren Leptonen, Elektron oder Muon, untersucht. Die durch Elektron-Positron-Annihilation am LEP-Speicherring entstehenden Tau-Paare werden ausgewertet, um die Verzweigungsverhältnisse $B_{l=e,\mu} = \frac{\Gamma(\tau \to \nu_\tau l \bar{\nu}_l)}{\Gamma_{tot}}$ zu bestimmen. Die Analyse erfolgt für die gesamte bei LEP I mit dem L3-Detektor auf der Z-Resonanz aufgezeichnete Datenmenge. Aus über 160000 selektierten Tau-Zerfällen werden die leptonischen Zerfälle identifiziert und die leptonischen Verzweigungsverhältnisse gemessen:

$$\begin{aligned} B_e &= (17.806 \pm 0.104_{stat} \pm 0.076_{sys})\ \% \\ B_\mu &= (17.342 \pm 0.110_{stat} \pm 0.067_{sys})\ \% \ . \end{aligned}$$

Das daraus bestimmte Verhältnis der Kopplungen von Elektron und Muon im geladenen schwachen Strom

$$\frac{g_\mu}{g_e} = 1.0007 \pm 0.0051$$

stimmt ausgezeichnet mit der aus dem Standardmodell entsprechend der angenommenen Lepton-Universalität erwarteten Gleichheit der Kopplungen überein. Durch Vergleich der Verzweigungsverhältnisse mit der im Standardmodell berechneten leptonischen Zerfallsbreite $\Gamma(\tau \to \nu_\tau l \bar{\nu}_l)$ wird ein Wert für die Tau-Lebensdauer bestimmt, der mit der direkten Messung sehr gut verträglich ist. Unter Hernahme der direkten L3-Messung der Tau-Lebensdauer wird die Universalität der Kopplungen am $Wl\bar{\nu}_l$-Vertex für g_τ/g_μ und g_τ/g_e mit einer Genauigkeit von 6 ‰ bestätigt.

Aus dem Verhältnis der hadronischen zur leptonischen Zerfallsbreite des Tau wird die Kopplungskonstante der starken Wechselwirkung gemessen:

$$\alpha_s(m_\tau) = 0.324 \pm 0.009_{Experiment} \pm 0.017_{Theorie} \ .$$

Der daraus zur Masse des Z-Bosons extrapolierte Wert

$$\alpha_s(m_{\mathrm{Z}}) = 0.1191 \pm 0.0009_{Experiment} \pm 0.0019_{Theorie}$$

ist in exzellenter Übereinstimmung mit den direkten Messungen und bestätigt die von der QCD vorhergesagte Energieabhängigkeit der Kopplungskonstante.

Die Masse m_{ν_τ} des Tau-Neutrinos läßt sich aus dem Vergleich der gemessenen mit einer für m_{ν_τ} berechneten leptonischen Zerfallsbreite begrenzen auf:

$$m_{\nu_\tau} < 107 \text{ MeV} \qquad \text{(mit 95\% Wahrscheinlichkeit)} \ .$$

Das Verhältnis aus B_μ und B_e ist sensitiv auf die Kopplungen an ein geladenes Higgs-Dublett und liefert eine Grenze für die Masse des geladenen Higgs-Bosons von

$$m_{H^\pm} > 1.0 \tan\beta \text{ GeV} \qquad \text{(mit 95\% Wahrscheinlichkeit)} \ .$$

Hierbei ist $\tan\beta$ das Verhältnis der Vakuumerwartungswerte beider Higgs-Dubletts.

Abstract

This is a study of the decays of the heaviest known lepton, the τ, into the two lighter leptons, electron or muon. From τ pairs produced at the LEP storage ring in electron-positron annihilation the leptonic branching fractions of the τ, $B_{l=e,\mu} = \frac{\Gamma(\tau \to \nu_\tau l \bar{\nu}_l)}{\Gamma_{tot}}$, are measured. The analysis was performed using the full LEP I data sample collected with the L3 detector at centre-of-mass energies around the Z mass. Within about 160000 selected τ decays the leptonic decays were identified and the branching fractions are measured as:

$$\begin{aligned} B_e &= (17.806 \pm 0.104_{stat} \pm 0.076_{sys})\% \\ B_\mu &= (17.342 \pm 0.110_{stat} \pm 0.067_{sys})\% \ . \end{aligned}$$

It is used to test the $e - \mu$ universality in the weak charged current couplings:

$$\frac{g_\mu}{g_e} = 1.0007 \pm 0.0051 \ .$$

The ratio of the couplings of electron and muon is in excellent agreement with the Standard Model assumption of 1. Using the Standard Model prediction for the leptonic decay width, $\Gamma(\tau \to \nu_\tau l \bar{\nu}_l)$, the τ lifetime is determined, precisely confirming direct measurements. Together with the L3 measurement of the τ lifetime the universality in the couplings at the W$l\bar{\nu}_l$ vertex is verified for g_τ/g_μ and g_τ/g_e at a level of 6 per mille.

The ratio of hadronic to leptonic τ decay width, R_τ, is calculated from the measured leptonic branching fractions, and a value of the QCD coupling constant is extracted:

$$\alpha_s(m_\tau) \ = \ 0.324 \ \pm \ 0.009_{exp} \ \pm \ 0.017_{theory} \ .$$

The value obtained by evolving $\alpha_s(m_\tau)$ to the Z mass,

$$\alpha_s(m_{\rm Z}) \ = \ 0.1191 \ \pm \ 0.0009_{exp} \ \pm \ 0.0019_{theory} \ ,$$

agrees very well with direct measurements and confirms the predicted running of α_s.

An upper limit for the mass of the τ neutrino, m_{ν_τ}, is estimated from a comparison of the measured leptonic τ decay rate to a prediction as a function of m_{ν_τ}:

$$m_{\nu_\tau} \ < \ 107 \text{ MeV} \qquad \text{(at 95\% confidence level)} \ .$$

The ratio of B_μ to B_e is sensitive to the couplings to a charged Higgs doublet and allows to set a limit on the mass of the charged Higgs boson

$$m_{H^\pm} \ > \ 1.0 \tan\beta \text{ GeV} \qquad \text{(at 95\% confidence level)} \ ,$$

where $\tan\beta$ is the ratio of the vacuum expectation values of the two Higgs doublets.

CONTENTS

Introduction 1

Part I Theoretical Framework and Experimental Conditions 3

1. The Tau Lepton in the Standard Model 5

1.1 The Standard Model of Particle Physics 5

1.2 The Electroweak Standard Model 7

1.3 The Tau as Standard Model Laboratory 11

1.4 Tau Pair Production 14

1.5 Tau Leptonic Decay 16

1.6 Physics Interest in Tau Leptonic Branching Fractions 19

2. The L3 Experiment at LEP 25

2.1 The Large Electron Positron Collider 25

2.2 The L3 Detector 27

2.2.1 The Central Tracking System 29

2.2.2 The Electromagnetic Calorimeter 32

2.2.3 The Scintillation Counters 34

2.2.4 The Hadron Calorimeter 34

2.2.5 The Muon Spectrometer 35

2.2.6 The Luminosity Monitor 37

2.2.7 The L3 Trigger System 37

3. Physics Capabilities in L3 41

3.1 Event Reconstruction 41
3.2 Particle Identification 43
3.3 Detector Simulation 44

Part II Measurement of Tau Leptonic Branching Fractions 47

4. Method of Measurement 49
4.1 Tau Leptonic Branching Fraction Measurement at LEP 49
4.2 Single Hemisphere Tagging 52

5. Selection of the Tau Sample 55
5.1 Dilepton Preselection 56
5.2 Selection of the Tau Sample 56
5.2.1 Principles of the Tau Selection 56
5.2.2 Identification of Tau Pair Events 60
5.2.3 Cosmic Muon Background 62
5.2.4 Background from $e^+e^- \to e^+e^-$ 63
5.2.5 Background from $e^+e^- \to \mu^+\mu^-$ 65
5.2.6 Background from Two-Photon Interactions 68
5.2.7 Background from $e^+e^- \to q\bar{q}$ 71
5.3 Summary for the Tau Selection 71

6. Identification of Leptonic Tau decays 75
6.1 Lepton Identification 75
6.1.1 Electron Identification 75
6.1.2 Muon Identification 80
6.2 Identification of Leptonic Tau Decays 83
6.2.1 Identification of $\tau \to e\bar{\nu}\nu$ 83
6.2.2 Identification of $\tau \to \mu\bar{\nu}\nu$ 87

7. The Measurement 89

7.1 Background Measurements 89
7.1.1 Background Measurements for the Tau Sample 89
7.1.2 Background Measurements for the Leptonic Samples 93
7.2 Identification Efficiencies 93
7.2.1 Electron Identification Efficiency 93
7.2.2 Muon Identification Efficiency 98
7.3 Systematic Studies 105
7.3.1 Systematics for the Background Measurements 105
7.3.2 Identification of Leptonic Tau Decays 108
7.3.3 Trigger Efficiency 108
7.3.4 Bias due to Tau Selection 109
7.3.5 Hadron Misidentification 109
7.3.6 Systematics from Polarisation 110
7.3.7 Momentum Range Restriction 110
7.4 Summary for Data Analysis 110
7.4.1 Tau Selection 111
7.4.2 Identification of Leptonic Tau Decays 111
7.4.3 Systematic Uncertainties 112

8. Results 119
8.1 Results 119
8.2 Test of Lepton Universality 120
8.3 Measurement of α_s 126
8.4 Mass of the Tau Neutrino 127
8.5 Mass of a charged Higgs Boson 127
8.6 Comparison with other Experiments 129

9. Summary and Conclusion 131

INTRODUCTION

The endeavour to study nature is an outstanding characteristic of the human race. This curiosity is aimed to understand how the material world is constructed and finally to give answer to fundamental questions of our existence. By searching for the building blocks of matter and the basic laws of nature, elementary particle physics provides a unique tool to understand the fundamental structure of matter. Together with cosmology it gives an idea of how the universe began and evolved to its present state, and hopefully will anticipate its future development.

Today matter is known to consist of a limited, small number of fermions, ordered in three families, which are linked by four different forces. A consistent model, the Standard Model, describes three of these forces by boson exchange. The strength of the interaction, the coupling between a particle and a boson, is given by coupling constants. The couplings do not depend on the fermion family, they are universal. The measurement presented here provides to test the validity of this assumption in the charged sector of electroweak interactions.

The τ is the heaviest known lepton. It decays into the lighter leptons and also into hadrons. Therefore, the τ provides a unique laboratory to explore the electroweak and strong interaction. The rate of the leptonic τ decays, $\tau \to e\bar{\nu}\nu$ and $\tau \to \mu\bar{\nu}\nu$, is predicted by the Standard Model with extremely small theoretical uncertainties and depends on the couplings of electron and muon to the intermediate charged vector boson W. Thus, the measurement of the leptonic branching fractions allows to test unambiguously the universality of the couplings of e and μ to the W. Combined with the knowledge about mass and lifetime of τ and μ, it probes the weak charged current couplings of all three charged leptons.

Further motivation to measure the leptonic branching fractions comes from hadronic decays of the τ. Due to large QCD corrections the hadronic decays are sensitive to the strong coupling constant α_s, which can be extracted from the ratio of the hadronic decay width to the leptonic decay width.

This thesis describes the measurement of the τ leptonic branching fractions with the L3 detector at the Large Electron Positron collider (LEP), which was operated between 1989 and 1995 at centre-of-mass energies around the Z resonance. At these energies of about 91 GeV the $e^+e^- \rightarrow \tau^+\tau^-$ cross section is enhanced. The large number of produced τ pairs together with the good conditions provided by LEP permits to measure the τ leptonic branching fractions with high precision.

The thesis consists of two parts. In the first part the theoretical framework and experimental conditions for the measurement will be explained. The Standard Model is introduced and the τ lepton will be described. The leptonic decay rates and the dependence on the couplings as calculated in the Standard Model will be given. Furthermore, the extraction procedure of α_s will be shown. With the increased precision of recent measurements possible new physics contributions to the τ decay amplitudes are studied. The sensitivity of the leptonic τ decay rate to a possible massive τ neutrino will be demonstrated as well as the sensitivity to a charged Higgs boson. Then, the experimental situation, including the capabilities of the L3 detector for particle physics will be described.

The second and main part is devoted to the measurement of the leptonic branching fractions. First, the method of the measurement will be developed. Then the selection of the event samples is explained in detail, followed by a careful study of the event content in these samples. Finally, the results will be presented and discussed within the context of part I.

Throughout this thesis the convention $\hbar = c = 1$ is used in all calculations, unless specifically stated otherwise.

Part I

THEORETICAL FRAMEWORK AND EXPERIMENTAL CONDITIONS

Chapter 1

THE TAU LEPTON IN THE STANDARD MODEL

In this chapter the τ lepton will be introduced as one of the fundamental particles of elementary matter. The current theory, which describes the structure and the interactions of elementary particles, hence also the production and decay of τ leptons, will be presented briefly. Finally the possibilities for testing the Standard Model by a precision measurement of the τ leptonic branching fractions will be explained.

1.1 The Standard Model of Particle Physics

Generally, four kinds of interactions are established: strong, electromagnetic, weak and gravitational. Except for the gravitation they are described by the Standard Model of particle physics [1–3]. In its context the basic constituents of matter are particles of half integer spin, the *fermions*. They are grouped into three families with similar properties with the exception of their mass (table 1.1). A part of the fermions, the *quarks*, do undergo strong interaction, in contrast to the remaining, the *leptons*. The forces between the fermions are generated by the exchange of integer spin particles, the *bosons* (table 1.2).

The Standard Model is the result of combining the knowledge about elementary particles and their interactions into a consistent theory. It answers many of the questions of the structure and stability of matter and describes most of the observed microscopical phenomena. All experiments have confirmed its detailed predictions so far. The Standard Model consists of the *Standard Model of electroweak interactions*, which describes electromagnetism and the weak force in a unified way, and a theory for the strong interactions, *quantum chromodynamics* (QCD).

Both theories are impressive implementations of the concept of gauge invariance, which

Family	**Lepton**	Charge [e]	Mass [MeV]	**Quark**	Charge [e]	Mass [MeV]
1.	ν_e	0	$< 15 \times 10^{-6}$	u	2/3	1.5 - 5
	e^-	-1	0.510999	d	-1/3	3 - 9
2.	ν_μ	0	< 0.190	c	2/3	1000 - 1400
	μ^-	-1	105.6584	s	-1/3	60 - 170
3.	ν_τ	0	< 18.2	t	2/3	168600 - 179000
	τ^-	-1	$1777.05^{+0.29}_{-0.26}$	b	-1/3	4100 - 4400

Tab. 1.1: Fundamental fermions in the Standard Model. Masses and mass limits are taken from [4]. Since quarks are confined inside hadrons, the quark masses must be determined indirectly through their influence on hadron properties. Therefore their mass values are model depended. Note, that the t quark is sufficiently heavy that its decay is expected to occur before hadronisation.

Boson	Charge [e]	Spin	Mass [GeV]	Interaction
γ	0	1	0	Electromagnetic
$W^\pm$	± 1	1	80.369 ± 0.061	Weak
Z	0	1	91.188 ± 0.007	
g	0	1	0	Strong
G	0	2	0	Gravitational

Tab. 1.2: Gauge bosons of the Standard Model and their masses [4], together with the proposed graviton G.

is based on two principal achievements of physics. One is the experience that the reveal of a symmetry, i.e. of the invariance of a system under a transformation, is very helpful to understand the underlying laws of nature. The other is the insight that a symmetry is always connected with a conserved physical quantity.

For the field of particle physics a special symmetry, the invariance under a local gauge transformation, introduces a gauge field and intrinsicly provides the interaction between fermions and the gauge field. The gauge theories of the Standard Model are renormalisable [5, 6], so that finite and unique predictions to all order of perturbation theory with a finite set of input quantities are obtained.

1.2 The Electroweak Standard Model

The theory of electromagnetic interactions, *Quantum Electrodynamics* (QED), was the first renormalisable quantum field theory. Its predictions, most notably the Lamb shift in atomic spectra, and the anomalous magnetic moments of the electron and muon, were confirmed by measurements impressively [7]. Because of the great success of QED, it became the paradigm for theories of the strong and the weak forces. For the QED, charge conservation is ensured by requesting that the Lagrangian is invariant under the local phase transformations of the particle field. These gauge transformations belong to the symmetry group $U(1)$.

In generalisation of QED the electroweak interaction is based on the symmetry group $SU(2)_L \otimes U(1)_Y$. The group $SU(2)_L$ contains the weak charged current, which couples to left-handed fermions only. The generators of the $SU(2)_L$ group are the three components of the weak isospin $\vec{T}$ which correspond to a gauge field triplet W^i_μ. The $U(1)_Y$ symmetry is generated by the weak hypercharge Y, which is related to the electric charge Q and the third component of the weak isospin T_3 by

$$Q = T_3 + \frac{Y}{2} \,, \tag{1.1}$$

and corresponds to a single gauge field B_μ.

The fermion structure of the Electroweak Standard Model is summarised in Table 1.3. The left-handed fermions are arranged as doublets while right-handed fermions form singlets. The fermion fields ψ in the Lagrangian appear as combinations of the left-handed (ψ_L) and right-handed (ψ_R) fields:

$$\psi_L \equiv \frac{1-\gamma^5}{2}\psi \qquad \psi_R \equiv \frac{1+\gamma^5}{2}\psi \qquad \psi = \psi_L + \psi_R \,. \tag{1.2}$$

Fermions	Generations	Q	Y	T_3
Leptons	$\begin{pmatrix} \nu_e \\ e^- \end{pmatrix}_L$ $\begin{pmatrix} \nu_\mu \\ \mu^- \end{pmatrix}_L$ $\begin{pmatrix} \nu_\tau \\ \tau^- \end{pmatrix}_L$	0 -1	-1 -1	$+1/2$ $-1/2$
	e^-_R μ^-_R τ^-_R	-1	-2	0
Quarks	$\begin{pmatrix} u \\ d' \end{pmatrix}_L$ $\begin{pmatrix} c \\ s' \end{pmatrix}_L$ $\begin{pmatrix} t \\ b' \end{pmatrix}_L$	$+2/3$ $-1/3$	$+1/3$ $+1/3$	$+1/2$ $-1/2$
	u_R c_R t_R	$+2/3$	$+4/3$	0
	d'_R s'_R b'_R	$-1/3$	$-2/3$	0

Tab. 1.3: The electric charge, hypercharge and weak isospin assignments for the fermions in the Electroweak Standard Model. The prime at the left-handed down-type quarks indicates weak interactcion eigenstates, which are mixings of the mass eigenstates. The mixing is described by the unitary *Cabbibo-Kobayashi-Maskawa* (CKM) mixing matrix [8,9].

The interactions between the fermions and the gauge fields enter through the covariant derivative:

$$\mathcal{D}_\mu = \partial_\mu + ig_1 Y B_\mu + ig_2 \frac{\tau_i}{2} \cdot W^i_\mu \,, \tag{1.3}$$

where g_1, g_2 are the coupling constants for $U(1)_Y$, $SU(2)_L$, respectively. The matrix representation of the generators $\tau_i \equiv 2\, T_i$ are the Pauli spin matrices.

At this stage all bosons and fermions are massless, a contradiction to the observation. This problem is solved by the Higgs mechanism [10,11].

In the minimal Higgs mechanism one complex scalar doublet field is introduced:

$$\Phi = \begin{pmatrix} \phi^0 \\ \phi^- \end{pmatrix} \,. \tag{1.4}$$

Its components have the same quantum numbers as the left-handed lepton doublets, except for the lepton number. The Higgs Lagrangian is then given by

$$\mathcal{L}_{Higgs} = (\mathcal{D}^\mu \Phi)^\dagger (\mathcal{D}_\mu \Phi) - V(\Phi^\dagger \Phi) \,. \tag{1.5}$$

The $SU(2)_L$ invariant potential of the Higgs field

$$V = \mu^2 \Phi^\dagger \Phi + \lambda (\Phi^\dagger \Phi)^2 \tag{1.6}$$

is symmetric around $\phi = 0$, in that way respecting the gauge symmetry. For the vacuum as the state with the lowest energy the potential should be minimal. A non-trivial minimum is at

$$|\Phi_0|^2 = -\frac{1}{2}\frac{\mu^2}{\lambda} \equiv \frac{1}{2}\nu^2, \tag{1.7}$$

where $\nu/\sqrt{2}$ is the vacuum expectation value of the Higgs field.

Choosing a specific vacuum state breaks the symmetry $SU(2)_L \otimes U(1)_Y$. The excitations around that ground state are parametrised by the new field Φ'

$$\Phi \rightarrow \Phi' = \frac{1}{\sqrt{2}} \begin{pmatrix} 0 \\ \nu + H \end{pmatrix} . \tag{1.8}$$

The Higgs field H corresponds to a massive particle, the spin-zero Higgs boson, which has not been observed up to now. Its mass is given by $m_H = \sqrt{2\lambda}\mu$. The actual lower mass limit for the scalar neutral Higgs boson derived from direct searches is 102.6 GeV [12].

Replacing Φ effectively by Φ' results in explicit mass terms in the Lagrangian. The fields of the observed massive charged gauge bosons $\mathrm{W}^\pm$ are identified as combinations of the gauge fields W^1_μ and W^2_μ:

$$W^\pm_\mu = \frac{1}{\sqrt{2}}(W^1_\mu \mp i W^2_\mu) . \tag{1.9}$$

From the mixing of the neutral fields W^3_μ and B_μ the massless gauge boson field of the photon is obtained:

$$A_\mu = W^3_\mu \sin\theta_W + B_\mu \cos\theta_W . \tag{1.10}$$

The orthogonal combination

$$Z_\mu = W^3_\mu \cos\theta_W - B_\mu \sin\theta_W \tag{1.11}$$

represents the massive neutral gauge boson, the Z.

The mixing of the neutral fields is parametrised by the *weak mixing angle* θ_W, which is given in terms of the electroweak couplings g_1 and g_2:

$$\sin\theta_W \equiv \frac{g_1}{\sqrt{g_1^2 + {g_2}^2}} \qquad \cos\theta_W \equiv \frac{g_2}{\sqrt{g_1^2 + {g_2}^2}} . \tag{1.12}$$

Since the masses of the gauge bosons W and Z are given by:

$$m_{\mathrm{W}} = \frac{\nu}{2} g_2 \tag{1.13}$$

$$m_{\mathrm{Z}} = \frac{\nu}{2} \sqrt{{g_1}^2 + {g_2}^2} \,, \tag{1.14}$$

the weak mixing angle relates their masses by

$$\cos\theta_W = \frac{m_{\mathrm{W}}}{m_{\mathrm{Z}}} \,. \tag{1.15}$$

The fermion masses are generated due to the interaction of the fermions with the Higgs field, whose strength is proportional to the mass.

The Lagrangian describing electroweak interactions of fermions in terms of the gauge fields, $W_\mu^\pm$, Z_μ and A_μ, becomes

$$\mathcal{L}_{int} = -ig_2(W_\mu^+ J_{CC+}^\mu + W_\mu^- J_{CC-}^\mu) - \sqrt{{g_1}^2 + {g_2}^2} Z_\mu J_{NC}^\mu - \frac{g_1 g_2}{\sqrt{{g_1}^2 + {g_2}^2}} A_\mu J_{EM}^\mu \,, \tag{1.16}$$

where the electric charge, e, is expressed in dependence of the coupling constants as:

$$\mathrm{e} = \frac{g_1 g_2}{\sqrt{{g_1}^2 + {g_2}^2}} \,. \tag{1.17}$$

The charged weak, neutral weak and electromagnetic interaction components of the Lagrangian are represented by the related currents J_{CC}, J_{NC} and J_{EM}.

Using the following definitions for hypercharge, left-handed charged and neutral weak currents:

$$J_Y^\mu = \overline{\psi} \gamma^\mu Y \psi \tag{1.18}$$

$$J_\pm^\mu = \overline{\psi}_L \gamma^\mu \tau_\pm \psi_L \tag{1.19}$$

$$J_3^\mu = \overline{\psi}_L \gamma^\mu \frac{\tau_3}{2} \psi_L \,, \tag{1.20}$$

with

$$\tau_\pm = \frac{1}{2}(\tau_1 \pm i\tau_2), \tag{1.21}$$

the fermionic electroweak currents can be written as:

$$\begin{aligned} J_{EM}^\mu &= J_3^\mu + J_Y^\mu &&= Q\overline{\psi}\gamma^\mu\psi \\ J_{NC}^\mu &= J_3^\mu - \sin^2\theta_W J_{EM}^\mu &&= \overline{\psi}\gamma^\mu \frac{g_V - g_A\gamma^5}{2}\psi \\ J_{CC\pm}^\mu &= \overline{\psi}\gamma^\mu \frac{V - A\gamma^5}{2}\tau_\pm\psi \,. \end{aligned} \tag{1.22}$$

This defines the vector[1] and axial-vector[2] coupling constants of the weak neutral current:

$$g_V^f \equiv T_3^f - 2Q_f \sin^2\theta_W \quad (1.23)$$

$$g_A^f \equiv T_3^f \ , \quad (1.24)$$

which depend on the fermion species f.

The vector and axial-vector couplings V and A of the charged current are set in the Standard Model to

$$V \equiv 1 \qquad A \equiv 1 \ . \quad (1.25)$$

This represents the (V-A) form of the weak charged current.

The Standard Model makes no predictions for the value of the electroweak couplings g_1 and g_2. These, and some other parameters like fermion masses and quark mixing angles, have to be obtained from the experiment.

The Standard Model is very successful in the description of all experimental results. However, it is not believed to be the final theory. Firstly, it does not include gravity. It does not explain the number of families and the reason for the fractional electric charges. In addition there are conceptual problems of the Standard Model like e.g. the hierarchy problem [13, 14]. Furthermore, it is unsatisfactory that it contains a large number of free parameters.

Therefore various extensions of the Standard Model, for example supersymmetry, grand-unified or superstring theories, have been proposed [15, 16]. New physical phenomena are searched for by looking for deviations between Standard Model predictions from the experimental measurements.

1.3 The Tau as Standard Model Laboratory

With the c quark, predicted in 1970 [17] and discovered in 1974 [18,19], the fundamental fermions could be grouped into two families. Nevertheless theoretical calculations for the properties of a third charged lepton, heavier than the muon, were done [20, 21]. Searches for such a particle were performed at the ADONE e^+e^- storage ring (Frascati,

[1] The term $\overline{\psi}\gamma^\mu\psi$ transforms like a vector under Lorentz transformation.

[2] The term $\overline{\psi}\gamma^\mu\gamma^5\psi$ transforms like an axial-vector under Lorentz transformation.

Italy) from 1970 to 1974 [22], and with the MARK I experiment at the SPEAR e^+e^- collider (Stanford Linear Accelerator Centre), starting 1973. However, the discovery of the τ lepton by M. L. Perl [23] in 1975 came as a surprise, since the τ was the first particle of a third family of leptons and quarks. Since then, the τ lepton has been the subject of extensive study with growing interest, performed by several experiments at rising center-of-mass energies. Especially the very clean samples of boosted $\tau^+\tau^-$ events accumulated at LEP on the Z peak have improved the accuracy of the τ measurements and brought a new level of understanding. In the theoretical field, a lot of efforts have been invested to understand the τ dynamics. The detailed study of higher-order electroweak corrections and QCD contributions has promoted the physics of the τ lepton to the level of precision tests. These precision measurements include the study of the static properties of the τ (for a summary see [24, 25]), and the study of its interactions [26, 27].

All experimental results [28] obtained so far suggest that the τ lepton is a sequential lepton. Together with its associated neutrino, ν_τ, it is a member of the third family of fermions and identical to electron and muon except for the mass.

The world average of the τ mass, dominated by the BES Collaboration measurement at the BEPC collider [29], is [4]

$$m_\tau = 1777.05\ ^{+0.29}_{-0.26}\ \text{MeV} . \tag{1.26}$$

The lifetime of the τ lepton has been measured to be [4]:

$$\tau_\tau = 290.0\ \pm\ 1.2\ \text{fs} . \tag{1.27}$$

The τ lepton is the only known lepton massive enough to decay into hadrons. Its hadronic decays (table 1.4) allow to test the electroweak couplings of quarks, as well as to study strong interaction at a momentum scale defined by the τ mass.

The τ pair production in electron-positron collisions provides a unique laboratory to explore not only the τ lepton properties but also allows various tests of the electroweak and strong sector of the Standard Model, as indicated in figure 1.1. As the heaviest lepton the τ lepton could be particularly sensitive to new interactions related to the Higgs mechanism.

Decay Mode	Branching Fraction (%)
$\pi^-\nu_\tau$	11.08 ± 0.13
$\pi^-\pi^0\nu_\tau$	25.32 ± 0.15
$\pi^-2\pi^0\nu_\tau$	9.15 ± 0.15
$\pi^-\pi^+\pi^-\nu_\tau$	9.56 ± 0.11

Tab. 1.4: The present world average values of the branching fractions for the dominant hadronic decay modes of the τ [4].

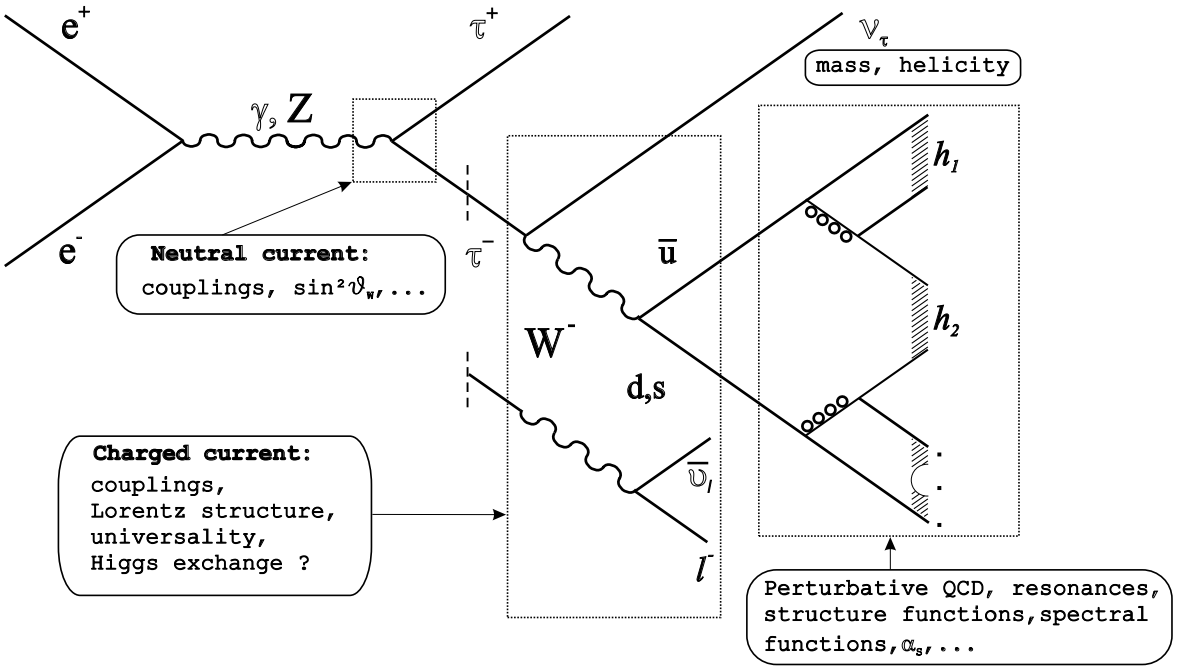

Fig. 1.1: The τ lepton as a laboratory to study the Standard Model.

1.4 Tau Pair Production

To lowest order in the Standard Model, only γ and Z boson exchange[3] contribute to the τ pair production from e^+e^- annihilation (figure 1.2).

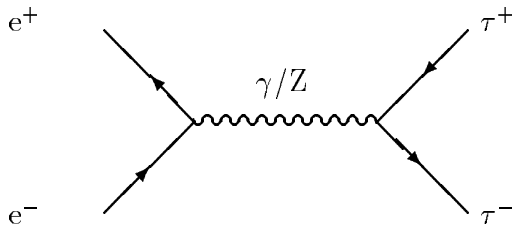

Fig. 1.2: Tree level Feynman diagram of the process $e^+e^- \to \tau^+\tau^-$.

For unpolarised beams [30], averaging over the helicity[4] states of the incoming electron and positron, the differential cross section for a certain final state helicity, h_τ, reads:

$$\begin{aligned}\frac{d\sigma_{\mathrm{Born}}(s,\cos\theta;h_\tau)}{d\cos\theta} &= \frac{3}{16}\left[\left(1+\cos^2\theta\right)F_0(s)+2\cos\theta F_1(s)+\right.\\ &\quad \left. h_\tau\left\{\left(1+\cos^2\theta\right)F_2(s)+2\cos\theta F_3(s)\right\}\right]\sigma_{QED}\ ,\end{aligned} \tag{1.28}$$

where $\sqrt{s}$ denotes the center-of-mass energy. Like the following considerations this equation is valid for any fermion[5] pair in the final state. The scattering angle θ is the polar angle of the τ^- with respect to the beam electron.

The pure photon exchange (QED) total cross section is given by:

$$\sigma_{QED}(s) = \frac{4\pi\alpha_{em}^2}{3s}, \tag{1.29}$$

where α_{em} is the electromagnetic fine structure constant. The functions $F_i(s)$ can be factorised by the electrical charge, Q_f, and the vector and axial-vector coupling

[3] The exchange of a Higgs boson is suppressed by $m_e^2 m_\tau^2/m_{\mathrm{Z}}^4 \approx 10^{-14}$ [24].

[4] The helicity $h = \frac{\vec{\sigma}\vec{p}}{|\vec{p}|}$ of a particle is the projection of its spin $\vec{\sigma}$ along its momentum $\vec{p}$.

[5] If the fermions are quarks, a colour factor, $N_f^c = 3$, appears.

constants, g_A^f and g_V^f:

$$\begin{aligned}
F_0(s) = &\quad Q_e^2 Q_\tau^2 + &2Q_e Q_\tau g_V^e g_V^\tau \mathrm{Re}(\chi(s)) + &\quad \left(g_V^{e\,2} + g_A^{e\,2}\right)\left(g_V^{\tau\,2} + g_A^{\tau\,2}\right)|\chi(s)|^2 \\
F_1(s) = &&2Q_e Q_\tau g_A^e g_A^\tau \mathrm{Re}(\chi(s)) + &\quad 2g_V^e g_A^e 2g_V^\tau g_A^\tau |\chi(s)|^2 \\
F_2(s) = &&2Q_e Q_\tau g_V^e g_A^\tau \mathrm{Re}(\chi(s)) + &\quad \left(g_V^{e\,2} + g_A^{e\,2}\right) 2g_V^\tau g_A^\tau |\chi(s)|^2 \\
F_3(s) = &&2Q_e Q_\tau g_A^e g_V^\tau \mathrm{Re}(\chi(s)) + &\quad 2g_V^e g_A^e \left(g_V^{\tau\,2} + g_A^{\tau\,2}\right)|\chi(s)|^2 \quad .
\end{aligned} \tag{1.30}$$

The term $Q_e^2 Q_\tau^2$ in F_0 arises from photon exchange, while the terms proportional to $|\chi(s)|^2$ and $\mathrm{Re}(\chi(s))$ describe the Z exchange and the interference between γ and Z, respectively. The complex function

$$\chi(s) = \frac{1}{4\sin^2\theta_W\ \cos^2\theta_W} \cdot \frac{s}{s - {m_\mathrm{Z}}^2 + i\, m_\mathrm{Z}\,\Gamma_\mathrm{Z}} \tag{1.31}$$

is the ratio of the Z and γ propagators with m_Z (Γ_Z) being the mass (width) of the Z. Summing over both helicity states and integrating over all scattering angles provides the total cross section:

$$\sigma(e^+e^- \to \tau^+\tau^-; s) \;\; = \;\; F_0(s)\,\sigma_{QED}(s)\;. \tag{1.32}$$

For centre-of-mass energies close to the Z mass, pure Z exchange dominates and the annihilation cross section is strongly enhanced. The measurement of $\sigma(s)$ allows precise determination of the Z parameters like mass, total width and partial decay width $\Gamma_{l\bar{l}}(l = e, \mu, \tau)$.

Asymmetries, which depend differently on the electroweak couplings of e and τ, are defined from the cross section as a function of the scattering angle and the helicity of the τ, h_τ:

$$\begin{aligned}
\mathrm{A_{FB}} &= \frac{\sigma(\cos\theta > 0) - \sigma(\cos\theta < 0)}{\sigma(\cos\theta > 0) + \sigma(\cos\theta < 0)} &= \frac{3}{4}\frac{F_1(s)}{F_0(s)} \\
\mathrm{A_{Pol}} &= \frac{\sigma(h_{\tau^-} = +1) - \sigma(h_{\tau^-} = -1)}{\sigma(h_{\tau^-} = +1) + \sigma(h_{\tau^-} = -1)} &= -\frac{F_3(s)}{F_0(s)} \\
\mathrm{A_{Pol}^{FB}} &= \frac{\sigma(h_{\tau^-}\cos\theta > 0) - \sigma(h_{\tau^-}\cos\theta < 0)}{\sigma(h_{\tau^-}\cos\theta > 0) + \sigma(h_{\tau^-}\cos\theta < 0)} &= -\frac{3}{4}\frac{F_4(s)}{F_0(s)} \quad .
\end{aligned} \tag{1.33}$$

Here $\mathrm{A_{FB}}$ is the forward-backward asymmetry, $\mathrm{A_{Pol}}$ the longitudinal polarisation, and $\mathrm{A_{Pol}^{FB}}$ the forward-backward polarisation.

On the Z peak their dependence on the neutral current couplings is given by:

$$\begin{aligned}
\sigma_{\mathrm{Born}}(s = {m_{\mathrm{Z}}}^2) &\simeq \left({g_V^e}^2 + {g_A^e}^2\right)\left({g_V^\tau}^2 + {g_A^\tau}^2\right) \\
\mathrm{A_{Pol}}(s = {m_{\mathrm{Z}}}^2) &\simeq -\frac{2 g_V^\tau g_A^\tau}{{g_V^\tau}^2 + {g_A^\tau}^2} \\
\mathrm{A_{FB}}(s = {m_{\mathrm{Z}}}^2) &\simeq \frac{3}{4}\frac{2 g_V^e g_A^e}{{g_V^e}^2 + {g_A^e}^2}\,\frac{2 g_V^\tau g_A^\tau}{{g_V^\tau}^2 + {g_A^\tau}^2} \\
\mathrm{A_{Pol}^{FB}}(s = {m_{\mathrm{Z}}}^2) &\simeq -\frac{3}{4}\frac{2 g_V^e g_A^e}{{g_V^e}^2 + {g_A^e}^2} \quad .
\end{aligned} \tag{1.34}$$

The Born approximation is not sufficient to match the high-precision measurement of the Z resonance at LEP and radiative corrections must be included. Some of them like photon radiation are applied as corrections to the measurement. Others are derived within the framework of the Standard Model and are subject of precision tests by comparing them to data. In addition, a part of them is very sensitive to new physical phenomena.

The neutral current couplings obtained from the current measurements agree well with the Standard Model prediction [31] and support e-μ-τ lepton universality with about 10% relative accuracy for vector couplings and about 0.1% for axial-vector couplings.

1.5 Tau Leptonic Decay

The dynamics of the τ decay into a lighter charged lepton[6] $l = e, \mu$ is fully determined in the Standard Model, where the decay is mediated by a W boson (figure 1.3).

The leptonic τ decays are treated as weak charged current interactions and are theoretically understood at the level of the electroweak radiative corrections [32]. The decay width is given by

$$\Gamma(\tau \to \nu_\tau l \bar{\nu}_l) = \Gamma^{Fermi}\, f\left(\frac{m_l^2}{m_\tau^2}\right)\, \delta_{\mathrm{W}}^\tau \delta_\gamma^\tau \,, \tag{1.35}$$

where the decay rate

$$\Gamma^{Fermi} = \frac{G_{\tau l}^2 m_\tau^5}{192\pi^3} \tag{1.36}$$

[6] Even if not stated explicitely, the τ always decays into a lepton (hadron) *and* neutrino(s).

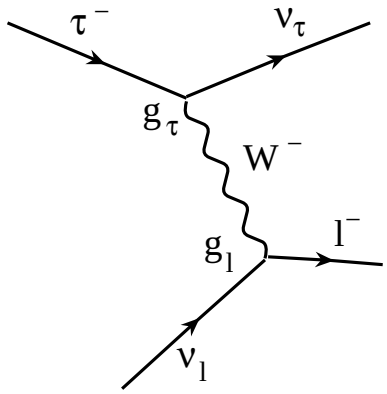

Fig. 1.3: The lowest order Feynman diagram describing the decay of the τ into lighter charged leptons. The charged current couplings are indicated at both vertices.

is known from the four-fermion theory [33]. This theory assumes a direct four-fermion interaction with the effective coupling G_F and is a good approximation within the limit where the squared momentum q^2 of the exchanged W is small compared to m_{W}^2.

The coupling $G_{\tau l}$ can be expressed in terms of $SU(2)_L$ couplings:

$$G_{\tau l}^2 \;=\; \frac{g_\tau^2 g_l^2}{32\, m_{\mathrm{W}}^4} \qquad\qquad l = e, \mu \; . \tag{1.37}$$

The quantities $f\left(\frac{m_l^2}{m_\tau^2}\right)$, δ_{W}^τ, δ_γ^τ are a phase space factor, a propagator mass correction and QED radiative corrections. They are calculated as follows:

Phase Space Correction: The mass of the final state leptons reduces the available phase space and thus the decay rate because a minimum energy is required to create the lepton. This correction is given in terms of $x = \frac{m_l^2}{m_\tau^2}$ by [34,35]

$$f(x) \;=\; 1 - 8x + 8x^3 - x^4 - 12x^2 \ln x, \tag{1.38}$$

leading to $f(\frac{m_e^2}{m_\tau^2}) = 1.0000$ and $f(\frac{m_\mu^2}{m_\tau^2}) = 0.9726$.

Propagator Mass Correction: Effects from the W propagator including $\mathcal{O}(\frac{m_l^2}{m_{\mathrm{W}}^2})$ tree level contributions are considered by the factor [32,36][7]

$$\delta_{\mathrm{W}}^\tau \;=\; 1 + \frac{3}{5}\frac{m_\tau^2}{m_{\mathrm{W}}^2} + \frac{9}{5}\frac{m_l^2}{m_{\mathrm{W}}^2} \; . \tag{1.39}$$

[7] Note, that the second term is given as $-2\frac{m_l^2}{m_{\mathrm{W}}^2}$ in literature (e.g. [27, 37]). The correct one used here is calculated by T.Riemann and was confirmed by W.J.Marciano.

With $m_{\mathrm{W}} = 80.396 \pm 0.061$ [4] the correction is 1.00029.

QED Radiative Corrections: Most of the electroweak radiative corrections are absorbed in $G_{\tau l}$ [38]. The QED radiative corrections were considered separately for historical reasons. They have been calculated [34, 39] to be:

$$\delta_\gamma^\tau = 1 + \frac{\alpha(m_\tau)}{2\pi}\left(\frac{25}{4} - \pi^2\right). \tag{1.40}$$

Here $\alpha(m_\tau)$ is the running electromagnetic coupling constant evaluated at m_τ. The running of the coupling constant is caused by the screening of the bare electric charge, due to the polarisability of the vacuum. Explicit calculations of the vacuum polarisation diagrams lead to the differential equation of the running of α as a function of the energy scale, μ (see for example [40]), from which $\alpha(m_\tau)$ was calculated to [32]:

$$\alpha(m_\tau) = 1/133.3\ . \tag{1.41}$$

This gives a QED radiative correction of

$$\delta_\gamma^\tau = 0.99568\ . \tag{1.42}$$

If lepton universality holds, then the coupling $G_{\tau l}$ is equal to the Fermi constant G_F. G_F is obtained from the muon lifetime [4]

$$\tau_\mu = (2.197035 \pm 0.000004) \times 10^{-6} s \tag{1.43}$$

using

$$\tau_\mu = \frac{1}{\Gamma(\mu \to \nu_\mu e \bar{\nu}_e)}\ , \tag{1.44}$$

where $\Gamma(\mu \to \nu_\mu e \bar{\nu}_e)$ can be calculated from equation 1.35 by replacing m_τ with m_μ, and m_l with m_e. Furthermore the QED radiative corrections for $\mu \to \nu_\mu e \bar{\nu}_e$ have been calculated through $\mathcal{O}(\alpha^2)$ [41], allowing a very precise determination of the Fermi constant to [38]:

$$G_F = (1.16637 \pm 0.00001) \times 10^{-5}\,\mathrm{GeV}^{-2}\ . \tag{1.45}$$

1.6 Physics Interest in Tau Leptonic Branching Fractions

The leptonic decay widths of the τ are predicted by equation 1.35 with high precision. The best experimental determination of the leptonic widths is obtained from the measurement of the τ lifetime, τ_τ, and the *leptonic branching fractions*, B_l, from

$$\Gamma(\tau \to \nu_\tau l \bar{\nu}_l) \;=\; \frac{B_l}{\tau_\tau} \tag{1.46}$$

with

$$B_l \;=\; \frac{\Gamma(\tau \to \nu_\tau l \bar{\nu}_l)}{\Gamma_{tot}}. \tag{1.47}$$

Here, Γ_{tot} is the total decay width of the τ.

Equation 1.46 is a relation between lifetime and leptonic branching fractions, which has to be confirmed experimentally.

Lepton Universality

In the Standard Model the couplings of the weak charged current do not depend on the lepton flavour:

$$g_\tau = g_\mu = g_e \;. \tag{1.48}$$

This reflects lepton universality.

Comparing the rates of the two leptonic τ decays allows to test the universality for electron and muon directly:

$$\frac{\Gamma(\tau \to \nu_\tau \mu \bar{\nu}_\mu)}{\Gamma(\tau \to \nu_\tau e \bar{\nu}_e)} = \frac{B_\mu}{B_e} = c_f \frac{g_\mu^2}{g_e^2} \;. \tag{1.49}$$

The factor

$$c_f = \frac{f\left(\frac{m_\mu^2}{m_\tau^2}\right)}{f\left(\frac{m_e^2}{m_\tau^2}\right)} = 0.9726 \tag{1.50}$$

is solely given by the phase space corrections due to different masses of e and μ for both decay modes.

A comparison of the charged current couplings of the τ to the couplings of the other leptons is obtained by dividing the total decay width for the muon decay, $\Gamma(\mu \to \nu_\mu e \bar{\nu}_e)$, by the width for the leptonic τ decay, $\Gamma(\tau \to \nu_\tau l \bar{\nu}_l)$:

$$\left(\frac{g_\tau}{g_l}\right)^2 = \left(\frac{m_\mu}{m_\tau}\right)^5 \frac{\tau_\mu}{\tau_\tau} B_{l'} \left[\frac{f\left(\frac{m_e^2}{m_\mu^2}\right)}{f\left(\frac{m_l^2}{m_\tau^2}\right)} \frac{\delta_{\mathrm{W}}^\mu \delta_\gamma^\mu}{\delta_{\mathrm{W}}^\tau \delta_\gamma^\tau}\right] , \tag{1.51}$$

with

$$l = e, \mu \qquad l' = \mu, e \qquad l' \neq l \; . \tag{1.52}$$

The factor in the square brackets accounts for the phase space corrections and the electroweak corrections. It is 1.0004 for $l = e$ and 0.9729 for $l = \mu$.

Moreover, lepton universality requires that the couplings $G_{\tau e}$ and $G_{\tau \mu}$, defined in equation 1.37, are equal to the Fermi constant G_F obtained from muon decay. The couplings $G_{\tau l}$ can be calculated from equation 1.35, using the measured τ lifetime and leptonic branching fractions (equation 1.46).

Determination of α_s

Compared to the leptonic decay modes the calculation of the hadronic decay rates is by far more complicated because the observed hadrons do not couple to the W directly. The decay rate into hadrons depends on the strong coupling constant, α_s. At the low momentum scale of the τ decay α_s is relatively large, so perturbative calculations must be done to more than one order in α_s. In addition, non-perturbative effects are expected.

The total hadronic width has been calculated using analyticity and the operator product expansion [42–45]. The hadronic τ decay width is one of the very few quantities calculated to $\mathcal{O}(\alpha_s^3)$, and the non-perturbative corrections have been shown to be largely suppressed.

In practice, the ratio of the hadronic to leptonic τ decay width, R_τ, is used:

$$R_\tau \equiv \frac{\Gamma(\tau \to \nu + \text{hadrons})}{\Gamma(\tau \to e \nu \bar{\nu})} \; . \tag{1.53}$$

It is given in the lowest order by the number of quark colours $N_C = 3$.

Following [45], R_τ, including QCD and electroweak corrections corrections, can be written as

$$R_\tau = 3(|V_{ud}|^2 + |V_{us}|^2) S_{EW} \left\{1 + \delta_{EW} + \delta^{(0)} + \sum_{D=2,4\ldots} \delta^{(D)}\right\} , \tag{1.54}$$

where $|V_{ud}| = 0.9735 \pm 0.0008$ and $|V_{us}| = 0.2196 \pm 0.0023$ are CKM mixing angles [4] and the factors $S_{EW} = 1.0194 \pm 0.0040$ [32] and $\delta_{EW} \simeq 0.0010$ [46] contain electroweak corrections.

Perturbative QCD corrections have been calculated to be [42,43,45]:

$$\delta^{(0)} = \left(\frac{\alpha_s(m_\tau^2)}{\pi}\right) + 5.2023 \left(\frac{\alpha_s(m_\tau^2)}{\pi}\right)^2 + 26.366 \left(\frac{\alpha_s(m_\tau^2)}{\pi}\right)^3 + \mathcal{O}\left(\alpha_s^4\right) \ . \quad (1.55)$$

The $\mathcal{O}(\alpha_s^4)$ contribution is [44]

$$\delta_4^{(0)} = (78 + K_4) \left(\frac{\alpha_s(m_\tau^2)}{\pi}\right)^4 \ , \quad (1.56)$$

with $K_4 = 27.5 \pm 50$ [27, 47]. The non-perturbative contributions are estimated to be [48]

$$\sum_{D=2,4\ldots} \delta^{(D)} = -0.014 \pm 0.005 \quad (1.57)$$

and hence small in comparison to the perturbative terms. Recent measurements of the moment of the τ hadronic spectral functions have confirmed this value [49,50].

Therefore the perturbative QCD contributions are dominant and provide sensitivity of R_τ to α_s.

Experimentally R_τ can be measured from the τ leptonic branching fractions:

$$R_\tau = \frac{1 - B_e - B_\mu}{B_e} \ , \quad (1.58)$$

drawing on the fact that the total decay width of the τ is the sum of the inclusive hadronic width and the leptonic widths. Using the measured R_τ, the strong coupling constant can be extracted from equations 1.54 and 1.55.

The Mass of the Tau Neutrino

The recent indications for neutrino mixing, and therefore for a mass, at the Super-Kamiokande atmospheric neutrino experiment [51] give further motivation to look for the effect of a non-zero mass m_{ν_τ} of the τ neutrino, ν_τ, in τ decays.

The first limits on m_{ν_τ} have been estimated by studying the endpoint of the momentum spectrum of the charged leptons from leptonic τ decays. The precision which can be obtained is limited by the experimental momentum resolution, which deteriorates with

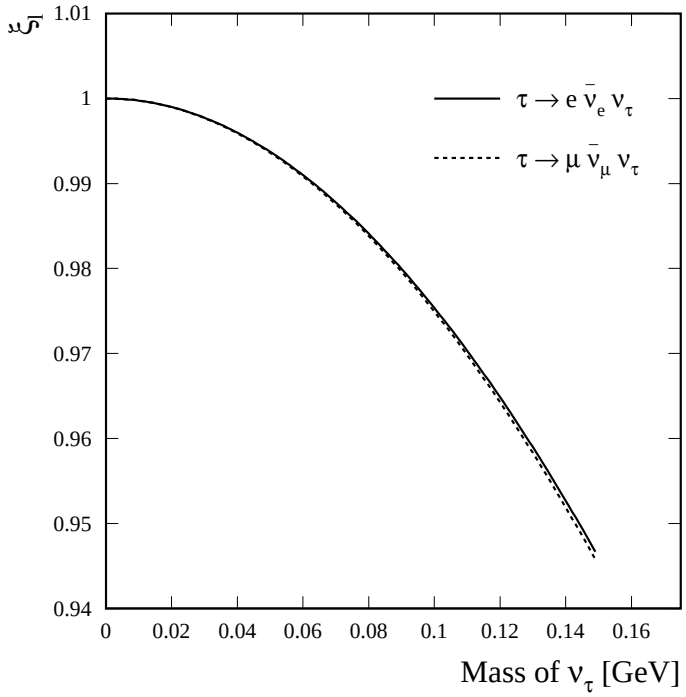

Fig. 1.4: The m_{ν_τ} dependent correction to the leptonic decay width, $\xi_l(m_{\nu_\tau})$, plotted as a function of the τ neutrino mass m_{ν_τ}. The solid and dashed lines represent the τ decaying into an electron and a muon, respectively.

increasing centre-of-mass energies. Better limits have been obtained by studying the endpoint of the effective hadronic mass and energy of high multiplicity τ decays.

Alternatively one can exploit the leptonic decay width to extract a limit on m_{ν_τ}. So far the neutrino mass was set to zero for all calculations, but without changing the structure of the theory, $\Gamma(\tau \rightarrow \nu_\tau l \bar{\nu})$ can be calculated for non-zero values of m_{ν_τ}. These calculations have been done for ν_τ in the range from 0 to 130 MeV [52]. The decay width can then be decomposed in the width at zero neutrino mass, $\Gamma(m_{\nu_\tau} = 0)$, and a correction function $\xi_l(m_{\nu_\tau})$, which is sensitive to m_{ν_τ}. Figure 1.4 shows $\xi_l(m_{\nu_\tau})$ in dependence on the presumed τ neutrino mass.

A limit on m_{ν_τ} can be obtained from the leptonic branching fraction together with the τ lifetime as follows:

$$m_{\nu_\tau} = \xi_l^{-1} \left\{ \frac{B_l}{\tau_\tau \, \Gamma(m_{\nu_\tau} = 0)} \right\} , \tag{1.59}$$

Here $\xi_l^{-1}\{\}$ represents the inverse function of $\xi_l(m_{\nu_\tau})$.

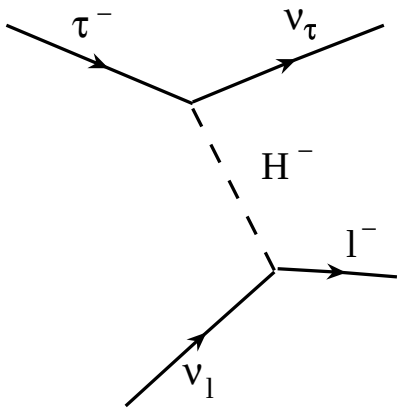

Fig. 1.5: The lowest order Feynman diagram describing the decay of the τ into leptons mediated by the exchange of a charged Higgs boson.

Higgs Exchange

Many extensions of the Standard Model involve an extended Higgs sector with more than one Higgs doublet. Such models contain charged Higgs bosons which contribute to the weak charged current with couplings rising with the fermion masses (figure 1.5). Therefore Higgs exchange amplitudes are in particular enhanced in $\tau \to \mu\bar{\nu}\nu$ and thus modify the ratio of the leptonic branching fractions.

The ratio g_μ/g_e depends on the mass of the charged Higgs $m_{H^\pm}$ and the ratio of the vacuum expectation values associated to the two Higgs doublets, $\tan\beta$, [53]:

$$\frac{g_\mu^2}{g_e^2} = \frac{1 - 4K\dfrac{m_\mu}{m_\tau}\dfrac{c_H(\mu)}{1+c_H(\mu)^2}}{1 - 4K\dfrac{m_e}{m_\tau}\dfrac{c_H(e)}{1+c_H(e)^2}} = \frac{B_\mu}{B_e}\frac{1}{c_f} \tag{1.60}$$

with [54, 55]:

$$c_H(l) = \frac{m_l m_\tau \tan^2\beta}{2m_H^2}\,. \tag{1.61}$$

The factor K corrects the restricted range of momenta used in the measurement of the branching fractions. It is estimated to $K = 0.96$ [56]. The phase space correction is defined in equation 1.50.

In conclusion, the measurement of the leptonic branching fractions of the τ lepton allows to test a fundamental assumption of the Standard Model, the lepton universality. Furthermore, the measurement can be used to determine α_s and to set limits on the mass of the τ neutrino and on the mass of a charged Higgs boson. This challenges to measure the τ leptonic branching fractions with utmost precision.

Chapter 2

THE L3 EXPERIMENT AT LEP

An important part of today's particle physics is done in collider experiments on large storage rings. These colliders provide a huge number of events, produced in head-to-head collisions of stored beams under well defined and stable conditions. In case of annihilation, the centre-of-mass energy of the event is twice the beam energy[1]. One of the first successfully working electron-positron storage ring colliders [57] was the VEPP II, where the ρ-resonance was studied in 1967 by colliding 380 MeV electrons with 380 MeV positrons and measuring the pair of π-mesons from the decay of the ρ. The size of these colliders measured only about few metres including the detector components. The further development, aimed to improve luminosity and energy, led to storage rings with diameters of several hundred metres. The maximum energy for a certain radius of a storage ring is limited by synchrotron radiation[2], leading to an over-proportional increase of radius and costs with peak energy. As suggested already in 1965, electron linear colliders are more cost effective at very high energies [58]. This energy seems to be reached by LEP.

2.1 The Large Electron Positron Collider

LEP [59] started operation at the European Laboratory for Particle Physics CERN in 1989. It is located on the border between France and Switzerland close to Geneva. The LEP ring is situated in an underground tunnel with a circumference of 26.7 km. Electrons and positrons are accelerated and stored in the same vacuum pipe.

Up to 1995 LEP worked at centre-of-mass energies of the electron positron system

[1] This is different in fixed target experiments, where the centre-of-mass energy E_{cms} depends on the beam energy E_{beam} and the mass M of the particle at rest: $E_{\mathrm{cms}} = \sqrt{2m \cdot (E_{\mathrm{beam}} + M)}$.

[2] The energy loss per turn for a particle circulating in a ring of a radius ρ is $E_{sync} = \frac{4\pi}{3}\frac{e^2}{\rho}(\frac{E_{\mathrm{beam}}}{mc})^4$.

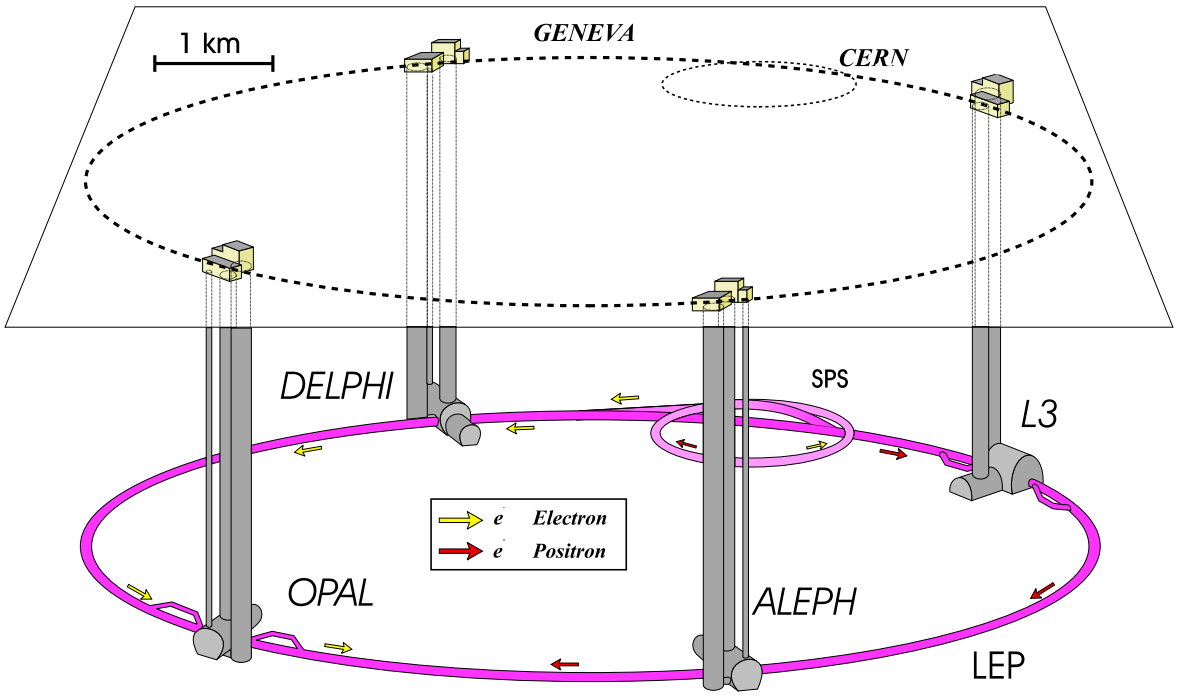

Fig. 2.1: The LEP site with the experiments ALEPH, DELPHI, L3 and OPAL.

around the Z resonance where the cross section for the production of Z bosons is dominant (LEP I). The study of e^+e^- annihilation provides a large variety of possibilities for testing the Standard Model. The huge number of recorded events[3] allows to determine with high precision Standard Model parameters like the Z boson properties and its couplings. Since end of 1995 the centre-of-mass energy was increased in several steps up to 200 GeV(LEP II). This moved the focus of the investigations more to fields like $W^{\pm}$ pair production and the search for new particles.

Electrons and positrons are created and pre-accelerated in the LEP injection chain [60] consisting of two linear accelerators, an Electron-Positron Accumulator (EPA) and two synchrotrons. The electrons leave the first linear accelerator with an energy of 200 MeV. At this point the positrons are produced from a part of the electron beam by scattering on a fixed tungsten target. Both electrons and positrons are accelerated up to 600 MeV in the second linac, passing the EPA and reaching the CERN Proton Synchrotron (PS). The PS operates as a 3.5 GeV electron-positron synchrotron and injects into the CERN Super Proton Synchrotron (SPS), which is used as a 20 GeV electron-positron injector for LEP. The particles are accelerated up to the

[3] About 20 million events were detected by the the four experiments between 1989 and 1995.

collision energies in the LEP ring and stored there. The ring itself consists of eight segments of a full circle connected by straight sections. The bending sections have a length of 2840 m each. All eight straight sections contain an interaction point, four of them were equipped with large detectors, ALEPH [61], DELPHI [62], L3 [63] and OPAL [64] (figure 2.1). Two of the remaining straight sections contain the radio-frequency cavities which accelerate the beam to the nominal energy and compensate for the energy losses due to synchrotron radiation in the curved sections.

The electron-positron interactions are produced by 4×4 (or 8×8) bunches of 10^{11} particles each. In 1995 a typical LEP fill lasted for about 12 hours of data taking giving an average integrated luminosity of 300–500 nb^{-1}.

2.2 The L3 Detector

The L3 experiment [65] is constructed to study e^+e^- interactions up to 200 GeV. It is optimised for precise energy measurements of electrons, photons and muons [63]. The detector consists of several subdetectors, installed within a 7800 ton magnet providing a 0.5 T solenoidal field along the beam axis. In the central 'barrel' region the subdetectors are arranged in a cylindrical form around the beam axis, in the forward and backward directions 'endcaps' are placed to cover almost the full solid angle.

From the interaction point outwards the barrel consists of (figure 2.2):

- a central tracking system (CTS),
- an electromagnetic calorimeter (ECAL),
- scintillation counters,
- a hadron calorimeter (HCAL),
- a muon filter,
- a muon detector (MCH),
- a luminosity monitor.

These subdetectors are complemented by triggering and data taking electronics and a cluster of online and offline computers. All detectors except the muon spectrometer are installed in a 32 m long, 4.45 m diameter steel support tube which is aligned concentrically with the beam pipe.

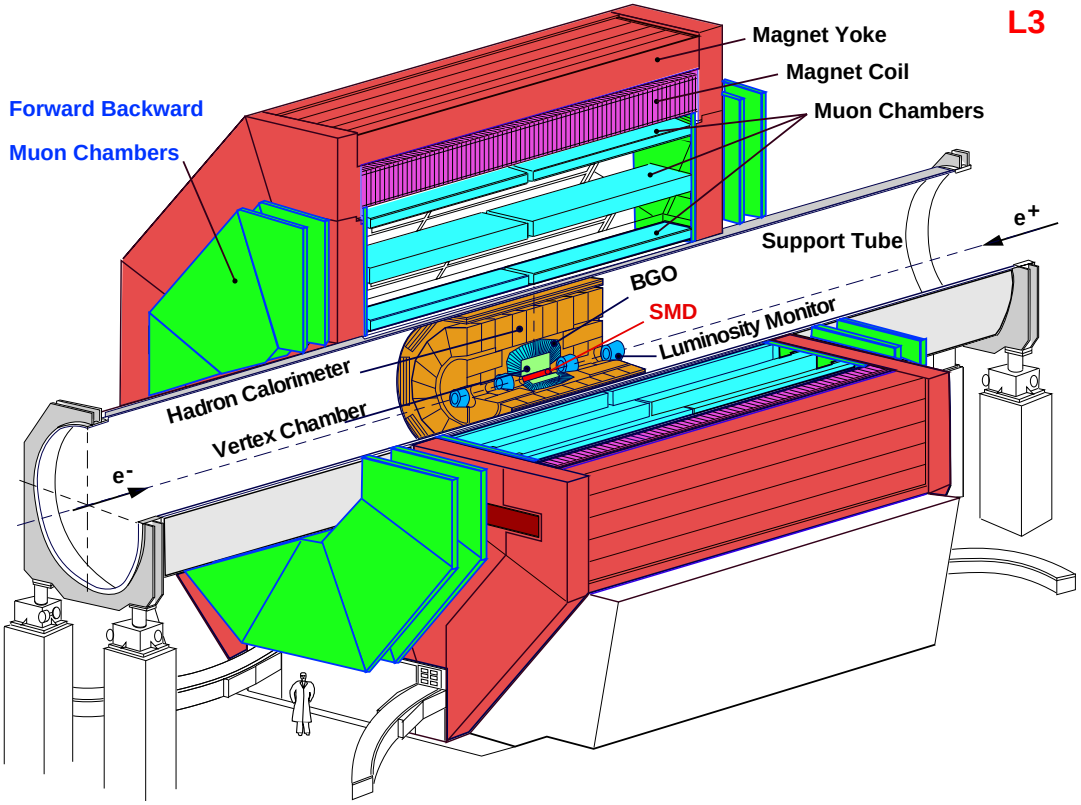

Fig. 2.2: A perspective view of the L3 detector.

Positions and directions in L3 are specified in a right-handed coordinate system with its origin placed at the nominal interaction point in the geometrical centre of the detector. The positive z-axis is given by the direction of the electron beam, and the positive x-axis points to the centre of the LEP ring.

The polar coordinates were chosen in the usual way: r and ϕ give the distance and angle in the $x-y$ plane, and θ is the polar angle with respect to the z-axis. Due to the solenoidal magnetic field a charged particle moves on a helicoidal track in the L3 detector. The projection of the helix is a circle in the r-ϕ plane. Quantities in this plane are referred as "transverse".

2.2.1 The Central Tracking System

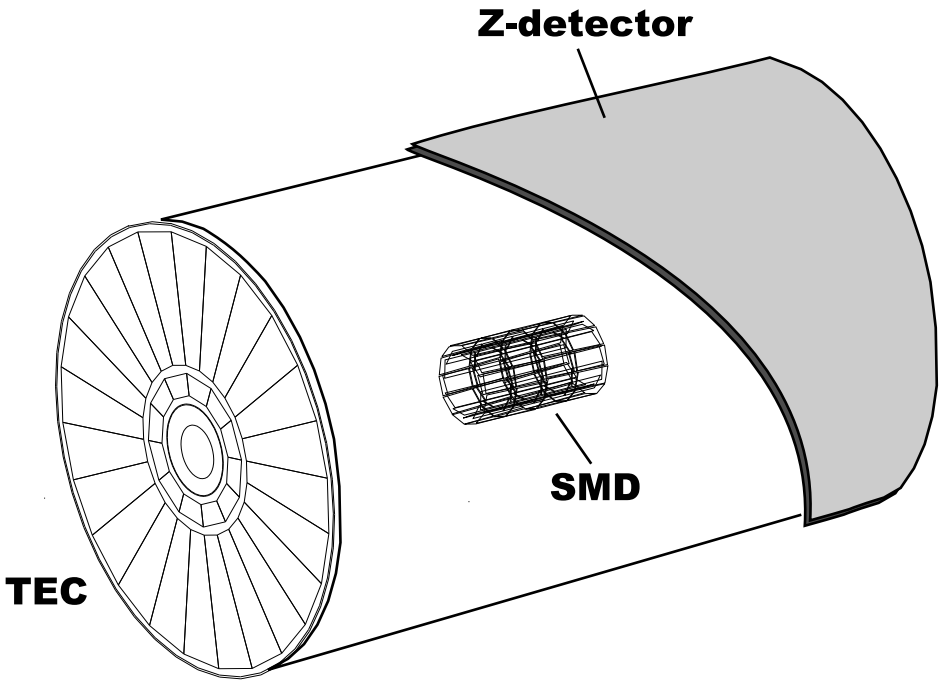

Fig. 2.3: The central tracking system, consisting of SMD, TEC and Z-detector.

The L3 central tracking system (Figure 2.3) contains the

- Silicon Microvertex Detector (SMD),
- Time Expansion Chamber (TEC),
- Z-Detector (ZCH).

Since the magnetic field is low and the maximum available radius inside of the ECAL is 52 cm a high spatial resolution is necessary to measure tracks from charged particles emerging from the interaction region with sufficient momentum resolution. The central tracking system fulfils this requirement and provides precise information on:

- the transverse momentum (P_T),
- the polar angle of tracks,
- the impact point of charged particles in the ECAL,
- the interaction point and secondary vertices.

The Silicon Microvertex Detector

The SMD [66] was constructed and installed as part of an L3 upgrade in 1993 to improve the impact parameter resolution, the polar angle measurement and the momentum resolution. It is mounted outwards on the 11 cm diameter beam tube. The axial length of 30 cm yields a polar angle coverage of $22° \leq \theta \leq 158°$.

Its components are two cylindrical layers of double-sided silicon strip detectors providing both polar and azimuthal coordinate measurements. The r-ϕ measurement is performed by the inner side of each silicon sensor, the z measurement by the outer side. Each layer consists of 12 modules, each one subdivided into 4 silicon wafers. Adjacent inner layers have an overlap in ϕ of 10%. The readout strips of the outer modules are tilted by 2° against the inner ones. Figure 2.4 illustrates the geometry of the SMD. The SMD provides additional high precision track points close to the primary vertex. Spatial resolutions of 7 μm and 14 μm for the r-ϕ and z coordinates, respectively, are obtained [67].

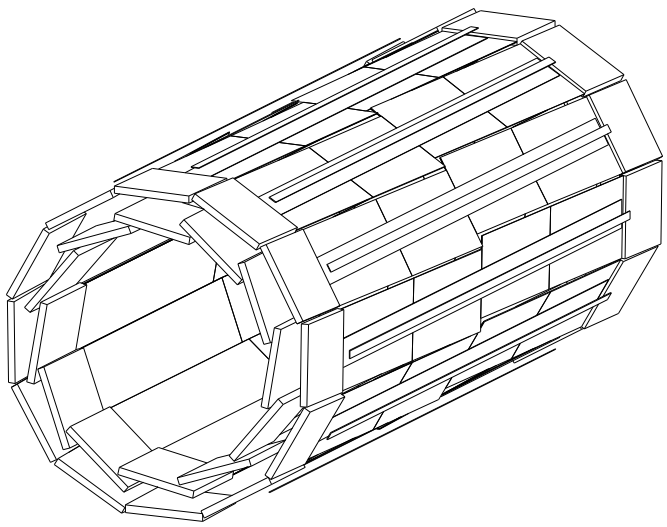

Fig. 2.4: A perspective view of the SMD.

The Time Expansion Chamber

The TEC [68] is a cylindrical chamber split by grids into large drift regions with a low homogeneous electric field and small amplification regions with a high electric field.

The low drift field operation called *time expansion mode* provides low drift velocities resulting in a high spatial resolution and good multi-track separation.

The electrons generated by an ionising particle drift with a constant velocity of approximately 6 μm/ns towards the amplification region, where gas amplification leads to avalanches at the anode wires. The anode pulses are digitised by 100 MHz analog-to-digital converters in order to obtain a precise drift-time measurement by a centre-of-gravity method.

The inner part of the TEC, divided into 12 sectors covering the full azimuthal angle, contains 8 anode wires strung parallel to the z-axis. The outer TEC is subdivided into 24 sectors with 54 anodes each. Since the TEC sectors are symmetric with respect to the anode plane, the measurement of the drift time only does not allow to decide on which side of the anode plane the particle passed. This ambiguity is resolved by read out the signal of pick-up wires on both sides of the anode plane and by matching the tracks measured in inner and outer TEC sectors (figure 2.5).

The single wire spatial resolution is approximately 50 μm. Using the total radial lever arm of 32 cm a transverse momentum resolution of $\sigma_{P_T}/P_T = 0.0018 P_T$ (GeV/c) can be achieved.

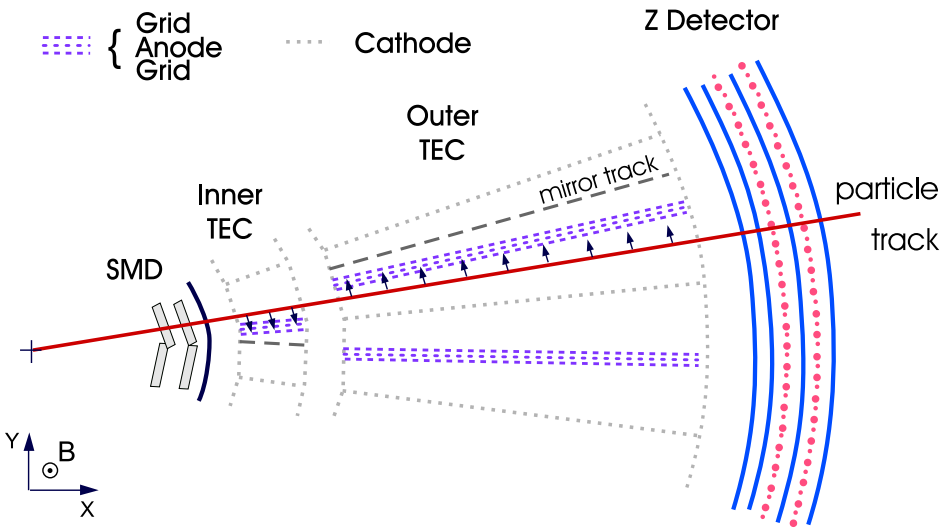

Fig. 2.5: Cross section of the L3 tracking system showing the structure of the inner and outer sectors of the TEC.

The Z-Detector

The TEC is surrounded by the Z-detector [69] to supplement the measurements from TEC and SMD with a z coordinate measurement in the angular range of $42° \leq \theta \leq 138°$.

It consists of two cylindrical proportional multiwire chambers with cathode strip readout. The 576 anode wires per chamber are strung in the axial direction. Each wire chamber contains two cathode layers. The 240 readout strips of one cathode layer in each chamber are oriented perpendicular to the chamber axis whereas the strips of the remaining layers form a helix with an angle of $\pm$ 69° to the axis (stereo layer).

A particle traversing the Z-detector generates an avalanche of electrons close to the wire. The avalanche induces image charges on both cathode layers. The measurement of the charge distribution allows to localise the avalanche position along the wire. The ϕ component of the stereo layer measurement is used to match the information about z with the tracks measured in the TEC.

The intrinsic efficiency of each chamber is approximately 96%. The resolution varies between 200 μm and 800 μm going from the centre to the edges of the Z-detector.

2.2.2 The Electromagnetic Calorimeter

The electromagnetic calorimeter [70], shown in figure 2.6, measures electrons and photons with high energy and spatial resolutions. It surrounds the central tracking system and is assembled from 10734 bismuth germanate ($Bi_4 Ge_3 O_{12}$) crystals used as showering and detecting medium. The central 'barrel' part of the detector contains 7680 crystals and covers a polar angle range of $42° \leq \theta \leq 138°$. The polar angle coverage of the two endcaps each consisting of 1527 crystals is $11.6° \leq \theta \leq 38°$ in the forward and $142° \leq \theta \leq 168.4°$ in the backward direction. The inner radius at $\theta = 90°$ is 520 mm. Each crystal in the barrel has the form of a truncated pyramid with a front face of 2×2 cm^2 and a rear face of 3×3 cm^2. All crystals point towards the interaction region, with a small offset of 10 mrad in ϕ to suppress energy leakage through the carbon fibre walls. Two photodiodes glued on their rear face and associated linear electronics detect the scintillation light. The crystal length of about 24 cm corresponds to approximately 22 radiation lengths or 1.1 nuclear interaction lengths. The tolerances of crystal dimensions are on the order of 100 μm to minimise the space between crystals where particles are undetected.

Bismuth germanate (BGO) is an inorganic scintillator providing an excellent energy resolution for electromagnetic showers over a wide range. The energy resolution is

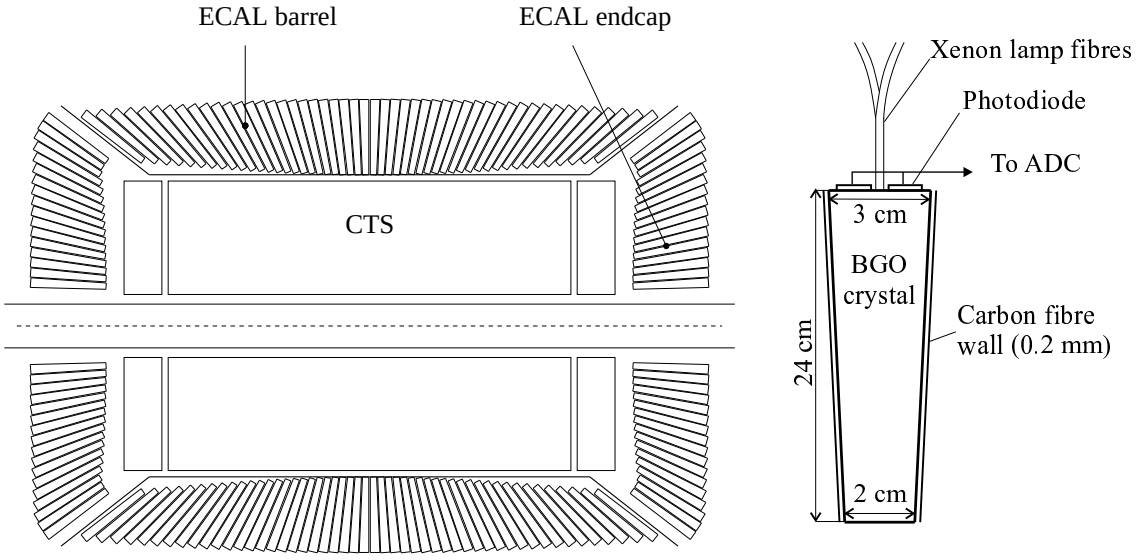

Fig. 2.6: The electromagnetic calorimeter (ECAL) in a side view. The right picture illustrates the geometry of one crystal.

measured to be 5% at 100 MeV and less than 2% for energies larger than 1 GeV [71].

The light produced in a BGO crystal by a particle of a given energy depends strongly on the crystal temperature, it decreases with rising temperatures[4]. Therefore the lowest possible temperature above the dew point, which is at about 18 °C, is used during data taking. The temperature of the crystals is kept within $\pm 0.5\,^{o}$C.

Calibration constants for each crystal in the barrel are determined from a test beam study in 1988 with 2, 10 and 50 GeV electron beams produced by the CERN SPS. A continuous calibration and monitoring of the calorimeter is ensured by three independent methods. A xenon light monitor measures the transparency of the crystals by the comparison of the response from the photodiodes with a generated reference light pulse. Bhabha scattering is used to calibrate the BGO at beam energy. An absolute energy scale calibration at low energies is achieved with cosmic muons. In addition, a Radio Frequency Quadrupole (RFQ) system is used for calibration. Dead and noisy crystals are detected online and put into a database.

Due to the fine segmentation of the crystal array of the calorimeter relative to the BGO Molière radius of 2.4 cm [72] the transverse shape of electromagnetic showers and the impact point of electrons and photons can be reconstructed. This provides a

[4] Temperature coefficient of light yield: -1.55 %/°C at 25°C

discrimination between electromagnetic and nonelectromagnetic origins. The measured angular resolution for the impact point ranges from about 5 mrad at 1 GeV to 1 mrad at 45 GeV [71].

2.2.3 The Scintillation Counters

The scintillation counter system is installed between the electromagnetic and hadronic calorimeters. It consists of 30 barrel counters and 32 counters located in front of each hadron endcap. The scintillators provide precise time information for particles passing through. These signals are used to trigger hadronic events based on the hit multiplicity. The time resolution of better than 0.5 ns provides a rejection of cosmic rays. The time-of-flight difference between opposite counters is about 6 ns for a cosmic muon which passes near the interaction point, whereas for a muon pair produced in a Z decay the difference is zero. The scintillator time related to the nominal time of the interaction and corrected for the time of flight peaks around zero for events coming from e^+e^- collisions. This allows further discrimination of cosmic muons.

2.2.4 The Hadron Calorimeter

In order to determine the total energy of hadrons the electromagnetic calorimeter is complemented by a hadron calorimeter, HCAL. The HCAL is made of depleted uranium absorber plates interspersed with gas proportional wire chambers. It is divided into a barrel part and two endcaps. The barrel has a modular structure consisting of 9 rings of 16 modules each as shown in figure 2.7 and covers the angular range $|\cos\theta| < 0.8$ over the full azimuthal range. The wire chambers are grouped to form readout towers pointing to the interaction region. They measure the showers induced by particles passing the uranium.

The integral depth of the calorimeter in nuclear interaction length for particles varies between 6 and 7, depending on the polar angle.

The fine segmentation of the calorimeters allows a measurement of the axis for single hadron jets[5] with a precision of approximately 35 mrad. High longitudinal segmentation of the HCAL is also used to identify penetrating muons by their minimum ionising signature along the track. In test beam studies the energy resolution for single pions was determined to be $(55/\sqrt{E/\mathrm{GeV}} + 5)\%$ [63]. The total energy resolution measured

[5] Particles in a spatial cone can form a jet.

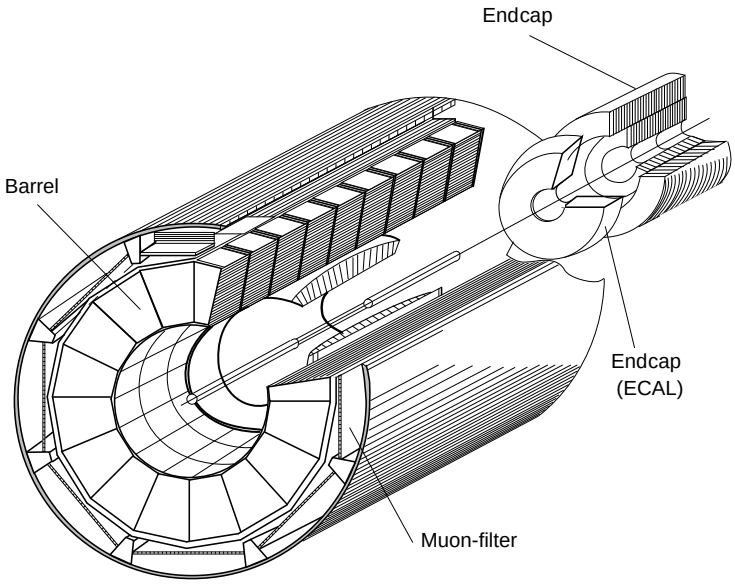

Fig. 2.7: The hadron calorimeter.

in hadronic Z decays is better than 10% in the barrel part [73].

To extend the total absorption length a muon filter is mounted just inside the support tube. It absorbs showers leaking outside the HCAL and ensures that only minimum ionising particles reach the muon spectrometer.

2.2.5 The Muon Spectrometer

The L3 muon spectrometer [74,75] is mounted outside the support tube but inside the magnet. It covers a polar angle from 35° to 145°.

The spectrometer is a system of multiwire drift chambers divided into two halves symmetrically arranged perpendicular to the beam pipe on both sides of the interaction point. The chambers are grouped in three equidistant layers of independent octants in each halve. Each octant contains five P-chambers: two outer and two middle chambers and one inner chamber (see Figure 2.8).

Each outer chamber is divided into 21 identical drift cells with 16 anode wires, each middle chamber has 15 cells with 24 wires, and each inner chamber contains 19 cells with 16 wires. The chamber cell has been designed to have a uniform electric field throughout the drift region.

The inner and the outer chambers are covered on the top and bottom by Z-chambers. P-chambers measure the track coordinates in the bending r-ϕ plane, whereas

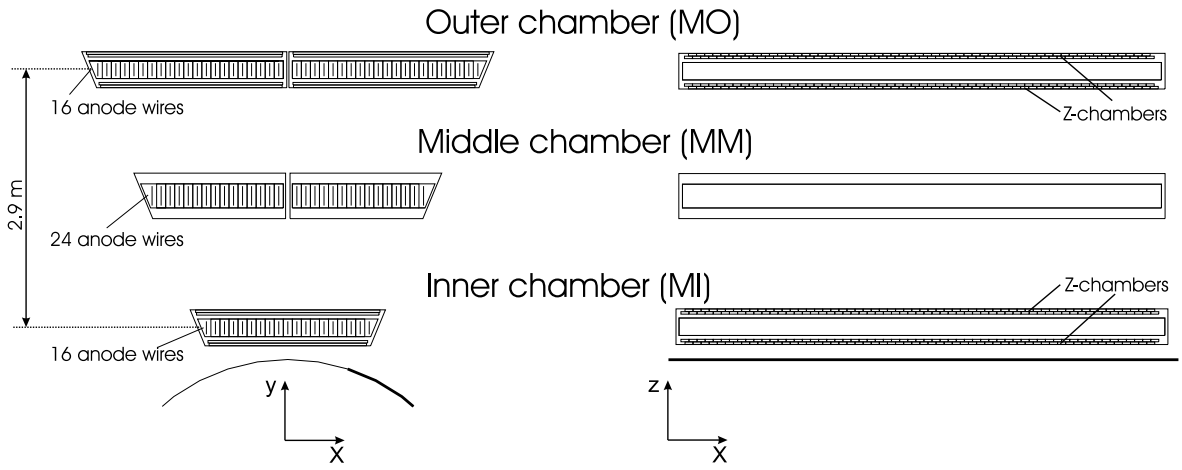

Fig. 2.8: Structure of a muon spectrometer octant. The left picture shows a view perpendicular to the beam pipe. The right figure illustrates a cross section parallel to the beam direction. The lever arm inside the magnetic field is 2.9 m.

Z-chambers determine the r-θ coordinates. The calculation of the track curvature from the r-ϕ coordinates results in a measurement of the transverse momentum. For muons passing all three P-segments, the triplets, this is done using the sagitta, S, which is illustrated in figure 2.9.

The sagitta, defined as the deviation of the middle P-segment from the straight line connecting the inner with the outer segment, has to be determinend with a precision approaching 70 μm to reach a momentum resolution of $\sigma_p/p \simeq 2\%$ for a 50 GeV muon track [63]. The 3-momentum of the muon can be calculated by including the θ measurement in the Z-chambers.

Muons reaching the spectrometer with a momentum greater than 3 GeV are confined to a single octant. Therefore the alignment is done only between chambers of one octant. The alignment is achieved and controlled by independent LED and laser systems. This ensures an internal alignment of better than 30 μm. A single wire resolution of about 200 μm has been estimated with cosmic ray tracks [63, 76]. This provides an intrinsic sagitta resolution of 60 μm.

For tracks crossing only two layers, called doublets, the transverse momentum is reconstructed from the difference of the track slopes inside the drift cells, which are measured to an accuracy of 1 mrad.

The momentum resolution for 45 GeV triplets is about 2.5% [76, 77]. For doublets the resolution drops to about 20% [77].

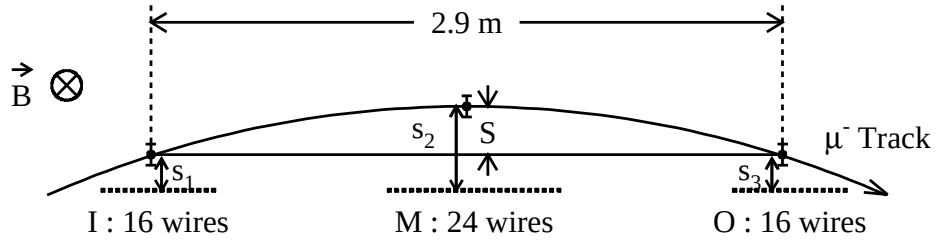

Fig. 2.9: Illustration of the sagitta method, which allows transverse momenta measurement.

2.2.6 The Luminosity Monitor

A precise measurement of the luminosity is obtained by selecting low angle Bhabha events and comparing the measured rate with a precise theoretical calculation of the cross section [78]. At L3, two electromagnetic calorimeters and two sets of silicon trackers (SLUM) measure the energy and angles of the scattered electrons and positrons. They are arranged symmetrically on each side of the interaction point and cover the 25 mrad ≤ 0 and $(\pi - \theta) \leq 70$ mrad polar angle range. Each calorimeter is an azimuthally symmetric array of 304 BGO crystals of the same shape and dimensions as used in the barrel electromagnetic calorimeter. Every crystal is read out by a photodiode and has a LED to monitor the stability of the energy measurement. The energy resolution for electromagnetic showers is 1.3% at 45 GeV, the angular resolution is 0.4 mrad in θ and 8.7 mrad in ϕ.

2.2.7 The L3 Trigger System

Only a few events per second are produced in e^+e^- collisions at the interaction point. This rate is small compared to the beam crossing rate of LEP[6]. After each beam crossing, the L3 trigger system decides whether an event should be recorded or not. To

[6] The revolution frequency of 11.24 kHz [79] for beam particles at LEP corresponds to a beam crossing rate of about 45 kHz, if the beams are modulated in 4 bunches.

minimise the dead time, the decision is taken in a three-level process with increasing complexity at each level.

Level-1 Trigger: The level-1 trigger is based on separate subdetector triggers, each gated by the beam crossing signal. The main four parallel triggers are:

- **Energy trigger:** The energy trigger makes decisions based on the value and the topology of the energy deposition in ECAL, HCAL and luminosity monitors [80–82].
- **TEC trigger:** The TEC trigger is based on the number and relative orientation of charged tracks [83].
- **Scintillator trigger:** The signals of scintillation counters are used to select high multiplicity events.
- **Muon trigger:** The muon trigger responds if there is at least one track in the muon spectrometer.

If any of them has a positive decision the event is digitised. If the level-2 decision is negative, all electronics is cleared and prepared for the next event. The typical trigger rate of a level-1 trigger is less than 8 Hz.

Level-2 Trigger The level-2 trigger [84] analyses events selected by the level-1 trigger. It correlates level-1 trigger decisions and uses additional information, not available in time at the preceeding trigger level. In particular, information on the vertex along the beam axis using the charge division measurement from the TEC, energy depositions in calorimeters correlated in a coarse $\theta - \phi$ map and longitudinal and transverse energy imbalance arising from the energy measurement are used. Each event with more than one positive level-1 trigger passes the level-2 unhindered. The combination of the coarse signals of the different subdetectors allows to reject background like beam-gas events, beam-wall interactions, synchrotron radiation and calorimetric noise. The data from all subdetectors is collected by the event builder and passed to the level-3 trigger if an event is accepted in level-2.

Level-3 Trigger Unlike the previous two levels, level-3 trigger [85] has access to the complete digitised data with finer granularity and higher resolution. At first the data is validated, then the calorimetric energy and the time-of-flight measured by

the scintillators are determined. A partial pattern recognition of tracks in the TEC is performed and correlations between TEC tracks and calorimetrical clusters are searched for. Thresholds and other requirements are defined more precisely, leading to a further suppression of the background. Events with more than one positive level-1 trigger result are always accepted as well as luminosity events. The final trigger decision is based on the overall event characteristic. The level-3 trigger does not introduce any additional dead time and allows an overall event writing rate of about 5 Hz.

Chapter 3

PHYSICS CAPABILITIES IN L3

Any experimental analysis abstracts the physical observables from the raw information measured by the detection device. The subject of physics carried out with particle detectors are particles. Beside the properties of a single particle the reconstruction of the particle production or decay chain is of interest. By grouping several particles belonging to a certain physics process into an *event* allows for a better study of interaction processes. An event at LEP consists of the particles generated in electron-positron annihilation and their decay products. These particles, which manifest themselves in different ways in the various subdetectors, have to be reconstructed and identified. Due to the complexity of the detector the translation of the raw detected information into observables, describing the different particles and finally the event, is expendable. For this translation a detailed simulation of the detector and the expected physical effects by the Monte Carlo technique is mandatory.

In the following chapter the event reconstruction and some aspects of particle identification in L3 are introduced as well as the detector simulation.

3.1 Event Reconstruction

Subdetectors provide only specialised information for traversing particles. To reconstruct the four-momenta of all detected particles and finally the whole event a reconstruction procedure is applied. This involves several levels and starts with the data acquisition system (DAQ). The DAQ consists of parallel data streams from CTS, ECAL, HCAL and the muon spectrometer, completed by a separate stream of trigger data. Combination of all data into one single event record enables an event based monitoring and analysis. Next, the digitised information from the DAQ is evaluated separately for every subdetector to reconstruct objects like tracks and calorimetric clusters. This abstraction allows to structure the information and reduces the number

of parameters to describe the event. The objects are very helpful to distinguish between different particles and events. A brief description of main objects used in this analysis follows.

Tracks Tracks are reconstructed for charged particles traversing the central tracking system or the muon spectrometer.

In the central tracking system the reconstruction starts with the signals collected by the anode wires of the TEC, the hits. For every hit the drift distance is derived from the drift time and a pattern recognition algorithm applied to group hits, presumably induced by the same particle, in form of tracks in the r-ϕ plane. A fit is performed for every track to determine the curvature, the distance of the closest approach (DCA) to the reference point, given by the e^+e^- interaction point, and the azimuthal angle within the bending plane. Finally, hits of the SMD and the Z-detector are assigned and the track is fitted to a helix in three dimensions. This provides the polar angle and the DCA in the r-θ plane.

Charged particles reaching the muon spectrometer can produce hits in the muon chambers. These hits are grouped into segments in each layer. If at least two segments in P-chambers can be associated with a common origin, a track is formed. For every track the momentum and space coordinates of the particle are determined. The backtracking to the interaction region gives the DCA, the polar and azimuthal angles. An average energy loss of the track in the material is calculated. The momentum at the interaction region is determined from the energy loss and the momentum measured in the spectrometer.

ECAL bumps The energy depositions in the ECAL are searched for neighbouring[1] fired crystals with a local maximum of energy deposition. A group of crystals with a total energy greater than 40 MeV forms a bump. The most energetic crystal is taken as a centre for a 3×3 or 5×5 crystal matrix. The energy is summed up for all crystals of a matrix. Assuming an electromagnetic origin of the bump, an electromagnetic shower shape is fitted to the bump, applying leakage and impact point dependent corrections. This provides the bump energy and the compatibility with an electromagnetic origin of the bump. The impact point of the particle is calculated from the energy weighted centre of gravity of the 3×3 matrix.

[1] Neighbouring crystals have a common corner or edge.

HCAL clusters A cluster in the HCAL is formed by at least two geometrically connected hits, given by energy deposition in the readout towers. Each cluster is characterised by its total energy and geometric position. A shower shape is given by the transverse and longitudinal profiles of a cluster, allowing to discriminate clusters of hadronic from non-hadronic origin.

Reconstruction across L3

Associations are made between objects in different subdetectors to produce more general objects and to calculate the kinematic variables that characterise the particles and finally the event. Logical objects can correspond to particles like muon candidates. These objects consist of a track in the muon spectrometer and in the CTS with associated clusters in the HCAL and energy depositions in the ECAL. The "smallest resolvable clusters" (SRC) are constructed from ECAL bumps with HCAL clusters behind, seen from the interaction region. The resolved SRCs are treated as particles and a rough energy measurement is then applied to determine a 3-momentum vector, with the magnitude given by the total energy and the direction determined by an energy-weighted average of the positions of its components.

An event thrust axis is then calculated as the unit vector $\vec{n}_T$ maximising the following sum

$$\sum_i \mid \vec{p}_i \cdot \vec{n}_T \mid$$

where $\vec{p}_i$ is the 3-momentum of the i-th muon candidate or SRC in the event. The total visible energy in the event is given by the sum of all SRC energies and muon candidates momenta.

3.2 Particle Identification

Particle identification is obtained from the different responses in the subdetectors. For example a charged particle like an electron is measured with the central tracking system and in the calorimeters while neutral particles like the π^0-mesons or photons are detected in the calorimeters only. Combining the information of all the subdetectors allows to discriminate between different particles. The following signatures are the basis for most of the selection and identification criteria used in this analysis.

Electron signature Electrons are measured as a CTS track matched to an electromagnetic shower in the ECAL. For particle energies greater than 1 GeV the shower shape is energy independent [86]. The shower is symmetrical and most of the energy is deposited in a 3×3 BGO crystal matrix around the shower maximum. Electrons are absorbed by the ECAL but a small fraction of the shower can leak into the HCAL at higher electron energies.

Muon signature Muons are heavier than electrons and penetrate matter without showering. Their ionisation is near the minimal one, they are, therefore, denoted as minimum ionising particles (MIP). The MIP energy deposition in the calorimeters is about 2-3 GeV and nearly independent of the muon energy. An ECAL bump from a traversing muon consist of a few crystals only. The hits in the HCAL build a long and thin line matching a CTS track. Muons with momenta below 3 GeV can be absorbed by the calorimeters. Most of the muons reach the muon spectrometer where a track is reconstructed.

Hadron signature Hadrons are measured in both calorimeters. Compared to an electromagnetic shower shape the ECAL shower of hadrons is less narrow and not necessarily rotationally symmetrical. For charged hadrons a CTS track can be matched to the ECAL bump. Hadrons are absorbed by the HCAL where they produce widely distributed hits.

Photon signature Photons deposit all their energy in the ECAL. They are detected as a single bump in the ECAL with no matching objects in the remaining detectors. Photon showers overlapping with charged hadron showers are reconstructed by an iterative procedure. The energy deposition which is assigned to the charged hadron is subtracted and photons are identified from the remaining neutral bumps.

3.3 Detector Simulation

Any physical interpretation of the detected signals requires a detailed understanding of the detector. The Monte Carlo (MC) technique is used to simulate the detector response to different particles or physical processes. This facilitates to determine acceptances and efficiencies, background rates and systematic effects. Selection criteria for the isolation of certain classes of events are optimised using the simulated detector information.

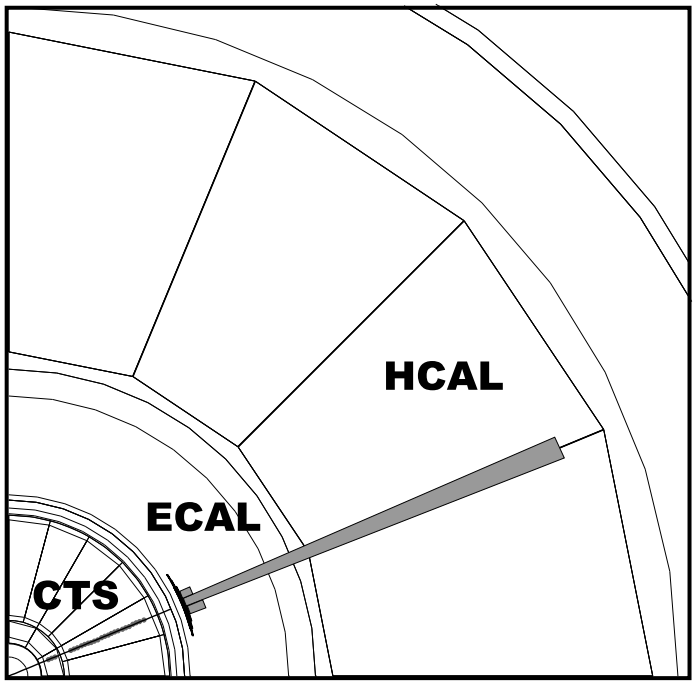

Fig. 3.1: A typical electron in the L3 detector. A track in the CTS points to a narrow energy deposition in the ECAL.

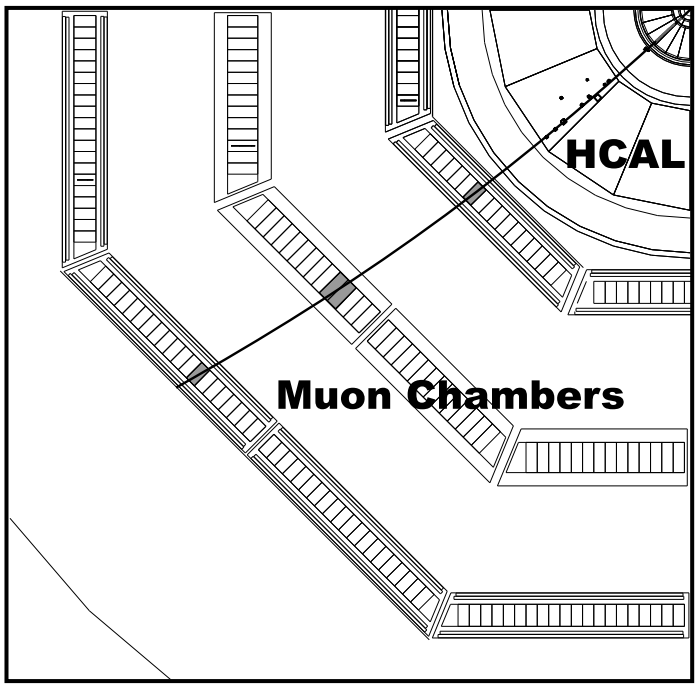

Fig. 3.2: A typical muon as seen with the L3 detector. A track is reconstructed in the CTS and in the muon chambers. The energy deposition in the calorimeters is minimal.

The Monte Carlo event simulation starts with the generation of events on the base of theoretical predictions. The output are final state particles with their four-momenta. In the next step the long-living particles are propagated through the L3 detector, taking into account the response of the detector elements for each particle. This includes the interactions in the detector materials, e.g. multiple scattering, energy loss or shower development, taking into account the influence of the magnetic field [87]. The decay of particles and hadronisation processes are included too. To get a more realistic description of the detector response imperfections like inefficiencies, noise and offsets of subdetectors are considered.

The result of this simulation is the digitised data of active elements of the detector, which is the input for the off-line reconstruction program. The event reconstruction is identical for Monte Carlo and data.

Part II

MEASUREMENT OF TAU LEPTONIC BRANCHING FRACTIONS

Chapter 4

METHOD OF MEASUREMENT

This chapter describes how the τ leptonic branching fractions can be measured at LEP. The advantage of single hemisphere tagging is discussed.

4.1 Tau Leptonic Branching Fraction Measurement at LEP

The annihilation of an electron and a positron into a τ pair (chapter 1.4) is the dominant source for τ production at LEP. Due to its short lifetime the τ decays before it reaches the first inner detector. Thus τ leptons manifest themselves by means of their decay products in the detector. The individual signatures of the decay products make it possible to distinguish between the different τ decay modes. The branching fraction B_x for the decay into x is determined from the number of these decays, N_x, normalised to the number of decays for all decay modes, N_τ,:

$$B_x = \frac{N_x}{N_\tau} \, . \tag{4.1}$$

An obvious way to get the total number of decays would be to select the different decays exclusively and to count them. The branching fraction is then given by:

$$B_x = \frac{N_x}{N_x + N_{\not x}} \, , \tag{4.2}$$

with $N_{\not x}$ as the number of decays of all decay modes except the studied one.

Another method is the inclusive selection of τ events for all decay modes, based on properties of the τ production process or a common signature for all τ decays. Table 4.1 compares both methods with respect to the influence of the error on the number of decays.

Method	Inclusive τ sample	All decays identified exclusively
	$B_x = \dfrac{N_x}{N_\tau}$	$B_x = \dfrac{N_x}{N_{\not x} + N_x}$
ΔB_x^2	$\dfrac{1}{N_\tau^2}\,\Delta N_x^2 + \dfrac{N_x^2}{N_\tau^4}\Delta N_\tau^2$	$\dfrac{N_{\not x}^2}{(N_{\not x}+N_x)^4}\,\Delta N_x^2 + \dfrac{N_x^2}{(N_{\not x}+N_x)^4}\,\Delta N_{\not x}^2$
$\Delta B_x^2 N_\tau^2$	$\Delta N_x^2 + \quad B_x^2 \quad \Delta N_\tau^2$	$(1-B_x)^2 \quad \Delta N_x^2 + \quad B_x^2 \quad \Delta N_{\not x}^2$
$B_x = 0.2$	$1 \quad \Delta N_x^2 + \quad (0.2)^2 \quad \Delta N_\tau^2$	$(0.8)^2 \quad \Delta N_x^2 + \quad (0.2)^2 \quad \Delta N_{\not x}^2$

Tab. 4.1: Error of the branching fraction in dependence on the error of the number of decays. The errors are assumed to be uncorrelated. The lowest line gives the factors for the errors for an hypothetical branching fraction of 0.2, which is of the same order as the τ leptonic branching fractions.

Error propagation provides that the errors ΔN_τ and $\Delta N_{\not x}$ have to be multiplied with the fraction B_x when calculating the error on the branching fraction ΔB_x. The relative contribution of ΔN_x is dominant for both methods[1]. For the inclusive method the error on N_x enters without suppression, while it is reduced by B_x for the exclusive method. Thus, the exclusive method provides smaller errors if ΔN_τ and $\Delta N_{\not x}$ are of the same order, and all errors are uncorrelated. However, for the inclusive method N_x is a subsample of N_τ and the statistical error has to be calculated as standard deviation of a binominal distribution [88]

$$\Delta B_x^2 = \frac{1}{N_\tau} B_x\,(1 - B_x)\ . \tag{4.3}$$

Furthermore, the exclusive method requires the knowledge and identification of all decay modes. Each identification introduces systematic effects which can add up to a large $\Delta N_{\not x}$. All identification efficiencies have to be determined, while for the inclusive method only the τ selection has to be studied.

Therefore, smaller errors on B_x are expected for the inclusive method if the selection of an inclusive sample and the identification of the decay x is achieved with high efficiencies.

[1] For this estimation the leptonic branching fractions are taken as 20 percent.

An advantage at LEP is that τ leptons are produced pairwise. The special characteristics of these events can be exploited to select an inclusive τ sample. The leptonic τ decays $\tau \to e\bar{\nu}_e\nu_\tau$ and $\tau \to \mu\bar{\nu}_\mu\nu_\tau$ are then recognised by identifying the electron or muon.

Therefore the measurement of the τ leptonic branching fractions is subdivided into two parts:

- selection of a $\tau\tau$ sample,
- identification of a purely leptonic τ decay.

The ideal situation is the selection of a class of events, the signal, unambiguously and without losses. But usually corrections to the number of events in a selected sample, containing N_{All} events, have to be applied. One is the contamination from other processes, the number of background events, N_B, which is in the following given by its fractions f:

$$f = \frac{N_B}{N_{All}} = \frac{N_B}{N_B + N_S} \,. \tag{4.4}$$

Here N_S is the number of the selected signal events.

The second is the acceptance for the signal, characterised by the efficiency ε. It is calculated from the number of signal events before the selection, N_{Signal}, and N_S:

$$\varepsilon = \frac{N_S}{N_{Signal}} \,. \tag{4.5}$$

The branching fractions can now be obtained through the expression

$$B_l = \frac{N_l(1 - f_l^{non-\tau})(1 - f_l^{\tau\nrightarrow l})}{2N_{\tau\tau}(1 - f_{\tau\tau}^{non-\tau})} \frac{1}{\varepsilon_l^{ID}} \frac{\varepsilon_{\tau\tau}^{sel}}{\varepsilon_l^{sel}} \tag{4.6}$$

with:

N_l	-	number of identified leptons,
$f_l^{non-\tau}$	-	fraction of identified leptons from non-τ events,
$f_l^{\tau\nrightarrow l}$	-	fraction of other τ decays, misidentified as leptons,
ε_l^{ID}	-	efficiency of lepton identification,
$N_{\tau\tau}$	-	number of selected $\tau\tau$ events
$f_{\tau\tau}^{non-\tau}$	-	fraction of non-τ events in the $\tau\tau$ sample,
$\varepsilon_{\tau\tau}^{sel}$	-	efficiency of $\tau\tau$ selection for all τ decays,
ε_l^{sel}	-	efficiency of $\tau\tau$ selection for the leptonic τ decay.

All the corrections to N_l and $N_{\tau\tau}$ are sources for systematic errors in the branching fraction measurement. The corrections are usually estimated from Monte Carlo, implying, that the detector is well described. The validity of the above has to be checked carefully. This is done by taking the corrections from data itself, what is not possible in all cases. For the remaining ones the agreement between data and Monte Carlo simulation can only be controlled for parts of the information used, like distributions of observables from which the selection criteria are defined. But even if single distributions agree their combination could still be different in data and Monte Carlo. Therefore a better way is an optimisation of the selection method to reduce such corrections as much as possible.

Since the L3 detector permits a good separation between $N_{\tau\tau}$ and other events, small background fractions can be obtained. In addition, the background processes are well known and their Monte Carlo simulation can be compared to separately selected data samples. These control data samples are more difficult to select for the case of the efficiencies quoted in expression 4.6. While the lepton identification can be checked with leptons produced in other processes, a completely independent τ sample can not be selected with sufficient efficiency. Therefore the ratio $\varepsilon_{\tau\tau}^{sel}/\varepsilon_l^{sel}$ is obtained from Monte Carlo only. This correction takes into account that the τ selection can enrich a certain decay mode and lead to a bias in the measurement. The efficiencies for selecting τ decays reached in other L3 measurements are in the order of $60-80$ percent (see for example [89]) and differ for the different decay modes. Even if applying an inclusive τ selection, the expected values $\varepsilon_{\tau\tau}^{sel}$ and ε_l^{sel} should be of the same order for the selection of a certain decay mode. Thus any deviation between data and Monte Carlo in the observables the selection criteria are based on can induce a non-negligible systematic error of a few percent.

A way to avoid this error is a selection which does not change the ratio of different τ decay modes. This is achieved by the method introduced below.

4.2 Single Hemisphere Tagging

The τ leptons produced at the centre-of-mass energies around the Z mass are highly boosted[2] in opposite directions and decay inside the detector. This back-to-back topology allows to assign a hemisphere to each decay. Since the two τ leptons decay

[2] $E_\tau = E_{Beam} >> m_\tau$

independently, performing the τ selection in one hemisphere only will leave the other hemisphere untouched. This avoids the enrichment or the reduction of leptonic decays and resulting biases for the measurement. The branching fraction can be measured without the precise knowledge of the efficiencies of the τ selection. This principle of *single hemisphere tagging* demonstrates figure 4.1.

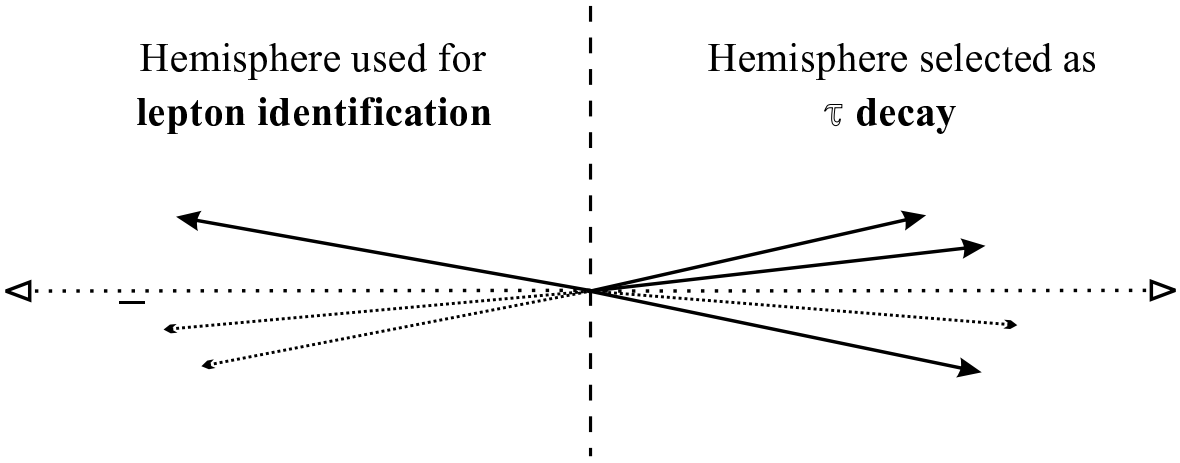

Fig. 4.1: The single hemisphere tagging for a $\tau\tau$ event. The right hemisphere ($\tau \to \pi\pi\pi\nu$) is selected as a τ decay and used to tag the event as a τ pair. This hemisphere is referred to as the *tagging* hemisphere, while the other is the *tagged* one. The lepton identification is carried out in the tagged hemisphere only.

The event is divided into two hemispheres, containing one τ decay each. If a hemisphere is identified as a τ decay the event is tagged and the lepton identification is carried out in the other hemisphere. This allows to study the τ decays in a sample almost unaffected by the τ selection.

Each event is tagged in both hemispheres independently.

Chapter 5

SELECTION OF THE TAU SAMPLE

A sample of $Z \to \tau^+\tau^-$ events is selected in a successive procedure starting with the total data sample recorded with L3. Since this signal is only a small amount of the data one has to find a way to distinguish between the signal and the background events. This is usually done by defining requirements to observables or combinations of observables which describe the signature of the process.

The first step is the preselection of low multiplicity events. The resulting sample contains almost all events with two leptons in the final state, i.e. e^+e^-, $\mu^+\mu^-$ and $\tau^+\tau^-$ final states. The preselection rejects most of the background from hadronic Z decays, cosmic rays and beam gas interactions. Each of the remaining events is separated in two hemispheres by a plane perpendicular to the event thrust axis.

For the subsequent selection of $\mathrm{Z} \to \tau^+\tau^-$ events the selection criteria can be divided in two classes. In the first one the properties of the whole event are used. The requirements applied to observables are named *correlated* cuts because they affect both hemispheres simultaneously. The other class are requirements in one hemisphere only, used for hemisphere tagging.

Every hemisphere is considered as τ decay if it fulfils some criteria derived for a typical τ decay and is inconsistent with background. This background comes mainly from two-photon scattering events ($\mathrm{e^+e^- \to e^+e^-f\bar{f}}$), Bhabha events ($\mathrm{e^+e^- \to e^+e^-}$), dimuon events ($\mathrm{e^+e^- \to \mu^+\mu^-}$), cosmic muons, and low multiplicity hadronic Z decays. For each of these event classes special hemisphere cuts are applied as described in the following chapters preceeded by a description of the preselection. The selection is restricted to the central barrel part of the detector. This reduces the acceptances of $\tau^+\tau^-$ events to 60 %.

5.1 Dilepton Preselection

In this analysis only dilepton final states are used for the measurement and the systematic studies. Hadronic Z decays which are characterised by a large charged track multiplicity are rejected by the following requirements:

- The total number of tracks is less than 9.
- The number tracks in any hemisphere is less than 6.
- The number of ECAL clusters is less than 26.

Cosmic muon events do normally not origin from the interaction region. They are reduced by requiring at least one track to pass the interaction region within 5 mm in the r-ϕ plane.

Background from two-photon interactions is suppressed demanding:

- at least one track with a transverse momentum greater than 1 GeV.
- the transverse energy imbalance to be larger than 3 GeV if the acollinearity[1] between any two tracks is smaller than 54°.

5.2 Selection of the Tau Sample

After the preselection only 25 percent of the data sample are $\tau\tau$ events. Therefore the background is large. But since it is well known most of it will be reduced in the τ selection procedure which is described in the following.

5.2.1 Principles of the Tau Selection

Due to the high boost the τ decay products are tightly collimated within a cone of a few degrees. The dominant τ decay modes are the 1-prong[2] and the 3-prong topology with $84.71 \pm 0.13\%$ and $15.18 \pm 0.13\%$ [90], respectively. In the hadronic τ decay modes charged particles can be accompanied by neutral hadrons. In addition, radiative photons occur.

[1] The acollinearity is defined as space angle between two tracks. Its maximum is π if the tracks are back-to-back.

[2] Prong stands for the number of charged particles.

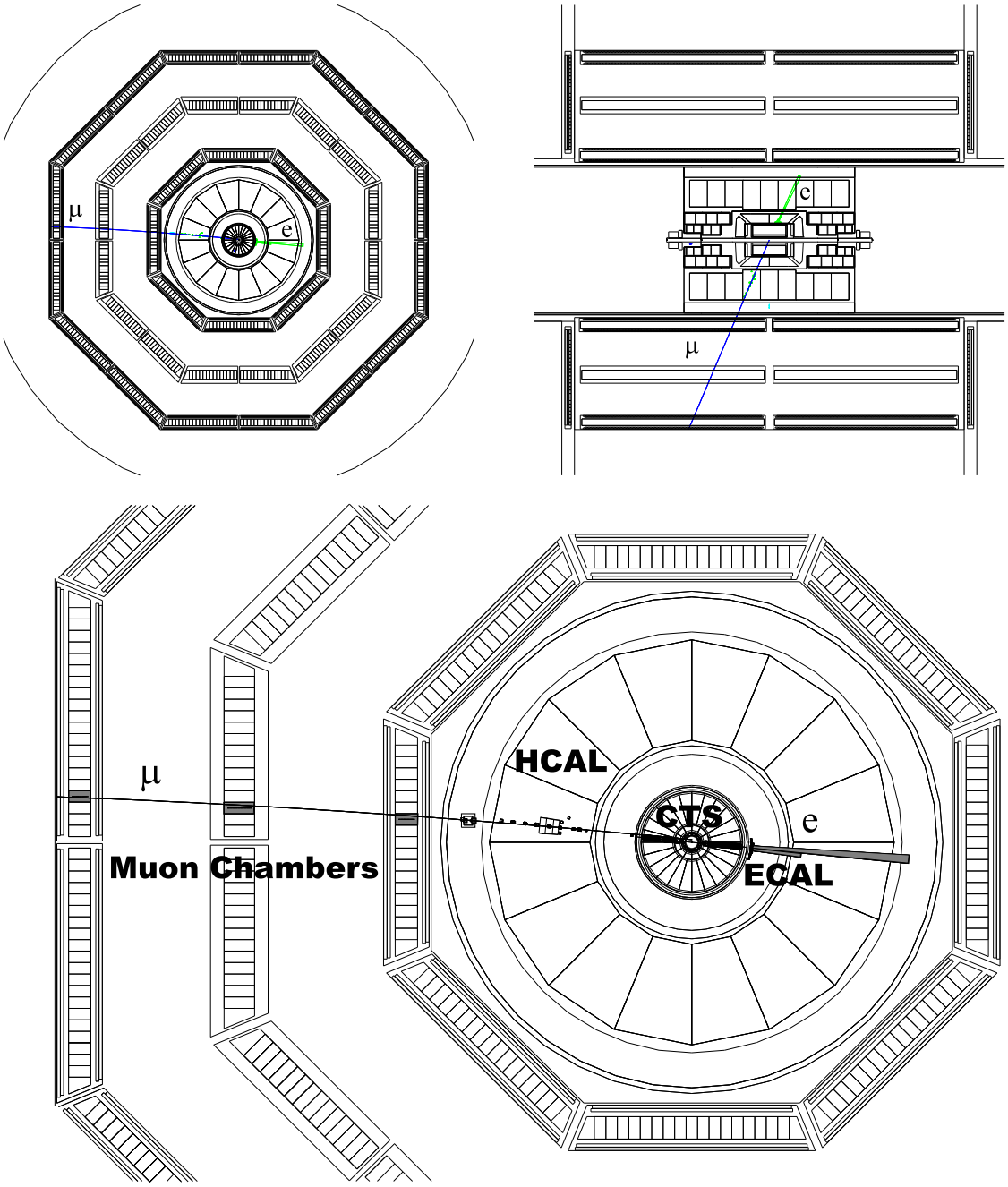

Fig. 5.1: View of a $\tau\tau$ event seen in L3. One τ decays into a muon, the other into an electron. The upper figures show the end view (left) and the side view (right) of the detector. Below is a zoomed cross section of the detector showing both tracks with the electron shower in the ECAL on one side and the MIP signature on the other.

Thus the typical $\tau\tau$ event at LEP contains two low multiplicity jets of at least one charged particle which are almost back-to-back and highly collimated. The neutrinos, which are produced in τ decays are not seen in the detector. Therefore the detected decay products do not carry the whole energy of the τ, which is around 45 GeV. Figure 5.1 shows a $\tau\tau$ event seen in L3.

The preselected data sample contains in addition to Z $\rightarrow \tau^+\tau^-$ events:

- direct Z decays into e^+e^-, $\mu^+\mu^-$ ($\sim 50\%$),
- two-photon events ($\sim 20\%$),
- muons from cosmic rays,
- low multiplicity hadronic Z decays.

Each class has some typical properties which help to separate them from the $\tau\tau$ events.

The direct Z decays manifest themselves as two leptons e or μ of the same generation. They have opposite momenta and their energy is approximately equal to the beam energy. If the final state lepton radiates a photon, the energy for the two leptons is different.

The events from two-photon interactions, $e^+e^- \rightarrow e^+e^- f\bar{f}$, are characterised by a low scattering angle of the outgoing electron and positron which carry a large fraction of the beam energy and mostly escape undetected. The $f\bar{f}$ pair tends to have low energy, a small transverse momentum and may have large acollinearity. The acoplanarity[3] is small because of low transverse and opposite momenta of the two photons.

The cosmic muons not rejected in the preselection pass the detector close to the interaction region. Such muons are reconstructed as two particles coming from the interaction region and carrying opposite charge (figure 5.2). The energies are equal and the acollinearity is maximal. These cosmic muons are not necessarily in time with the beam crossing.

The ideal case for the measurement of the leptonic branching fraction would be to perform the selection of $\tau\tau$ events by using only one hemisphere as expatiated to the single hemisphere tagging method in 4.2. But since here only a part of the information is used this method has a lower potential to reduce the background. Exploiting both hemispheres it is easy to distinguish, e.g. between a Bhabha event with two high

[3] The angle included by two tracks in the r-ϕ plane reduced by π.

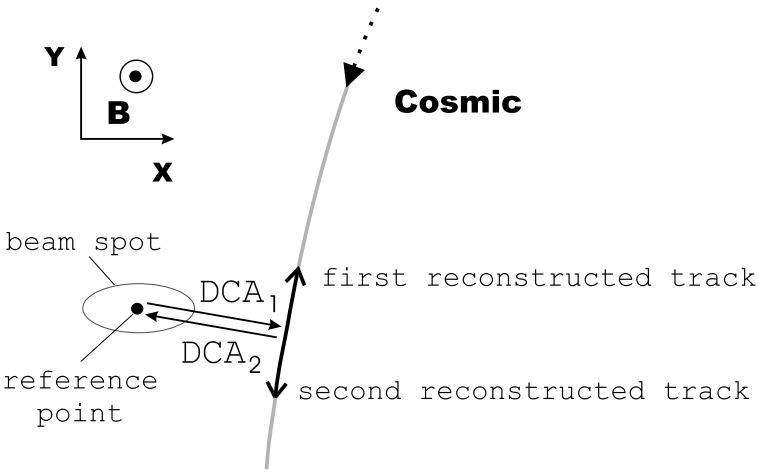

Fig. 5.2: The reconstruction of a cosmic muon in the CTS. The figure corresponds to a cross view of the L3 detector in the bending plane. The origin of the coordinate system is at the nominal vertex. The muon passing the detector is reconstructed as two tracks with opposite momenta and opposite charge. The DCA depends on the track direction related to the beam spot and is therefore anticorrelated too.

energetic back-to-back electrons from a $\tau\tau$ event, where one τ goes to an high energetic electron and the other one to a hadron or muon. Looking only for one hemisphere makes it very difficult to decide how the electron was produced.

Low background fractions are necessary to keep the resulting systematic error small. To achieve that without rejecting all events which can not be identified unambiguously in one hemisphere only, hemisphere tagging is combined with correlated cuts in a special way. The correlated cuts are carefully chosen to have a negligible influence on the ratio of the different τ decays. This is achieved by placing the correlated cuts in regions where they reject almost no signal. If such an adjustment of the cut is not possible, the cut is applied as a *dedicated* correlated on a subsample only. In this subsample the background is enriched by hemisphere cuts. Thus the dominant part of the τ sample is selected by cuts in the tagging hemisphere, and the inefficiency resulting from correlated cuts is small.

5.2.2 Identification of Tau Pair Events

Based on the typical signature the following requirements for the $\tau\tau$ event are derived:

- There must be one to three tracks in the selection hemisphere[4].
- The maximum opening angle between a track and the thrust axis must be lower than 25 degrees (figure 5.3).
- The acollinearity of the two leading[5] tracks in each hemisphere must be larger than 2.8 rad.
- The acoplanarity angle must be larger then 0.005 rad. This cut is applied as a dedicated correlated cut.

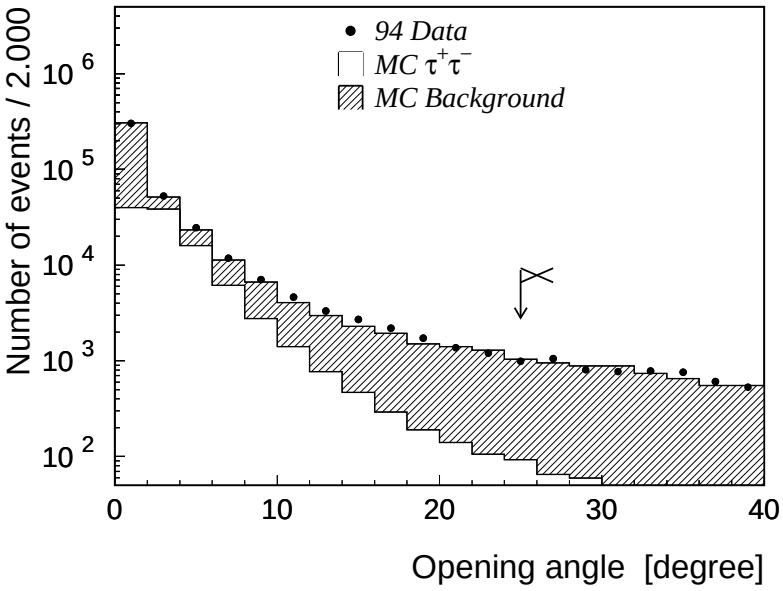

Fig. 5.3: The maximum opening angle between a track and the thrust axis. The figure shows the distribution after the preselection. Data and Monte Carlo prediction are in good agreement for the region where the cut is placed.

[4] For about 10 percent of the 3-prong τ decays only two tracks were reconstructed.

[5] The *leading* track is the track with the highest momentum.

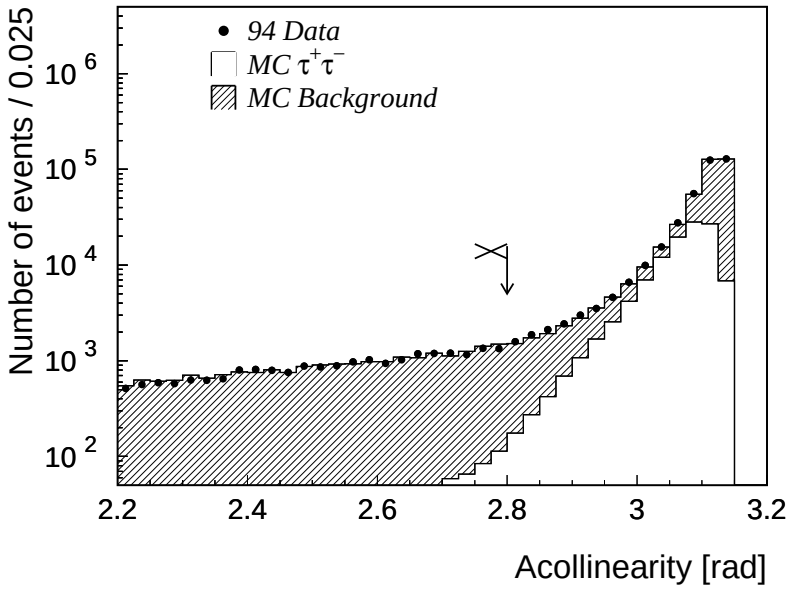

Fig. 5.4: The acollinearity distribution, after the preselection. Data and Monte Carlo prediction agree very well. The cut, indicated by the arrow, has a negligible influence on the signal.

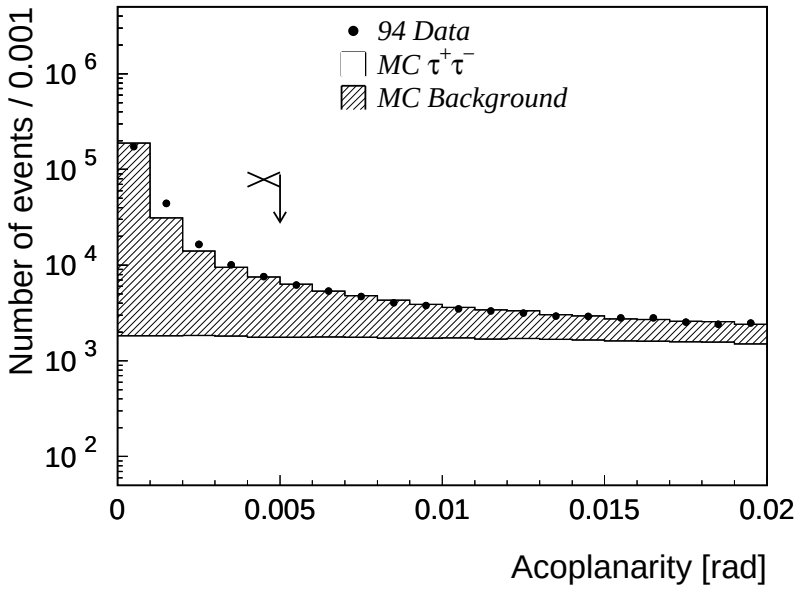

Fig. 5.5: The acoplanarity distribution, after the preselection. At very low acoplanarities, where Bhabha and dimuon events are dominating, the Monte Carlo describes the data not very well. This is mainly caused by a poor CTS measurement.

The cut on the acollinearity (see figure 5.4) has a very small impact on the signal[6]. The deviation between data and Monte Carlo distributions at low acoplanarity (figure 5.5) is due to Bhabha and dimuon events mainly. In the region of the cut value the agreement between data and Monte Carlo is good. The distribution for the signal is almost flat. Therefore the disagreement affects the background mostly. Nevertheless, to minimise the inefficiency for the signal, the cut on acoplanarity is applied as dedicated correlated cut for subsamples only, as explained in subchapter 5.2.1. The hemisphere cuts to select the subsamples are derived for each background separately.

In all plots the Monte Carlo simulation for the $\tau\tau$ events is normalised to luminosity, while the background normalisation is obtained from data distributions.

5.2.3 Cosmic Muon Background

Cosmic muons passing the interaction region can survive the preselection. Because these muons are reconstructed as two muons going in opposite directions (figure 5.2), the both DCA should be equal, except of the sign. They build a band around $\mathrm{DCA}_1 = -\mathrm{DCA}_2$, as shown in figure 5.6.

Out-off-time cosmic ray events can be discriminated using the time information from the scintillation counters. The measured event time of $\tau\tau$ events is correlated with the beam crossing, whereas cosmic muon hit the detector permanently.

To suppress cosmic muons at least one |DCA| should be smaller than 2 mm. In the tagging hemisphere it is required that the |DCA| is smaller than 1 mm and the event time measured by the scintillation counters lies within 5 ns after the beam crossing. To keep the inefficiency for the $\tau\tau$ sample small, this cut is applied only if the calorimetrical energy in the tagging hemisphere is compatible with a MIP signature:

- The HCAL cone energy[7] energy $\mathrm{E}^{\mathrm{cone}}_{\mathrm{HCAL}}$ is smaller 6 GeV and
- the ECAL cone energy $\mathrm{E}^{\mathrm{cone}}_{\mathrm{ECAL}}$[8] is smaller 5 GeV.

[6] Only 0.5 percent of the preselected $\tau\tau$ events have an acollinearity smaller than 2.8 rad as estimated from Monte Carlo.

[7] *Cone energy* is the energy sum in a cone of a half-angle size of 30 degrees around the track.

[8] $\mathrm{E}^{\mathrm{cone}}_{\mathrm{ECAL}}$ sums over the ECAL energy without fitting bumps.

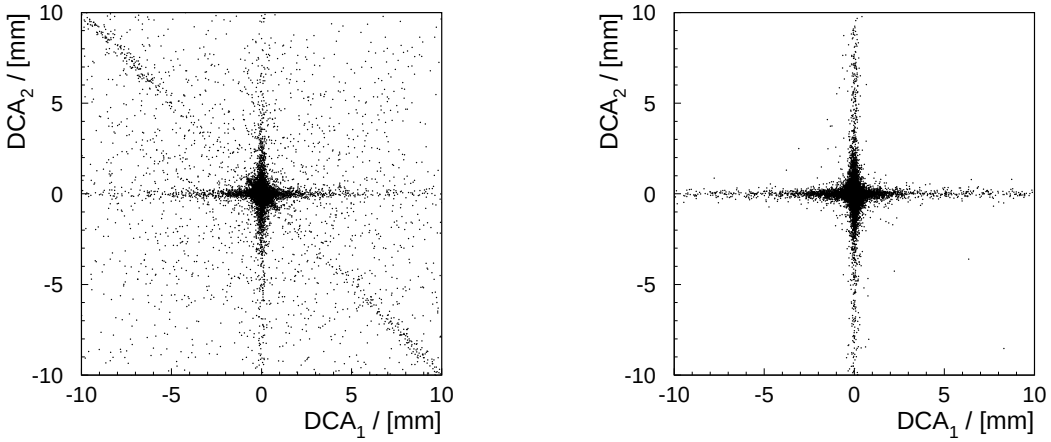

Fig. 5.6: The DCA distribution, after the preselection and the cuts on acollinearity and maximum opening angle. The DCA of the leading track in one hemisphere (DCA_1) is plotted against the DCA of leading track in the other hemisphere (DCA_2). The left plot is for data, the right one for signal Monte Carlo. The band around $DCA_1 = -DCA_2$ caused by cosmic muons is clearly visible.

5.2.4 Background from $e^+e^- \to e^+e^-$

A typical Bhabha event leaves two clear electromagnetic bumps in the ECAL in each hemisphere, with an energy close to the beam energy E_{beam}. Most of the Bhabha events are rejected by cutting all events with an ECAL bump energy, E_{ECAL}^{bump}, of more than 0.75 E_{beam} in the tagging hemisphere. Figure 5.7 gives the distribution of E_{ECAL}^{bump} in the region around the cut.

For the remaining Bhabha events only small or even no ECAL energy is measured in the tagging hemisphere for physical reasons or due to detector imperfections:

- There is bremsstrahlung before (initial state) or after (final state) the annihilation. The signature of these electrons is very similar to electrons from $\tau \to e\bar{\nu}\nu$.
- The electron hits bad regions of the ECAL like dead crystals or cracks[9] between crystals. The reconstructed ECAL bump is therefore not of the typical electromagnetical form, and these electrons tend to deposit some energy in the HCAL.

[9] Cracks are regions within the geometrical acceptance of the ECAL that are not covered by crystals. Thus no measurement is performed.

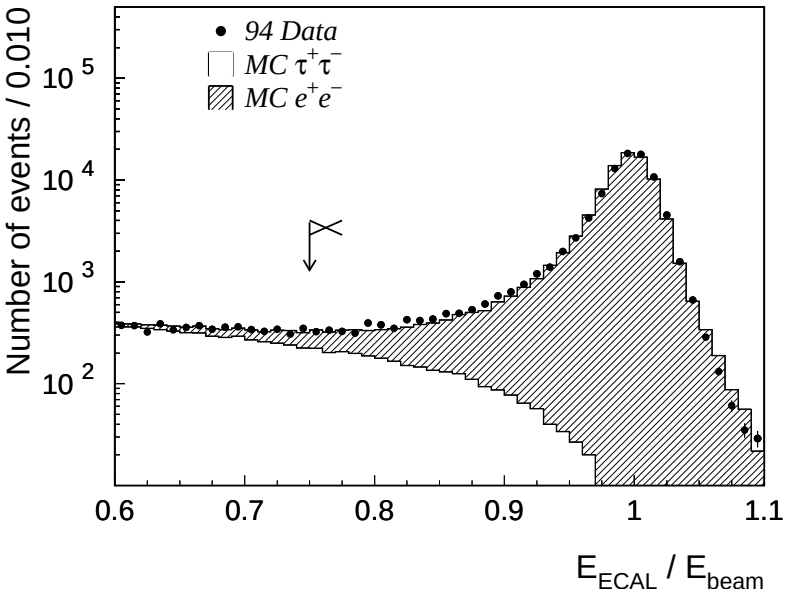

Fig. 5.7: The ECAL bump energy of the leading track, after the preselection. The arrow gives the nominal cut value.

The following requirements for a loose electron[10] are applied to one hemisphere:

- There is one track.
- There are not more than 3 bumps in the ECAL.
- The momentum from the CTS is compatible with the energy from the ECAL, or the shower in the ECAL is of an electromagnetic nature.
- There is no response in the muon spectrometer and muon filter.

They are fulfilled by the remaining Bhabha events but by electrons and even low energetic pions from τ decays too. In this loose electron sample the Bhabha electrons are more energetic than selected tracks from decaying τ leptons. Thus demanding a minimum energy for the track momentum, P_{CTS}, or the ECAL energy provides further separation between signal and background. Furthermore, the larger energy of the Bhabha electrons results in higher energy depositions in both calorimeters if the electron is not absorbed in the ECAL.

[10] A detailed description of the electron signature is given in section 6.1.1.

This leads to rejection criteria against tracks in the tagging hemisphere pointing to cracks between ECAL crystals:

- There is one loose electron and
- $E^{cone}_{ECAL} > 10$ GeV or $P_{CTS} > 10$ GeV and
- non-zero HCAL energy and
- $E^{cone}_{ECAL} + E^{cone}_{HCAL} > 20$ GeV.

In addition, dedicated correlated cuts on acoplanarity are applied, listed in table 5.1.

Hemisphere tagging	Correlated cut	Reject
loose electron and $E^{cone}_{ECAL} > 10$ GeV or $P_{CTS} > 10$ GeV and		
track pointing to ECAL crack	acoplanarity < 0.005 rad	yes
or		
no HCAL energy	acoplanarity < 0.005 rad	yes
or		
non-zero HCAL energy and $E^{cone}_{ECAL} + E^{cone}_{HCAL} > 20$ GeV	acoplanarity < 0.005 rad	yes

Tab. 5.1: The dedicated correlated cuts on acoplanarity to suppress Bhabha events with low ECAL bump energy in the tagging hemisphere.

Figure 5.8 depicts the advantage of dedicated correlated cuts for the selection. The requirements for a loose electron define a sample where the background is enriched relative to the signal, and the rejection criteria reduce mostly the background.

5.2.5 Background from $e^+e^- \to \mu^+\mu^-$

The momentum of muons from $e^+e^- \to \mu^+\mu^-$ peaks around 45 GeV. For triplets the measured peak is very sharp. However, it is broadened for muons measured as doublets because of the lower momentum resolution. Furthermore, a tail down to small momenta comes from radiative muons.

Figure 5.9 shows the energy distribution in the tagging hemisphere for muons measured as triplets. The higher energetic part of the spectrum is dominated by the dimuon

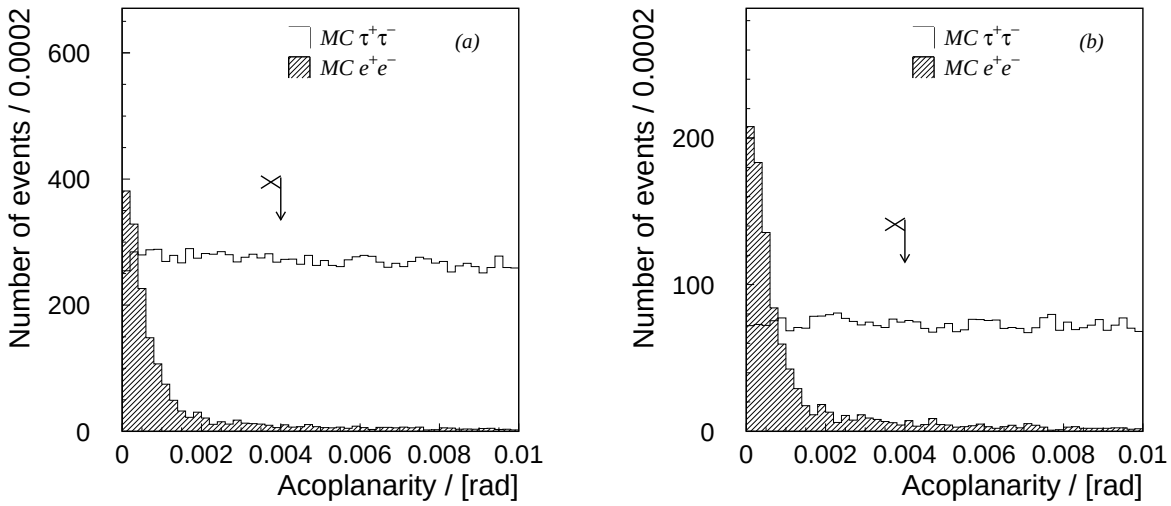

Fig. 5.8: Distribution of the acoplanarity for the signal and the Bhabha background, after the preselection and, in addition, the cuts against high ECAL energies. The right graph (b) gives the acoplanarity for events fulfilling the requirements for a loose electron. The number of signal events in the lost region is considerably smaller for these events. To demonstrate the effect only the Monte Carlo distributions are shown.

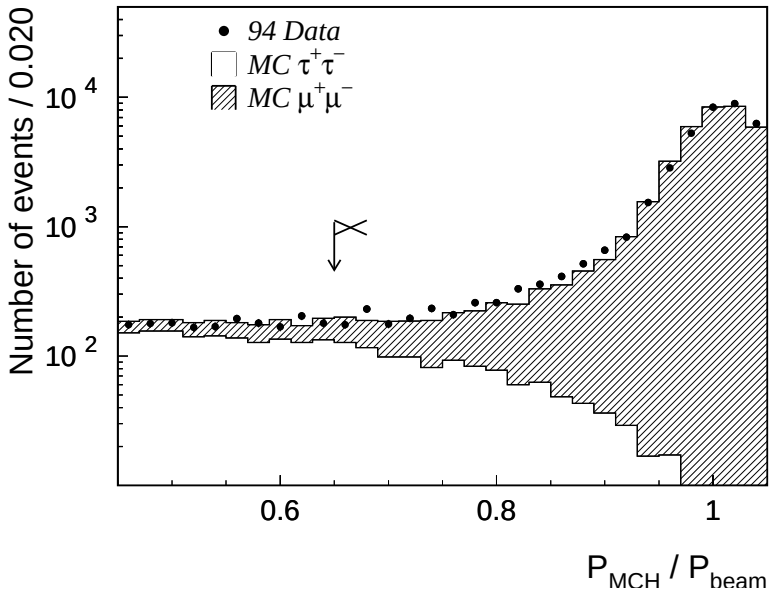

Fig. 5.9: The momentum for events measured as triplets in the muon chambers, after the preselection. The arrow gives the nominal cut value.

events, the lower part by the signal. Triplets are rejected if their momentum exceeds 0.65 P_{beam}. This reduces most of the background from dimuon events. For the muons measured as doublets this cut is reduced to 0.44 P_{beam} (figure 5.10).

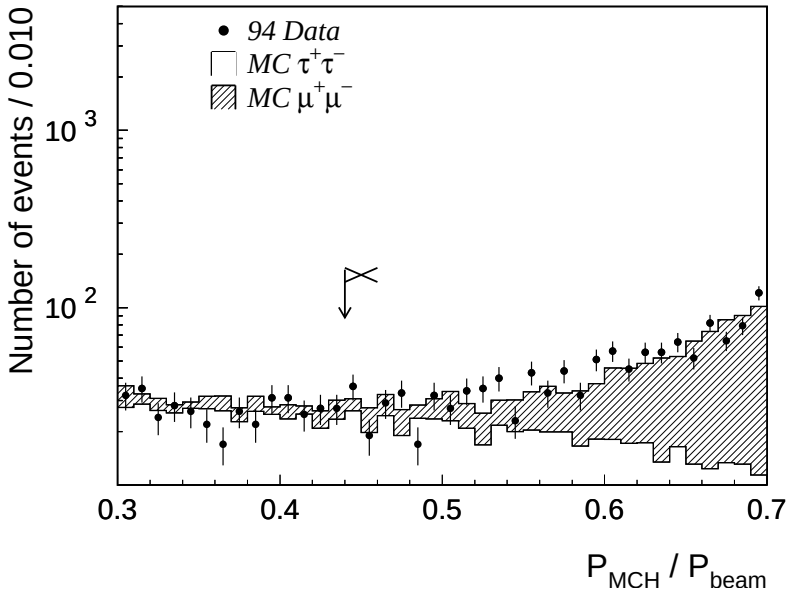

Fig. 5.10: The momentum for events measured as doublets in the muon chambers, after the preselection. The arrow gives the nominal cut value.

For events with at least one P-chamber layer hit in the tagging hemisphere the sum of the calorimetrical energy and the momentum from the muon chamber measured in this hemisphere must not exceed 0.8 P_{beam}. The remaining background from $Z \rightarrow \mu^+\mu^-$ is characterised by a bad or not measured track in the muon spectrometer, or the momenta are low due to photon radiation. These muons tend to have higher momenta than tracks of τ decay products. Thus, requiring a MIP signature together with a minimum momentum selects a sample, where the $Z \rightarrow \mu^+\mu^-$ background is enhanced compared to signal. Applying the rejection criteria on the acoplanarity to this sample reduces mostly background. The dedicated correlated cuts to reject the remaining $Z \rightarrow \mu^+\mu^-$ events are given in table 5.2.

Tracks, where the extrapolation from the CTS points into the central gap in the muon spectrometer at $|\cos\theta| < 0.04$ or between two muon chamber segments in the r-ϕ plane, are rejected, if they fulfil the following requirements:

- $P_{CTS} < 10$ GeV and

Hemisphere tagging	Correlated cut	Reject
one track with $P_{CTS} > 15$ GeV ($E^{cone}_{ECAL} < 5$ or signal in muon chamber) ($E_{HCAL} - E^{MIP}_{HCAL} < 1$ GeV or $E^{9}_{ECAL} < 1$ GeV)	acoplanarity < 0.005 rad	yes
track pointing to muon chamber cracks $E_{HCAL} - E^{MIP}_{HCAL} < 2$ GeV not more than 35 hits in HCAL not more than 3 ECAL bumps [$E^{9}_{ECAL} < 0.5$ GeV or ($E^{cone}_{ECAL} + E^{cone}_{HCAL} < 15$ GeV and $E^{9}_{ECAL} / E^{25}_{ECAL} > 0.94$)]	acoplanarity < 0.005 rad	yes

Tab. 5.2: The dedicated correlated cuts against dimuon events. Requirements to muons in the tagging hemisphere to select large momenta or muons going into muon chamber cracks are combined with a cut on acoplanarity.

- $E^{cone}_{ECAL} + E^{cone}_{HCAL} < 5$ GeV and
- not more than 35 hits in the HCAL and
- $E^{9}_{ECAL} < 0.5$ GeV and
- $E^{9}_{ECAL} / E^{25}_{ECAL} > 0.94$ and
- $E_{HCAL} - E^{MIP}_{HCAL} < 2$ GeV.

The justification for the last five cuts defining the MIP signature is explained in detail in section 6.1.2.

5.2.6 Background from Two-Photon Interactions

For the background from two-photon interactions the cuts are optimised to suppress each of the final states e^+e^-, $\mu^+\mu^-$ and $q\bar{q}$.

Background from $e^+e^- \to e^+e^-\ e^+e^-$

These events are mainly characterised by two low energetic electrons in the detector. The following hemisphere tagging rejects these electrons:

- The ratio E^{cone}_{ECAL} /E^{bump}_{ECAL} is smaller than 1.1 or E^{bump}_{ECAL} is smaller 2 GeV.
- The χ^2_{em} is smaller than 5.
- The probability $P^{comp}_{CTS\text{-}ECAL}$ is larger than 0.01.
- The momentum P_{CTS} is smaller than 6 GeV.
- The E^{bump}_{ECAL} is larger 0.5 GeV and smaller 6 GeV.

To reduce the influence of these cuts for the signal it is required also:

- There is no signal in the muon detector.
- There are no energy depositions in the HCAL.

Hemisphere tagging	Correlated cut	Reject
$P_{CTS} < 10$ GeV no signal in muon chamber $E^{bump}_{ECAL} < 10$ GeV $E^{cone}_{HCAL} < 3$ GeV	acoplanarity < 0.005 rad	yes

Tab. 5.3: The dedicated correlated cut against $e^+e^- \to e^+e^-\ e^+e^-$ events. The hemisphere cuts to select low energetic electrons are combined with a cut on acoplanarity.

Further suppression is achieved by a dedicated cut on acoplanarity for low momentum electrons as given in table 5.3.

Background from $e^+e^- \to e^+e^-\ \mu^+\mu^-$

The muons from $e^+e^- \to e^+e^-\ \mu^+\mu^-$ are generally low energetic and only a small part of them reaches the muon chambers. The remaining appear as low momentum tracks with a MIP compatible energy deposition in the calorimeters. They are suppressed by rejecting events satisfying the following hemisphere cuts:

- The momentum measured in the muon chambers is smaller than 5 GeV.
- The CTS momentum is smaller than 5 GeV.
- The ECAL energy E^{9}_{ECAL} does not exceed 0.5 GeV.
- There is energy deposition in the HCAL, but $E^{\mathrm{cone}}_{\mathrm{HCAL}}$ does not exceed 4 GeV.

The dedicated correlated cut for low momentum MIP's is given in table 5.4.

Hemisphere tagging	Correlated cut	Reject
low momentum MIP: $E^{cone}_{ECAL} < 1$ GeV and $E^{cone}_{HCAL} < 4$ GeV and CTS momentum < 9 GeV muon chamber momentum < 8 GeV	acoplanarity < 0.005 rad	yes

Tab. 5.4: The dedicated correlated cut against $e^+e^- \to e^+e^- \mu^+\mu^-$ events. The hemisphere cuts to select low energetic muons are combined with a cut on acoplanarity.

In addition these tracks must not point into cracks between the muon chamber segments or into the central gap.

Background from $e^+e^- \to e^+e^- q\bar{q}$

These events are very similar to the leptonic final state two-photon events and most of them are affected by the previously described cuts. The remaining events have typically:

- more than one track,
- no signal in muon chamber,
- $E^{\mathrm{bump}}_{\mathrm{ECAL}} < 3$ GeV,
- $E^{\mathrm{cone}}_{\mathrm{HCAL}} < 3$ GeV,
- $P_{\mathrm{CTS}} < 10$ GeV.

and are removed by according cuts in the tagging hemisphere.

5.2.7 Background from $e^+e^- \to q\bar{q}$

Events from $e^+e^- \to q\bar{q}$ have a high multiplicity and a total energy larger than 60 GeV. To reject them, there should be not more than one track and not more than 3 bumps in the ECAL in the tagging hemisphere, and the total calorimetric energy in the hemisphere should not exceed 25 GeV.

5.3 Summary for the Tau Selection

In the L3 data recorded at the Z peak between 1989 and 1995, 163256 events are selected as τ pairs. In the selection procedure τ events were tagged in one hemisphere by looking for the signature of a τ decay. The tagging procedure selects not only τ leptons but other events with similar final state particles in one hemisphere too. These particles are mainly electrons and muons from Bhabha, dimuon and two-photon events. This remaining background is reduced by correlated cuts to both hemispheres which are applied for certain single hemisphere final states, to retain as much as possible τ events.

This procedure provides an almost clean sample of $\tau\tau$ events with a purity of about 97 percent. Correlated cuts were optimised and combined with hemisphere tagging to to minimise the amount of the $\tau\tau$ events affected by correlated cuts. The overall selection efficiency in the fiducial volume is estimated from Monte Carlo to be about 76 percent.

In order to illustrate the agreement between the data and the Monte Carlo distributions, the selected τ sample is divided into three subsamples and characteristic spectra for the tagged hemisphere are compared. Figure 5.11 shows the ECAL bump energy for *electron-like* tracks in the selected τ sample. The probability that the ECAL shower is of an electromagnetic nature is high and the HCAL energy is small for these events. For *muon-like* τ decays a track is required in the muon chambers and the energy measured in the HCAL should be compatible with a MIP (figure 5.12). The remaining events are mostly τ decays into hadrons. The sum of calorimetrical energies measured in the HCAL and ECAL both is given in figure 5.13.

The data are nicely reproduced by the Monte Carlo simulation and the background is well understood. A detailed explanation of the background measurements follows in section 7.1.1.

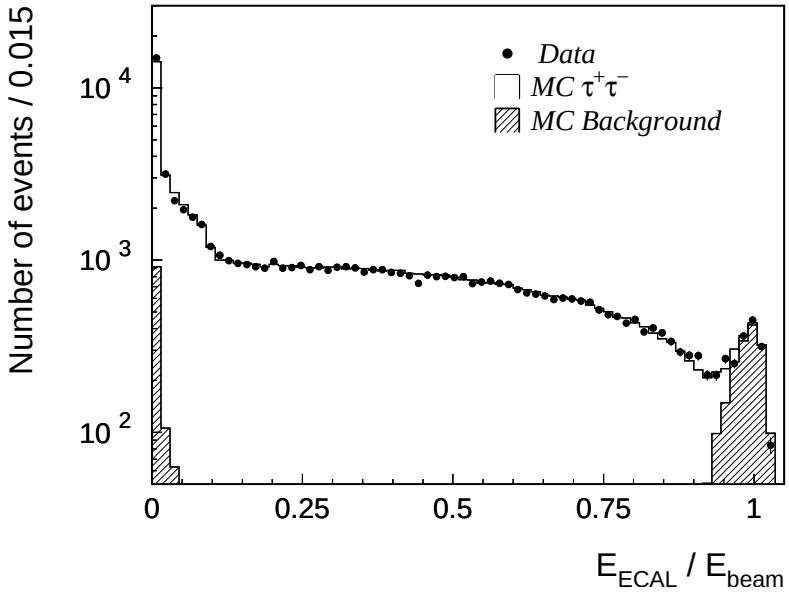

Fig. 5.11: The ECAL bump energy for *electron-like* tracks in the selected τ sample.

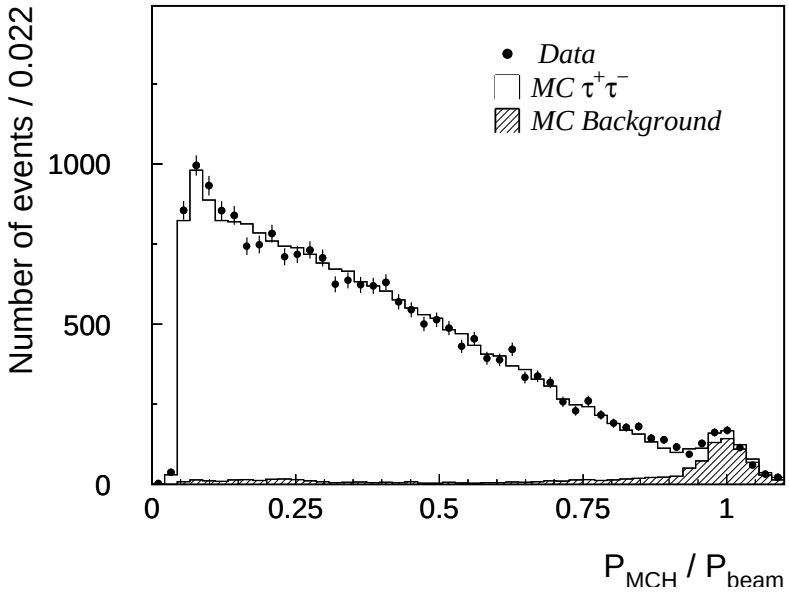

Fig. 5.12: The muon chamber momentum for *muon-like* events selected as τ decays.

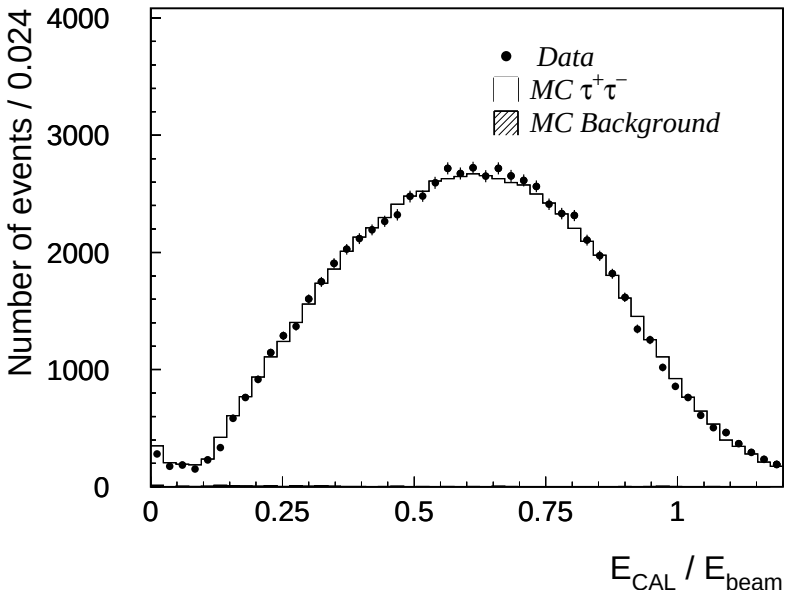

Fig. 5.13: The sum of ECAL and HCAL energies for the part of the τ decays not being *electron-like* or *muon-like*.

Chapter 6

IDENTIFICATION OF LEPTONIC TAU DECAYS

The leptonic τ decays manifest in the detector by a single lepton e, μ in a hemisphere with an energy covering a wide range up to the beam energy. Other τ decay modes can produce electrons and muons in subsequent decays or fake leptons by hadrons. Therefore the identification of leptonic τ decays consists of two parts:

- Identification of a single lepton e, μ.
- Assignment of the lepton to a leptonic τ decay.

The lepton identification is based on the particle identifications for electrons and muons as introduced in chapter 3.2. The identifications are optimised for leptons from τ decays to provide a high identification efficiency over a wide energy range. Additional suppression of hadronic decay modes provides high purity of the final sample of leptonic τ decays.

6.1 Lepton Identification

Single leptons are identified from the combination of their signatures in different subdetecors. Below, typical distributions of measured variables are presented for the electron and the muon.

6.1.1 Electron Identification

The electron identification relies on estimators characterising the electron signature in a quantitative way. These estimators are constructed analysing the electromagnetic shower in the ECAL in combination with the track measurement.

Angular Matching

The good energy resolution and the fine segmentation of the ECAL allow to determine the shower maximum with high precision. The maximum is calculated from the centre-of-gravity of the energy deposited in the 3×3 crystal matrix around the most energetic crystal. For an electron shower the position of the maximum coincides with the impact point of the track. A measure of the matching performance is obtained by comparing the ϕ and θ polar coordinates of the track impact point to the reconstructed shower maximum. Figure 6.1 shows the distribution of the displacement $\phi_{\mathrm{CTS}} - \phi_{\mathrm{ECAL}}$ for high energetic Bhabha events. The achieved resolution of 0.75 mrad is much more precise than the angular coverage of a single crystal in ϕ of about 40 mrad.

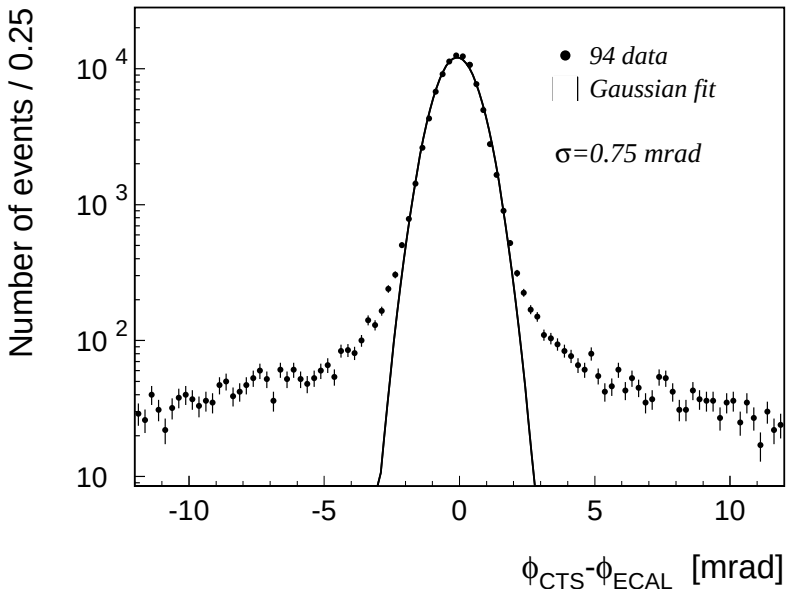

Fig. 6.1: Displacement in ϕ between the extrapolation of the CTS track to the ECAL surface and the shower maximum in the ECAL for Bhabha events, selected from data.

The resolution of $\phi_{\mathrm{CTS}} - \phi_{\mathrm{ECAL}}$ decreases with lower energies following the behaviour of the ECAL energy resolution. Nevertheless, the space matching for electrons is better than for tracks from the other τ decay, mainly hadrons. This is illustrated in figure 6.2.

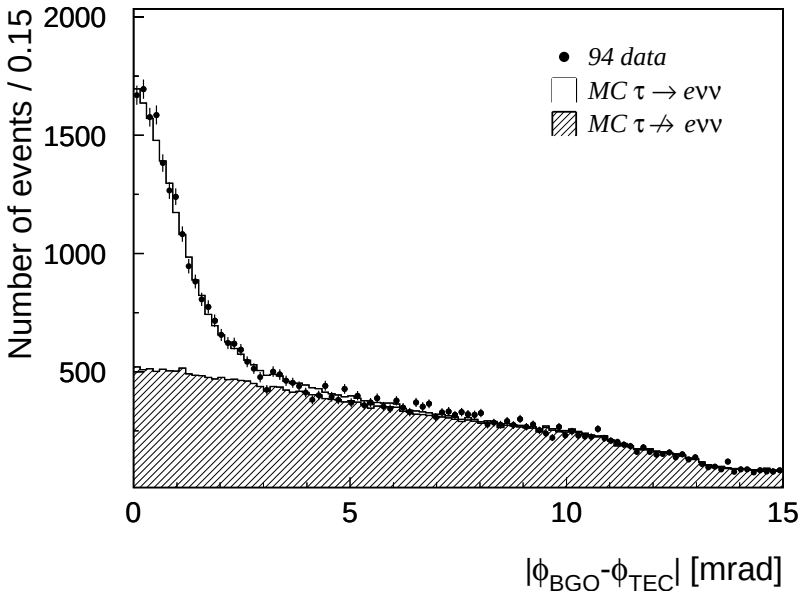

Fig. 6.2: Distance between the shower maximum in the ECAL and the track entry extrapolated from the CTS in ϕ, for the τ sample. The unhashed histogram shows the distribution for the electrons from $\tau \to e\bar{\nu}\nu$.

Electromagnetic Shower Profiles in the ECAL

The regular and fine-grained structure of the ECAL provides electromagnetic showers with a characteristic transverse profile, which is almost independent from the particle energy. The dominant part of the shower is restricted to a 3×3 crystal matrix surrounding the shower maximum. Comparing the summed energy in these 9 crystals E^9_{ECAL} with the sum over 25 crystals (5×5 matrix) E^{25}_{ECAL} gives a ratio of about 0.96 for E^9_{ECAL} /E^{25}_{ECAL} as estimated from a Bhabha data sample and shown in figure 6.3.

The form of the transverse profile is known from test beam studies with electrons. Its parameterisation allows to compute the expected energy for each crystal in the 3×3 crystal matrix taking into account the dependence on the impact point. The variable χ^2_{em} quantifies the compatibility of the observed shower profile with that expected from an electromagnetic one.

The distributions of E^9_{ECAL} /E^{25}_{ECAL} and χ^2_{em} for the τ sample are shown in figures 6.4 and 6.5. Both are useful to discriminate electrons from other τ decay products.

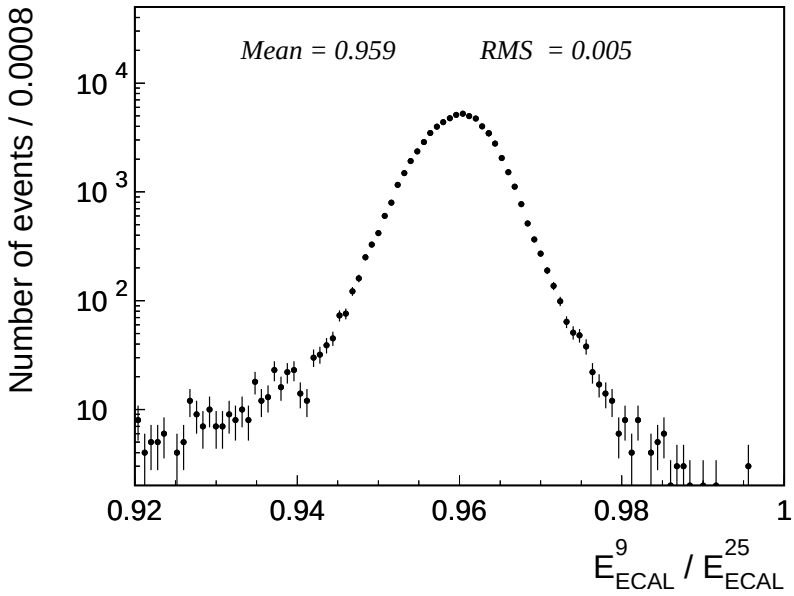

Fig. 6.3: Ratio of the summed ECAL energy in 9 crystals over the sum in 25 crystals around the shower maximum for a Bhabha sample, selected from data.

Additional Estimators for Electrons

Since electrons deposit all their energy in the ECAL, the energy measurement should agree with the momentum provided by the CTS. The probability that both measurements are compatible considering the different resolutions is given by $P^{comp}_{\text{CTS-ECAL}}$.

Furthermore the following estimators are used in this analysis:

- The number of tracks in the hemisphere. It is one for electrons from τ decays.
- The number of ECAL crystals in an electromagnetic shower. The electromagnetic shower profile covers usually more than one crystal.
- The number of reconstructed bumps in the ECAL. Usually an electron consists of one bump only. Additional bumps can arise from radiated photons or due to badly reconstructed showers.
- The energy deposition in the HCAL must be consistent with the tail of an electromagnetic longitudinal shower profile. It is small and restricted to the first three HCAL layers.

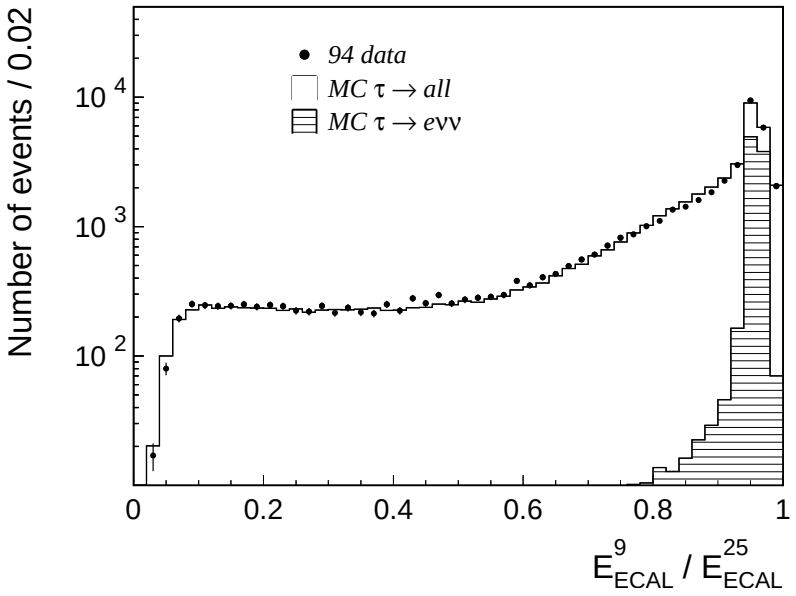

Fig. 6.4: Ratio of the summed ECAL energy in 9 crystals over the sum in 25 crystals around the shower maximum, for the τ sample.

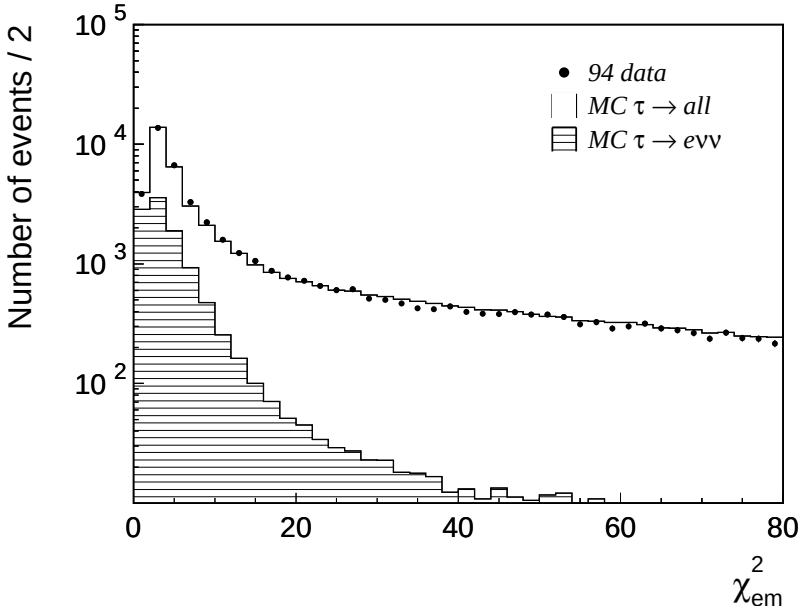

Fig. 6.5: $\chi^2_{\rm em}$ that the ECAL shower is of an electromagnetic nature, for the τ sample.

- The energy deposition in the ECAL outside of the bump which is assigned to the electron. This is quantified by the ratio of the ECAL energies E^{cone}_{ECAL} /E^{bump}_{ECAL}.

6.1.2 Muon Identification

Estimators describing the muon signature can be derived from the track measurement in the muon spectrometer and the MIP response in the calorimeters.

The arrangement of the subdetectors in L3 ensures that hadrons, electrons and photons can not reach the muon spectrometer. Therefore a track in the muon chamber is a strong indication for a muon. But hadrons can produce tracks in the spectrometer too, mostly by decaying into a muon before reaching the HCAL or the by the decay of a hadron of the HCAL shower.

Muon Tracks

For muons from a τ decay the track in the muon spectrometer must point to the interaction region and match with the track in the CTS.

Figure 6.6 gives the distance $\phi_{CTS} - \phi_{MCH}$ between a CTS track and a track in the muon spectrometer in the r-ϕ plane. The tendency of the hadron induced muon chamber tracks to show larger distances corresponds to the fact that the tracks in CTS and muon spectrometer mostly belong to different particles.

The precise track reconstruction in the muon chambers allows to decide if a track comes from the interaction region by calculating the distance of closest approach to the interaction vertex. This distance DCA_{MCH} is less than 500 mm in the r-ϕ and r-z planes for low energy muons and decreases with growing momenta, following the spectrometer resolution.

Minimum-Ionising Signature

The minimum-ionising nature of a muon leads to a characteristic signature in the calorimeters.

A MIP response in the ECAL is characterised by a small shower covering only a few crystals[1]. Therefore the ratio E^{9}_{ECAL} /E^{25}_{ECAL} is close to 1. The typical energy of a muon measured in the ECAL is smaller than 1 GeV (figure 6.7). Due to photon radiation

[1] For about 90 percent of the muons a cluster consists only of utmost 3 crystals.

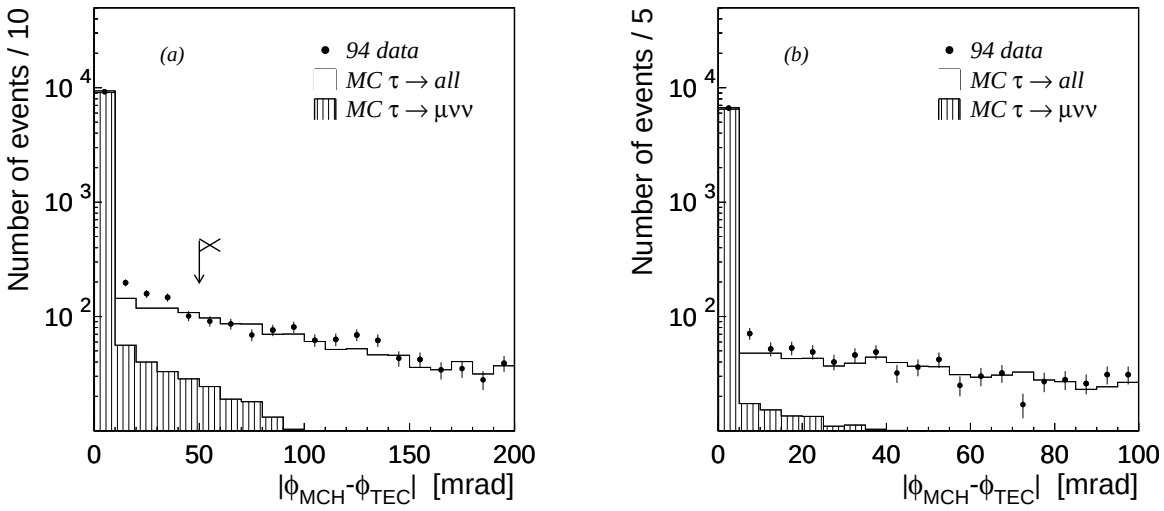

Fig. 6.6: Distance between a CTS track and a track in the muon spectrometer in r-ϕ plane at the interaction vertex. Figure (a) gives the distribution for the whole τ sample. In figure (b) tracks passing the CTS close to the anode wires, where the CTS measurement is poor, are suppressed.

larger ECAL energies occur in some cases. Nevertheless, a good separation between $\tau \to \mu\bar{\nu}\nu$ events and other τ decays is still achieved (figure 6.8).

The energy depositions of a muon interacting in the HCAL are small and distributed along its line of flight. They are predictable from the measured muon track. The compatibility of the energy depositions in the hadron calorimeter with that expected from a muon is quantified in the following way. The measured energy deposits in the HCAL lying along a straight line are fitted with the expectation for minimum-ionising particles and a χ^2_{MIP} is calculated. The comparison of the expected signal with the measured one provides further estimators for the minimum-ionising signature in the HCAL like the difference between the measured and expected energy, $\mathrm{E_{HCAL}} - \mathrm{E^{MIP}_{HCAL}}$ (figure 6.9).

The MIP signature of muons in both calorimeters illustrates figure 6.10. It shows the calorimetric energies for 45 GeV muons for $\mathrm{Z} \to \mu^+\mu^-$ events selected from data. The measured energy depositions are only a small part of the muon energy. The dependence of the calorimetrical energy on the particle's momentum is shown in figure 6.11. For muons from $\tau \to \mu\bar{\nu}\nu$ the energy deposition is small and independent from the muon momentum whereas for other τ decays the measured muon momentum is small and the calorimetrical energy larger than for a MIP.

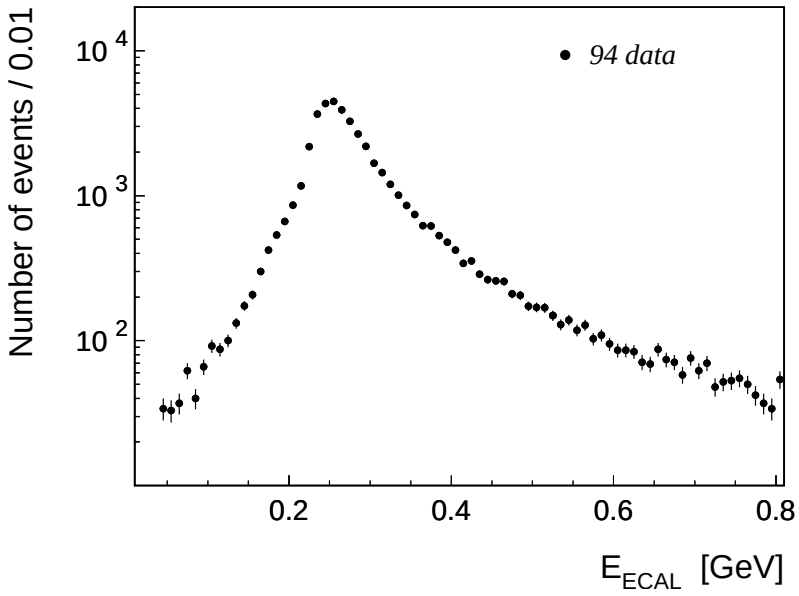

Fig. 6.7: The energy deposition in the ECAL for Z $\rightarrow \mu^+\mu^-$ events selected from data.

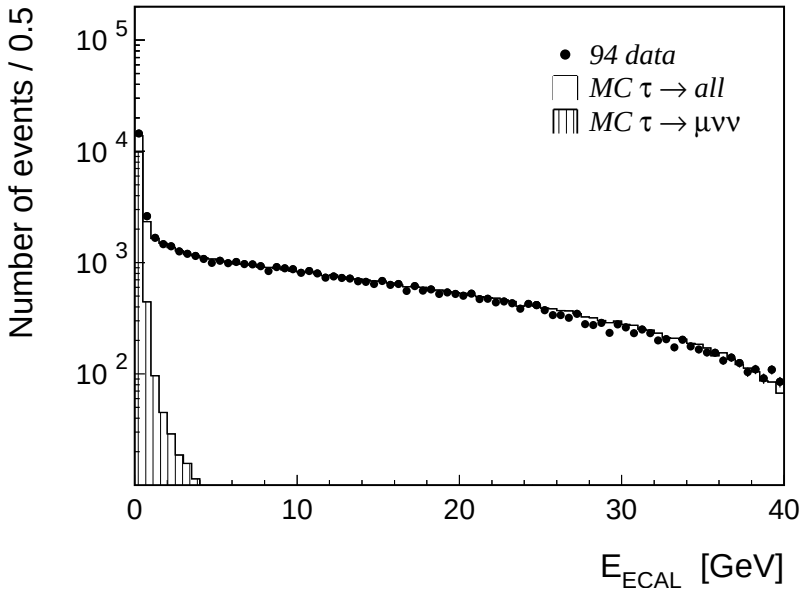

Fig. 6.8: The energy deposition in the ECAL for all τ decays and for τ decays into muon. A track in the muon spectrometer is required.

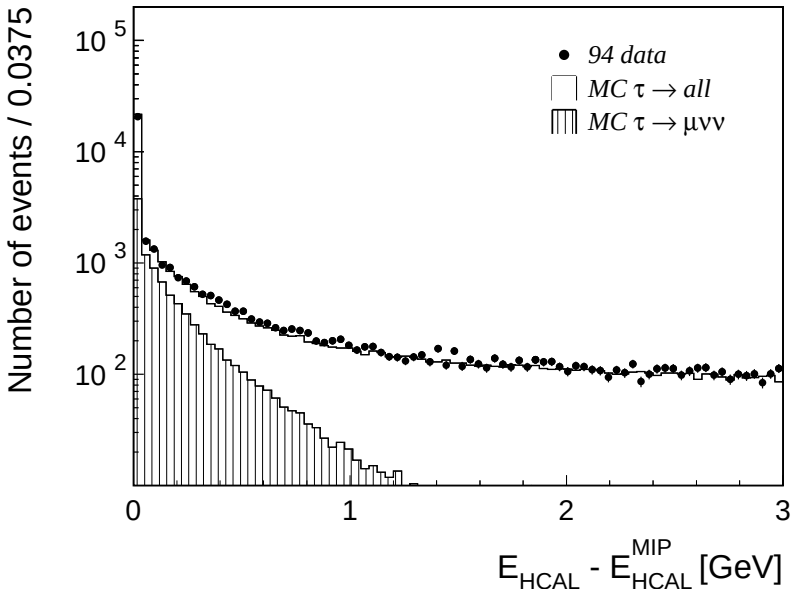

Fig. 6.9: The distribution for the difference between between the measured HCAL energy and the energy expected for MIP, for the τ sample.

6.2 Identification of Leptonic Tau Decays

The identification of leptonic τ decays is performed as an identification of single leptons based on the estimators discussed in the above sections. Additionally, requirements to reject decay products from other τ decays are developed.

6.2.1 Identification of $\tau \to e\bar{\nu}\nu$

A common identification of $\tau \to e\bar{\nu}\nu$ is to accept "good" electrons only. Tight cuts are applied, for values of the estimator variables, where the probability for electrons is strongly enhanced. This ensures high purity and acceptable efficiencies but makes the identification, especially the identification efficiency, very sensitive to the quality of the measurement of "bad" electrons caused by detector effects or accompanying photons. To reduce that sensitivity $\tau \to e\bar{\nu}\nu$ decays are identified as follows:

1. An *electron candidate* is defined using loose cuts and by setting requirements on combinations of estimators which must be met independently.

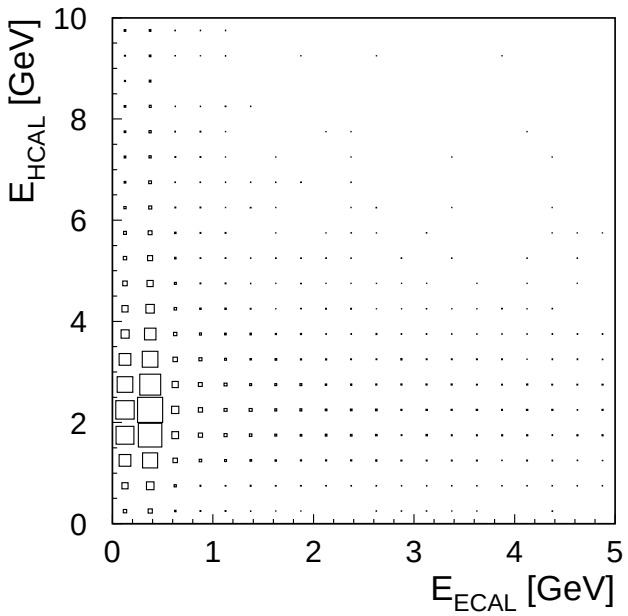

Fig. 6.10: The energy depositions of muons from Z $\rightarrow \mu^+\mu^-$ data events in the calorimeters.

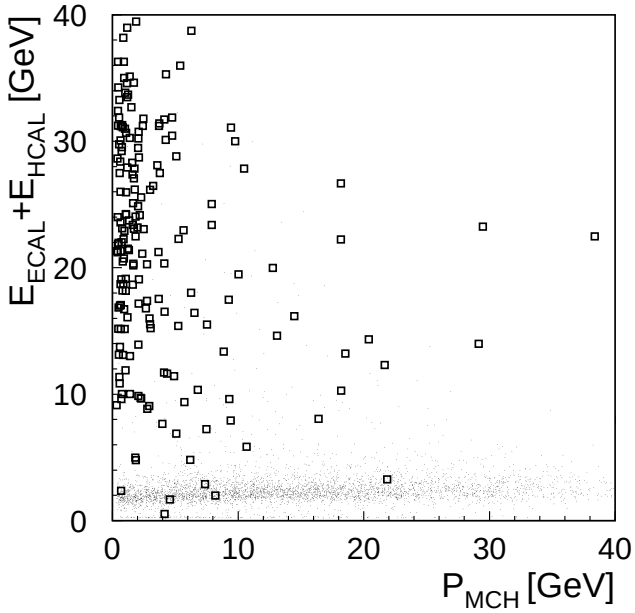

Fig. 6.11: The total calorimetrical energy is shown against the momentum measured in the muon spectrometer for the τ Monte Carlo sample. The small dots are for muons from τ decays. Rectangles are tracks in the muon chambers originating from hadronic τ decays.

2. Veto cuts are applied to suppress remaining muons and hadrons. These cuts combine additional criteria typical for the background signature with electron identification estimators.

Electron candidates have to satisfy the following criteria in the tagged hemisphere:

1. There is one track.
2. The track is inside $|\cos\theta| < 0.71$.
3. The electromagnetic shower consists of at least 4 ECAL crystals.
4. There are not more than 4 bumps in the ECAL.
5. The probability $\mathrm{P}^{comp}_{\text{CTS-ECAL}}$ is larger than 5×10^{-6}.
6. There is no response from the muon chamber and muon filter.
7. - The ratio $\mathrm{E}^{\text{cone}}_{\text{ECAL}}$ /$\mathrm{E}^{\text{bump}}_{\text{ECAL}}$ is smaller than 1.1 or
   - χ^2_{em} is smaller than 30 or
   - $\mathrm{E}^{9}_{\text{ECAL}}$ /$\mathrm{E}^{25}_{\text{ECAL}}$ is larger than 0.92.

This selects 94 percent of the electrons but the amount of misidentified hadrons and muons is still about 40 percent. These events from other τ decays are suppressed as described in the following.

Figure 6.12 gives the distribution of $\mathrm{P}^{comp}_{\text{CTS-ECAL}}$ for the electron candidates. For most of the background the CTS momentum is different from the measured ECAL energy because they are not absorbed in the ECAL. The small amount of electrons where momentum and ECAL energy disagree is caused by bad momentum measurement for particles passing the CTS close to the anode wires mainly. For those events also the angular matching between the CTS track and the ECAL shower maximum is worse and can be as bad as it is typical for the background. In order to reduce the background but to keep the poor measured electrons the cut on $\mathrm{P}^{comp}_{\text{CTS-ECAL}}$ is combined with requirements for the shower in ECAL.

A bad agreement between the CTS and the ECAL measurements is given for electron candidates if:

- $\mathrm{P}^{comp}_{\text{CTS-ECAL}} < 0.03$ or
- $|\theta_{\text{CTS}} - \theta_{\text{ECAL}}| > 12$ mrad or

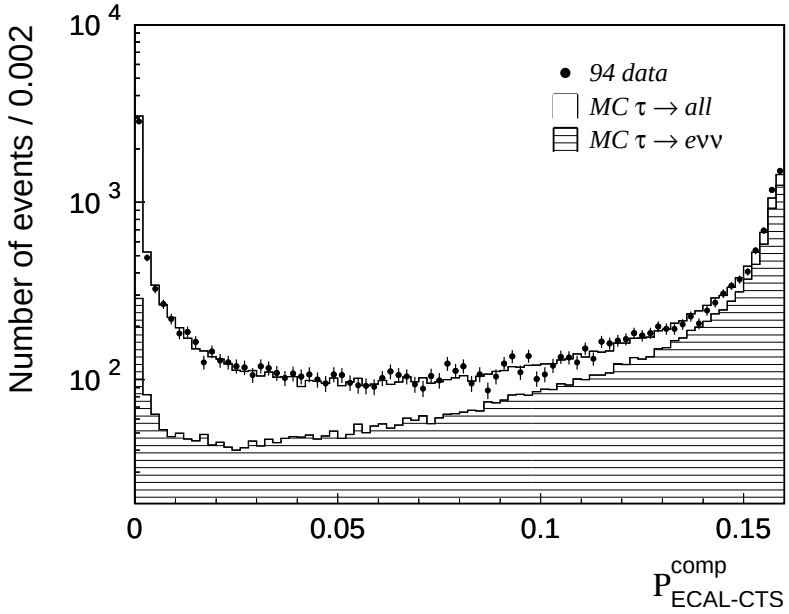

Fig. 6.12: Probability that CTS momentum and ECAL energy are compatible, for the τ sample. The hatched histogram shows the distribution for $\tau \to e\bar{\nu}\nu$.

- $|\phi_{\mathrm{CTS}} - \phi_{\mathrm{ECAL}}| > 3$ to 11 mrad[2].

To retain the electrons these events must fulfil the following cuts

- not more than 2 bumps in the ECAL[3],
- $0.92 < \mathrm{E}^{9}_{\mathrm{ECAL}} / \mathrm{E}^{25}_{\mathrm{ECAL}} < 0.98$,
- $\chi^2_{\mathrm{em}} < 20$.

Otherwise the electron candidate is rejected.

Only a few percent of the electrons produce an energy deposition in the HCAL, either if they do not shower in the ECAL or if the shower leaks into the hadron calorimeter. This happens preferred if a track goes to the edges of the ECAL crystals. These electrons are distinguished from other τ decay products by suppressing electron candidates with non-zero HCAL energy and:

[2] The actual value of the cut on $|\phi_{\mathrm{CTS}} - \phi_{\mathrm{ECAL}}|$ depends on shower energy and varies from 11 mrad at 1 GeV to about 3 mrad at 45 GeV.

[3] More than two bumps are, e.g., typical for hadronic τ decays with π^0decaying into photons.

- at least one additional ECAL bump or
- $\chi^2_{\rm em} > 20$.

If the extrapolation of the track hits the central region of a crystal, defined in the r-ϕ plane[4], the cluster in the HCAL must be consistent with a tail of an electromagnetic shower.

A low ratio of $\mathrm{E}^9_{\rm ECAL}$ /$\mathrm{E}^{25}_{\rm ECAL}$ is typical for electrons accompanied by photons nearby but for hadrons from τ decays too. In order to suppress these hadrons there should be no additional ECAL bump and $\chi^2_{\rm em} < 20$ for events with $\mathrm{E}^9_{\rm ECAL}$ /$\mathrm{E}^{25}_{\rm ECAL} < 0.92$.

6.2.2 Identification of $\tau \to \mu\bar{\nu}\nu$

The identification of $\tau \to \mu\bar{\nu}\nu$ is based on a signal in the muon spectrometer. This implies the restriction to muons with a momentum larger than 2.5 GeV, the average energy loss in the calorimeters. However, it ensures a good understanding of the remaining background. The background is suppressed by requiring a MIP signature in the calorimeters and the muon originating in the interaction region.

A *muon candidate* is defined as one track in the central tracking system and a track in the muon spectrometer in the tagged hemisphere. The muon track must contain at least two P-segments. This selects 82 percent of the muons from $\tau \to \mu\bar{\nu}\nu$ with an fraction from other τ decay modes of 12 percent.

A muon candidate is suppressed as background, if it fulfils one of the following conditions:

- The energy of a ECAL shower matched by a track, $\mathrm{E}^9_{\rm ECAL}$, is greater than 1 GeV and $\mathrm{E}^9_{\rm ECAL}$ /$\mathrm{E}^{25}_{\rm ECAL}$ is smaller than 0.94.
- The muon spectrometer track does not match with a CTS track or the muon track does not extrapolate into the interaction region:

  $|\phi_{\rm CTS} - \phi_{\rm MCH}| > 0.05$ (remember figure 6.6) or

  $DCA^{MCH}_{r\text{-}\phi} > 70$ to 500 mm, depending on the muon momentum or

  $DCA^{MCH}_{r\text{-}z} > 500$ mm.

[4] A local ϕ from 0 to 1 is defined for each crystal. The local ϕ of the impact point is between 0.05 and 0.95.

There is no MIP signature in a calorimeter:

$$E^{9}_{ECAL} > 0.4 \text{ GeV} \quad \text{or}$$
$$E^{9}_{ECAL} / E^{25}_{ECAL} < 0.94 \quad \text{or}$$
$$E_{HCAL} - E^{MIP}_{HCAL} > 0.2$$

- The sum of calorimetrical energy matched by a track is larger than 5 GeV and the deposits in the HCAL are inconsistent with a muon signature:

$$\chi^2_{MIP} > 50 \text{ and}$$
$$E^{cone}_{ECAL} < 4 \text{ and } E^{3 \text{ layers}}_{HCAL} > 1 \quad \text{or}$$
$$E^{cone}_{ECAL} > 4 \text{ and } E_{HCAL} - E^{MIP}_{HCAL} > 0.2$$

The cut on the HCAL energy in the first three layers as seen from the interaction region, $E^{3 \text{ layers}}_{HCAL}$, is used to discriminate low energetic hadrons, which will leave most of their energy in the shower at the beginning of the HCAL.

Chapter 7

THE MEASUREMENT

The τ leptonic branching fractions with their statistical errors are measured from the data samples provided by the τ selection and the lepton identification, including corrections for efficiency and background contributions as well. The measurement is checked for the influence of systematic effects and according errors are assigned.

The τ selection is done for each year separately because the detector performance and hence the realistic Monte Carlo simulation differ from year to year. The subsequent background estimations as well as the identification of leptonic τ decays is performed for these subsamples.

7.1 Background Measurements

7.1.1 Background Measurements for the Tau Sample

The background in the selected τ samples amounts to about 3%, and must be known with a relative precision of 10% or better to give a systematic error well below the expected statistical precision of the measurements. The background usually comes from tails of distributions, which are sometimes not well described in the Monte Carlo simulation. Hence the background contributions calculated from the Monte Carlo simulation by normalising the generated number of events to the rate expected from the measured luminosity are checked carefully and are corrected for observed discrepancies.

Background from $e^+e^- \to e^+e^-$

The energy distribution for low energetic or badly measured Bhabha electrons has been found to be badly reproduced in the simulation. Therefore the number of remaining Bhabha events is estimated from the data. The ECAL energy spectrum of the data

in the tagged hemisphere is fitted by a superposition of the Monte Carlo predictions for $\tau\tau$ and Bhabha events in an energy region where the background is dominant (see figure 7.1).

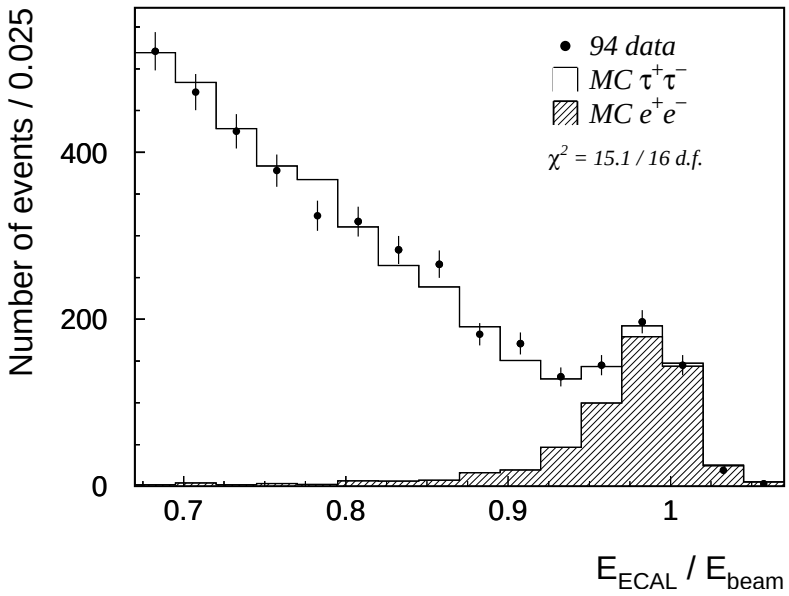

Fig. 7.1: The ECAL energy in the tagged hemisphere used for the estimation of the Bhabha background fraction. The energy spectrum of the data is fitted by a superposition of the Monte Carlo predictions for $\tau\tau$ and Bhabha events.

The fit provides a scale factor which is used to calculate the background contribution from the number of Monte Carlo Bhabha events passing the τ selection. The error of the contribution is taken from the error of the fit.

Background from $e^+e^- \to \mu^+\mu^-$

The background from $e^+e^- \to \mu^+\mu^-$ are mainly events where the muon in the tagging hemisphere is badly measured in the muon chambers. To rely not completely on the description of such effects in the Monte Carlo simulation the background is measured by a fit to the data. The energy spectrum of the muons in the τ data sample is reproduced by a superposition of the Monte Carlo predictions for the signal and the background. This is performed for a sample of muons with a momentum measured in the muon chamber of more than half of the beam energy. Figure 7.2 shows the result of the fit.

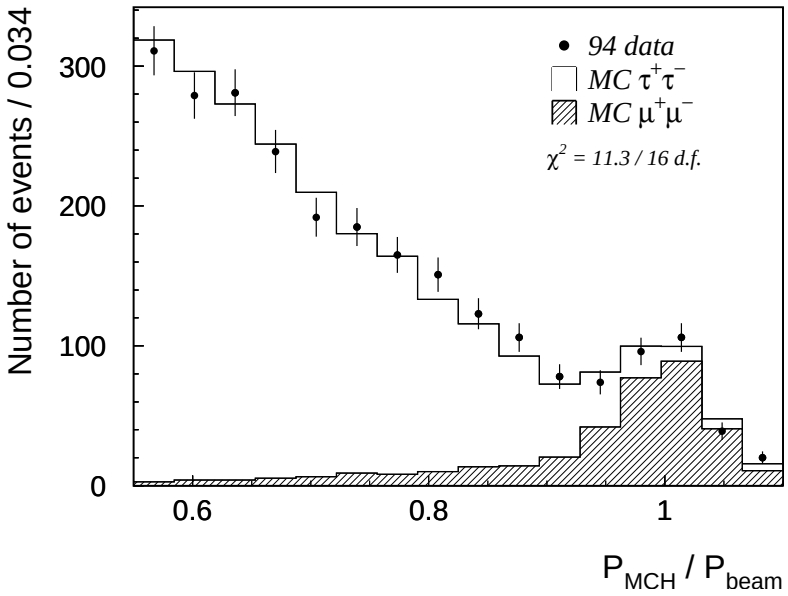

Fig. 7.2: The momentum spectrum for events measured in the muon chambers. The plot shows the data distribution for the final τ sample and the Monte Carlo prediction. A fit is performed to estimate the fraction of the background.

Background from Two-Photon Interactions

The background from two-photon events is estimated for each of the final states e^+e^-, $\mu^+\mu^-$ and $q\bar{q}$, separately. The contributions are to small to measure them by a fit to the final τ data sample. The background fractions are therefore evaluated from the number of Monte Carlo events remaining after the τ selection. The number of these events is normalised by scaling the Monte Carlo expectations to the luminosity of the data sample.

Background from $e^+e^- \to q\bar{q}$

The background from $e^+e^- \to q\bar{q}$ is evaluated from the data. A clean reference sample of $e^+e^- \to q\bar{q}$ events is selected by the following requirements:

- The total number of ECAL clusters should exceed 12.
- The maximum opening angle between a track and the thrust should be larger than 25 degrees.
- The total calorimetrical energy in both hemispheres should be larger than 50 GeV.

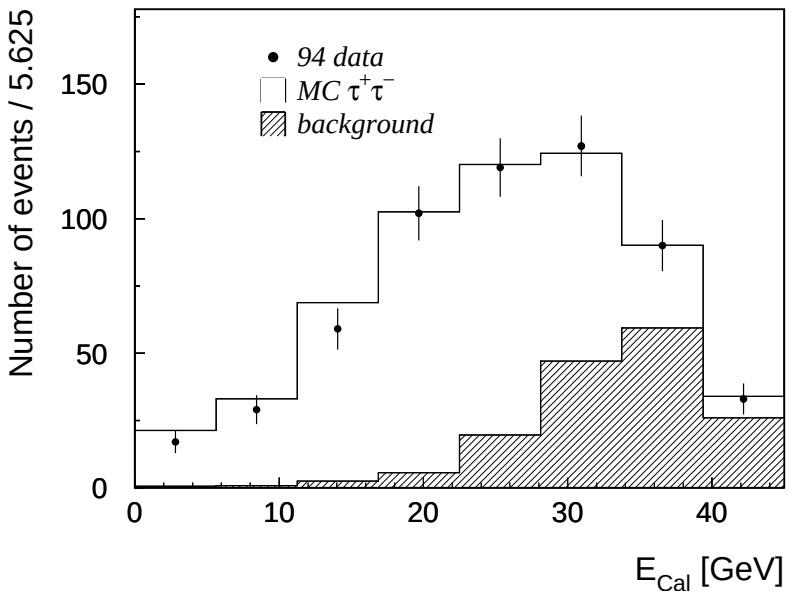

Fig. 7.3: Calorimetric energy spectrum in the tagged hemisphere for events with more than 12 ECAL clusters per event. The plot shows the distribution for the final τ sample. The fraction of the background from $e^+e^- \to q\bar{q}$ is estimated by fitting a reference data sample together with the simulated τ spectra.

From this sample the remaining $e^+e^- \to q\bar{q}$ events in the τ sample were measured by fitting the calorimetrical energy for events with more than 12 ECAL clusters. Figure 7.3 shows the result of the fit. Since the complete reference sample is used, the fit provides the total number of $e^+e^- \to q\bar{q}$ events in the τ sample.

Background from Cosmic Muons

The amount of the remaining cosmic muons is estimated from the data. A clean cosmic muon sample is selected by:

- the band $|(\mathrm{DCA}_1 + \mathrm{DCA}_2)| < 3$ mm and
- $|\mathrm{DCA}_1| + |\mathrm{DCA}_2| > 6$ mm.

The DCA of these events were recalculated to get a sample of cosmic muons with $|\mathrm{DCA}_1| + |\mathrm{DCA}_2| < 3$ mm, corresponding to a sample of cosmic muons passing the detector close to the interaction region. Such muons are not rejected by the cuts on large DCA. Assuming that the density is constant in the band, the remaining cosmic muon background is estimated from these cosmic muons passing the τ selection.

7.1.2 Background Measurements for the Leptonic Samples

The background contaminations for the samples with decays identified as $\tau \to e\bar{\nu}\nu$ and $\tau \to \mu\bar{\nu}\nu$, respectively, are estimated from the simulated background passing the τ selection and the identification of leptonic τ decays. The number of these events is scaled with same factors as the simulated background in the τ sample.

7.2 Identification Efficiencies

The precise knowledge of the efficiency to identify the leptonic τ decays is essential for the measurement of the branching fractions. In contrast to the background fractions which are only a few percent the efficiency is about 80 percent. To keep the systematic error below the statistical one the efficiency should be known with a relative precision of better than one percent. The efficiency can be obtained with sufficient statistical precision from Monte Carlo simulation. But even small deviations between the data and the Monte Carlo simulation could lead to sizeable differences between the real and the determined from simulation identification efficiencies.

The leptonic τ decays are identified through their lepton. The identification is based on the properties of the lepton and almost independent from the production process. Hence it can be studied and compared for data and Monte Carlo simulation using other processes, referred to as control samples. The key condition is that the lepton is tagged independently from the identification considered.

7.2.1 Electron Identification Efficiency

The electron identification efficiency as a function of the reconstructed electron energy is shown for $\tau \to e\bar{\nu}\nu$ decays from Monte Carlo simulation in figure 7.4. The efficiency is over 90 percent over a wide energy range. It decreases slightly towards lower energies. The proper reconstruction of the electron shower is less affected by detector effects like single noisy or dead crystals at higher energies. In addition the energy depositions of electrons and radiated photons can overlap in the electromagnetic calorimeter. This can shift the position of the shower maximum away from the electron track or reduce the ratio E^9_{ECAL} /E^{25}_{ECAL}. These effects from radiated photons are more pronounced if the electron energy is not too large compared to the photon energy.

For very low energetic electrons the identification efficiency drops while the misidentification probability for other τ decays increases. The high end of the spectra is dominated

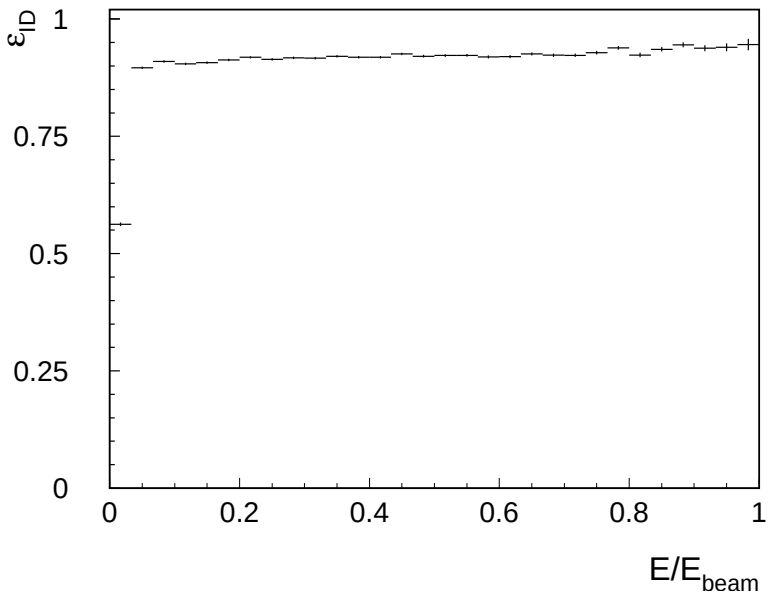

Fig. 7.4: The efficiency for identifying the decay $\tau \to e\bar{\nu}\nu$ is shown for the Monte Carlo simulation as a function of the reconstructed electron energy.

by Bhabha events. To minimise the uncertainties arising from these sources, the final electron spectrum is restricted to $0.015 < E_{electron}/\mathrm{E_{beam}} < 0.85$.

The identification efficiencies for $\tau \to e\bar{\nu}\nu$ decays as estimated from the Monte Carlo simulation are listed in table 7.1. The efficiencies are given for the total Monte Carlo sample selected as τ decays, and inside the accepted geometrical and energetic region.

The electron identification is studied for control samples of Bhabha events and of events from $e^+e^- \to e^+e^-\, e^+e^-$.

The Bhabha events are selected by requiring a high energetic electron of at least 0.95 $\mathrm{E_{beam}}$ in the tagging hemisphere. Figure 7.5 shows the identification efficiency for an electron in the tagged hemisphere.

The comparison of the electron identification in data and Monte Carlo simulation shows a small overestimation of the identification efficiency in the Monte Carlo simulation. This is explained by not perfectly reproduced ECAL effects like leakage, dead crystals and noisy crystals, which influence the reconstruction of electromagnetic showers.

Like for the high energetic electrons an overestimation of the identification efficiency is observed for low energetic electrons from a $e^+e^- \to e^+e^-\, e^+e^-$ control sample as shown in figure 7.6.

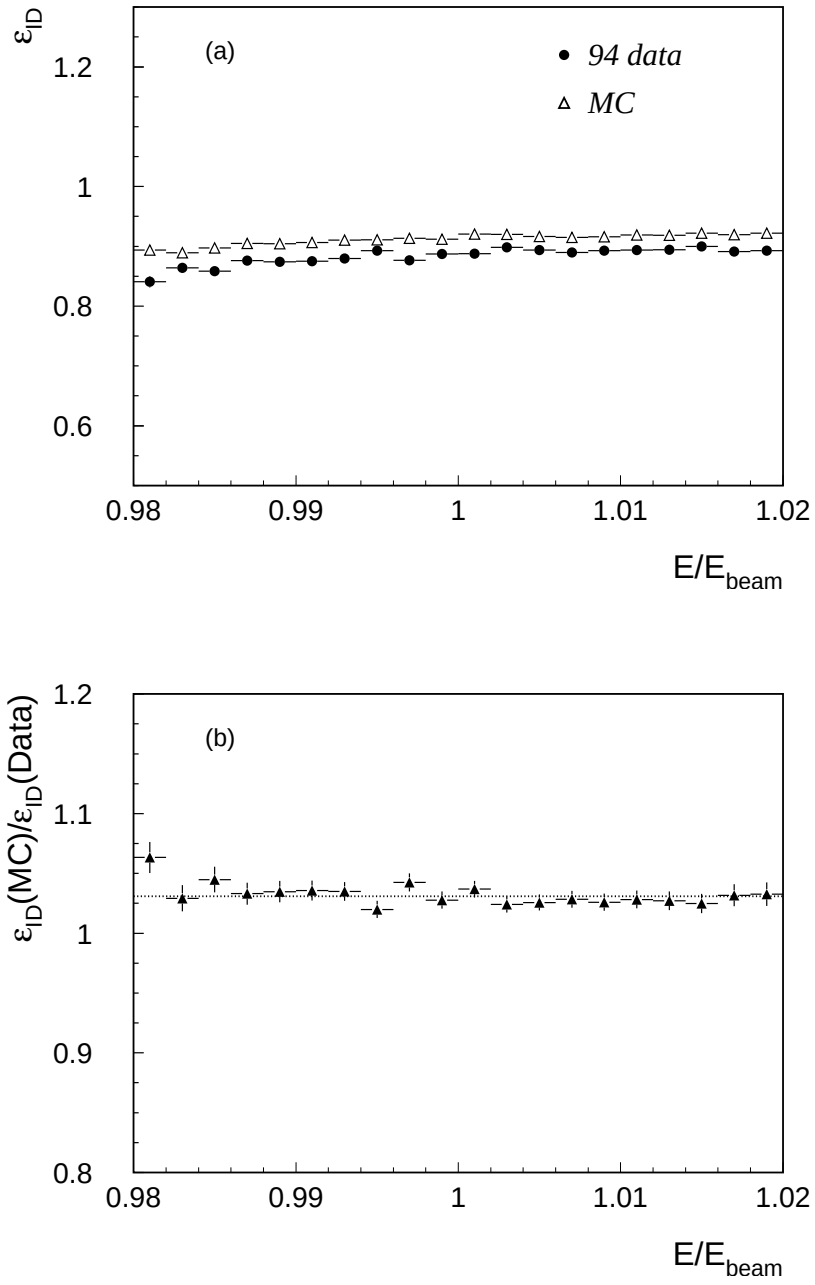

Fig. 7.5: Electron identification for high energetic electrons from Bhabha events . The upper figure shows the identification efficiency for data and Monte Carlo simulation in dependence on the energy measured in the ECAL. The lower graph gives the ratio of both distributions together with the result of a linear fit.

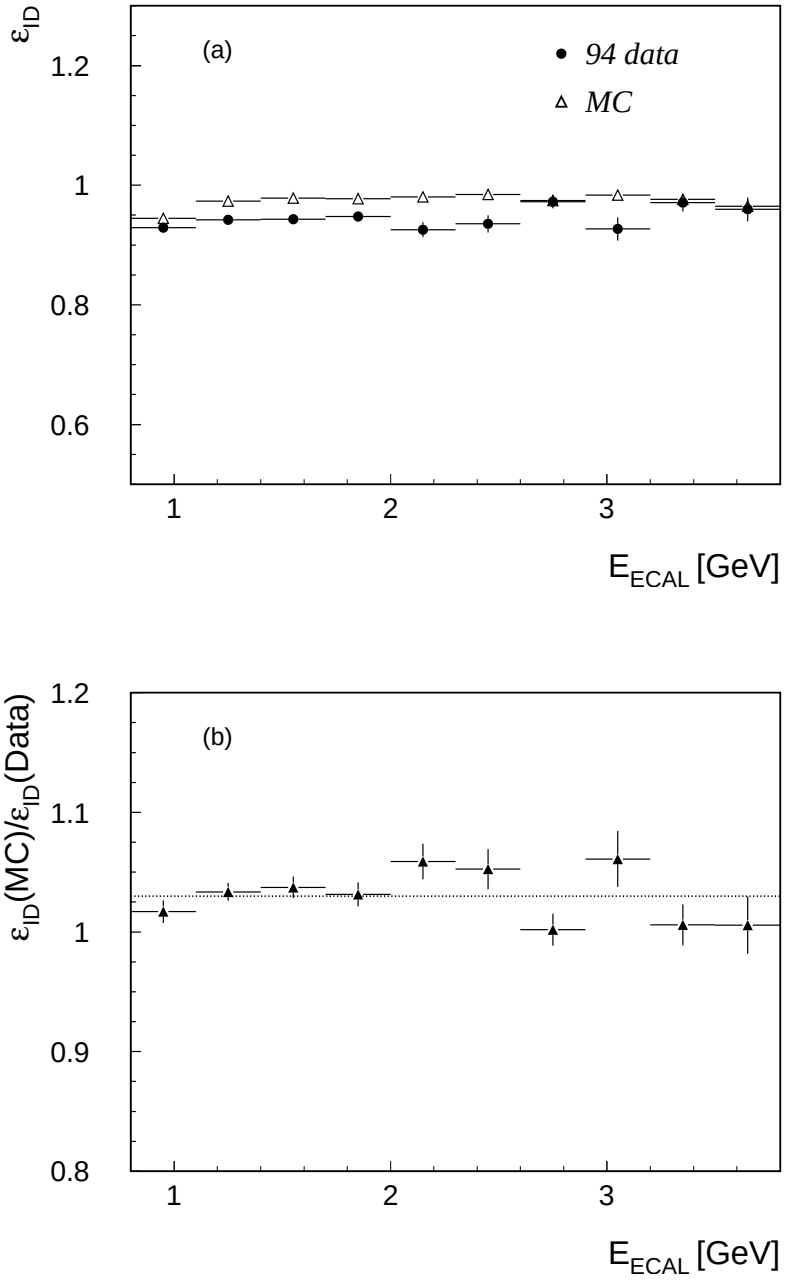

Fig. 7.6: Electron identification for $e^+e^- \to e^+e^-\ e^+e^-$ events. The upper figure shows the identification efficiency for data and Monte Carlo simulation in dependence on the energy measured in the ECAL. The ratio of both distributions together with the result of a linear fit is given in (b).

	Total efficiency (%)	Inside efficiency (%)
1991+92	88.61 ± 0.14	93.14 ± 0.13
1993	86.49 ± 0.16	90.43 ± 0.16
1994	86.56 ± 0.11	90.55 ± 0.11
1995	85.32 ± 0.14	89.23 ± 0.14

Tab. 7.1: The identification efficiencies for $\tau \to e\bar{\nu}\nu$ events with respect to the τ selected Monte Carlo sample. The quoted errors come from the statistics of the sample. The *inside* efficiency corresponds to the accepted geometrical and energetic region.

Both control samples are used separately to determine an efficiency correction

$$c_{ID} = \frac{\varepsilon_{ID}^{MC}}{\varepsilon_{ID}^{data}} \tag{7.1}$$

from the identification efficiencies in data and in Monte Carlo simulation, ε_{ID}^{data} and ε_{ID}^{MC}.

To ensure that the electron identification in the control samples is comparable to that of the electrons from τ decays not the whole control samples are used but only kinematical regions where the identification efficiency is almost constant. But comparing the identification for such kinematical region, e.g. defined by requiring a minimum ECAL energy, provides only the efficiency correction c_{ID}^{ECAL}. This correction does not account possible deviations of the ECAL detector efficiency[1] in data and Monte Carlo simulation, c_{ECAL}^{eff}, which is related to c_{ID} as

$$c_{ID} = c_{ID}^{ECAL} \cdot c_{ECAL}^{eff} \,. \tag{7.2}$$

The same holds for the momentum measured in the CTS:

$$c_{ID} = c_{ID}^{CTS} \cdot c_{CTS}^{eff} \,. \tag{7.3}$$

Both are multiplied to

$${c_{ID}}^2 = c_{CTS}^{ID}\, c_{ECAL}^{ID} \cdot \varepsilon_{CTS}^{eff}\, \varepsilon_{ECAL}^{eff} \,, \tag{7.4}$$

where c_{ID} still depends on the detector efficiencies. An intrinsic estimation of these efficiencies can be achieved by measuring the identification efficiencies for the ECAL

[1] The ECAL detector efficiency gives the fraction of electrons with an ECAL measurement.

energy by requiring a CTS track. This gives the efficiency correction

$$c_{ID} = c^{ID}_{CTS+ECAL} \cdot \varepsilon^{eff}_{CTS}\,\varepsilon^{eff}_{ECAL} \;, \tag{7.5}$$

Replacing $\varepsilon^{eff}_{CTS}\,\varepsilon^{eff}_{ECAL}$ in formula 7.4 with formula 7.5 leads to

$$c_{ID} = \frac{c^{ID}_{CTS}\,c^{ID}_{ECAL}}{c^{ID}_{CTS+ECAL}} \;. \tag{7.6}$$

The identification corrections are estimated from the ECAL energy and CTS momentum distributions for both control samples and using formula 7.6. This provides one correction factor at low electron energies from $e^+e^- \to e^+e^-\,e^+e^-$ and one at high electron energies from Bhabha events. Both corrections are of comparable size. Furthermore, the comparison of the identification efficiency for radiative Bhabha events as shown in figure 7.7 gives no indication for an energy dependence of the deviations in the identification efficiencies.

Table 7.2 shows the efficiency corrections for the electron identification together with the result of a linear fit. The fit is applied to take into account the small differences in the correction factors at low and at high energies. It provides a slope for a possible linear dependency of the correction which is convoluted with the identification efficiency for the Monte Carlo τ sample bin by bin. Then the correction determined at high electron energies is applied to the Monte Carlo identification efficiency.

	$\frac{\varepsilon^{ID}_{MC}}{\varepsilon^{ID}_{Data}}$ at $\frac{E}{E_{beam}} = 0.05$	$\frac{\varepsilon^{ID}_{MC}}{\varepsilon^{ID}_{Data}}$ at $\frac{E}{E_{beam}} = 1$	Slope
1991+92	1.026 ± 0.008	1.034 ± 0.003	0.008 ± 0.009
1993	1.035 ± 0.010	1.034 ± 0.003	-0.001 ± 0.011
1994	1.031 ± 0.005	1.033 ± 0.002	0.001 ± 0.005
1995	1.031 ± 0.006	1.031 ± 0.003	0.000 ± 0.007

Tab. 7.2: Corrections to the electron identification efficiency. Linear fits provide the slopes between the corrections for high electron energies and for low electron energies.

7.2.2 Muon Identification Efficiency

The muon identification efficiency determined from Monte Carlo simulation for $\tau \to \mu\bar{\nu}\nu$ as a function of the momentum measured in the muon spectrometer is shown

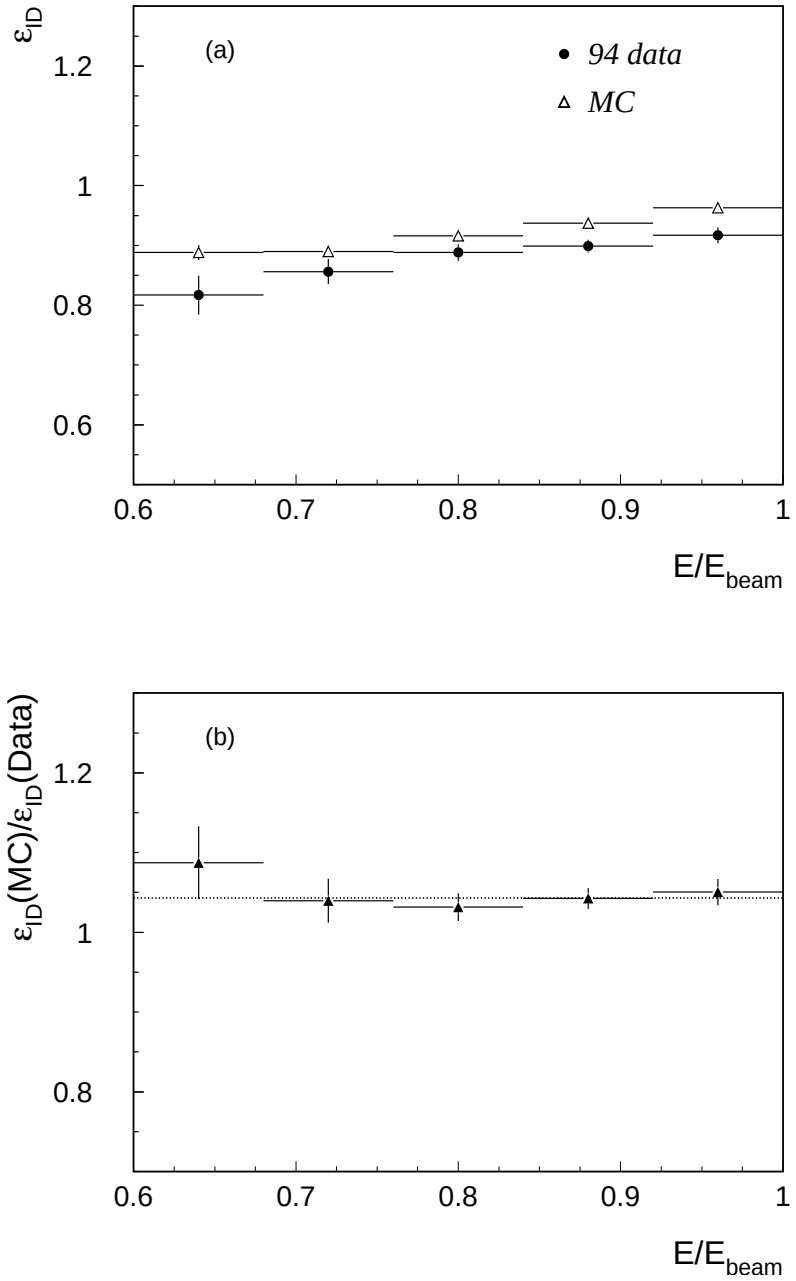

Fig. 7.7: Electron identification for radiative Bhabha events. The upper figure shows the identification efficiency for data and Monte Carlo simulation in dependence on the energy measured in the ECAL. The lower graph gives the ratio of both distributions.

in figure 7.8.

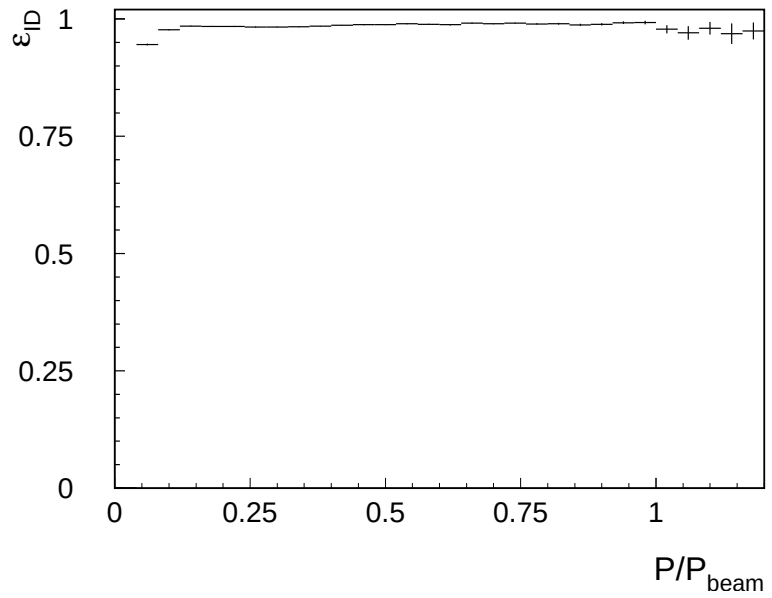

Fig. 7.8: The efficiency for identifying the decay $\tau \to \mu\bar{\nu}\nu$, as determined from Monte Carlo simulation, is plotted as a function of the reconstructed muon energy.

The identification efficiency for muons detected in the muon spectrometer is about 98 percent over all momentum range except for low momentum muons. In addition, muons from hadronic τ decays tend to show up low momenta, therefore a minimal muon momentum of 2.5 GeV is required. In the high momentum region around 45 GeV the sample is dominated by dimuon events leading to an upper limit of 0.92 for muon momentum normalised to the beam energy.

The identification efficiencies for $\tau \to \mu\bar{\nu}\nu$ decays as estimated from the Monte Carlo simulation are listed in table 7.3. The efficiencies are given for the total Monte Carlo sample selected as τ decays, and inside the accepted geometrical and energetic region.

Control samples to study the muon identification are selected for $e^+e^- \to \mu^+\mu^-$ and $e^+e^- \to e^+e^-\,\mu^+\mu^-$ events. The $e^+e^- \to \mu^+\mu^-$ events were tagged by a high momentum muon in one hemisphere. Figure 7.9 shows the identification efficiency for the high energetic muon in the tagged hemisphere. The identification efficiency decreases for muon momenta below the beam energy because of radiated photons which affect the identification requirements on E^9_{ECAL} and E^{25}_{ECAL}. The muon identification efficiency for the control sample from $e^+e^- \to e^+e^-\,\mu^+\mu^-$ is illustrated in figure 7.10.

The muon identification is compared for low momentum muons and high momentum

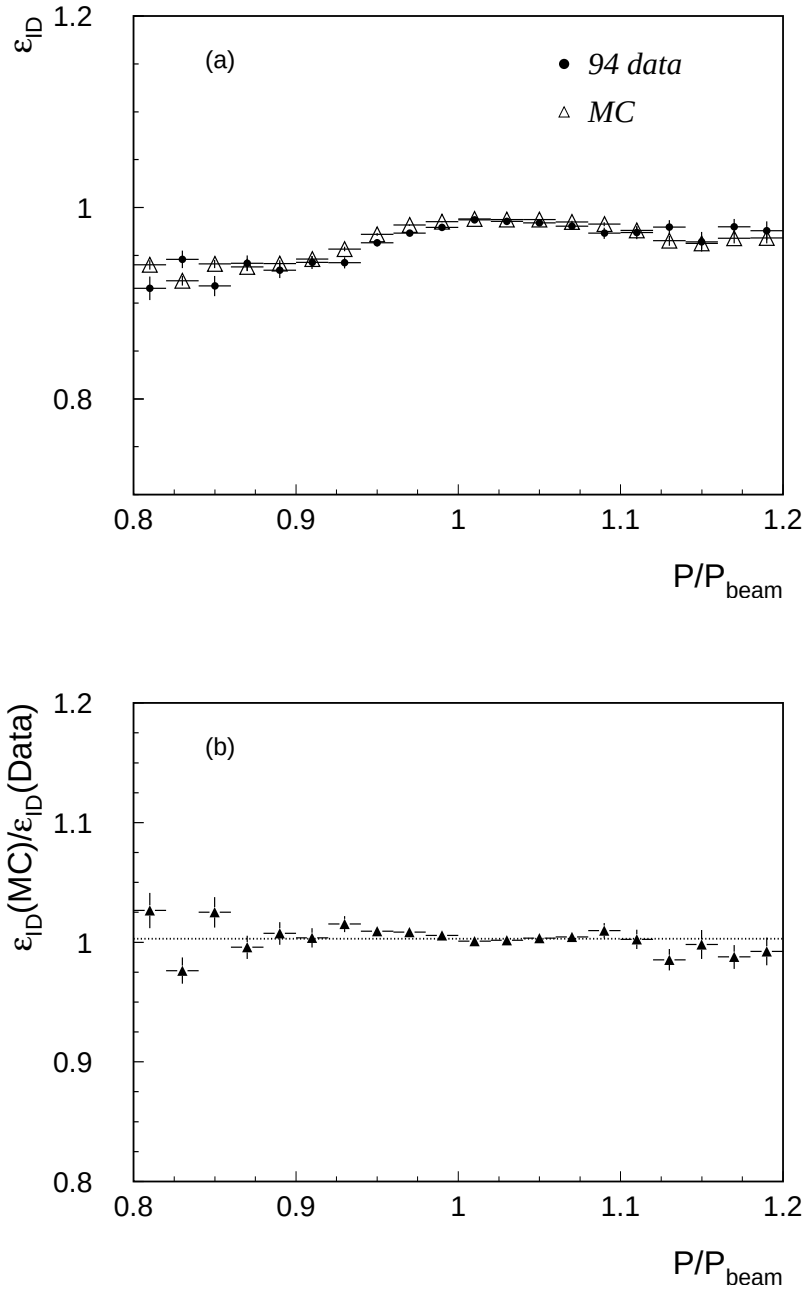

Fig. 7.9: Muon identification for high momentum muons from $e^+e^- \to \mu^+\mu^-$ events. The upper figure shows the identification efficiency for data and Monte Carlo simulation in dependence on the momentum measured in the muon spectrometer. The lower graph gives the ratio of both distributions.

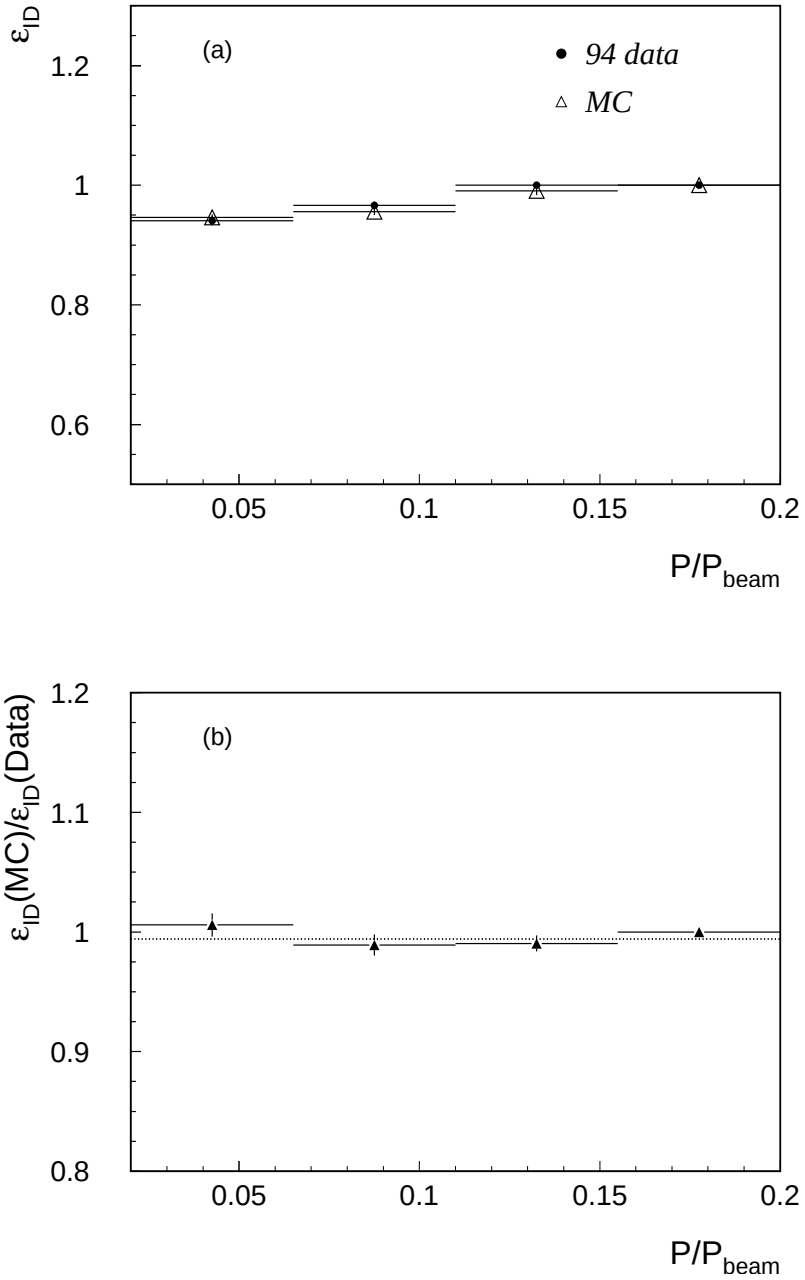

Fig. 7.10: Identification of low momentum muons from $e^+e^- \to e^+e^- \mu^+\mu^-$ events. Figure (a) shows the identification efficiency for data and Monte Carlo simulation in dependence on the momentum measured in the muon spectrometer. The lower graph (b) gives the ratio of both.

	Total efficiency (%)	Inside efficiency (%)
1991+92	76.78 ± 0.19	99.64 ± 0.06
1993	78.61 ± 0.20	99.10 ± 0.07
1994	75.42 ± 0.14	99.28 ± 0.05
1995	74.19 ± 0.18	97.64 ± 0.08

Tab. 7.3: Identification efficiencies for $\tau \to \mu\bar{\nu}\nu$ events with respect to the selected τ events in the simulation. The *inside* efficiency is determined within the geometrical and energetic acceptance. The quoted errors come from the statistics of the Monte Carlo sample.

muons using the control samples. This is done for the muon chamber momentum and the CTS momentum in analogy to the electron identification. No deviations or only very small deviations between data and Monte Carlo simulation are observed as can be seen in table 7.4. As for the electron identification a line is fitted and a slope calculated.

	$\frac{\varepsilon^{ID}_{MC}}{\varepsilon^{ID}_{Data}}$ at $\frac{E}{E_{beam}} = 0.05$	$\frac{\varepsilon^{ID}_{MC}}{\varepsilon^{ID}_{Data}}$ at $\frac{E}{E_{beam}} = 1$	Slope
1991+92	1.004 ± 0.009	1.007 ± 0.002	0.003 ± 0.010
1993	1.010 ± 0.011	1.011 ± 0.002	0.002 ± 0.012
1994	0.999 ± 0.006	1.006 ± 0.001	0.008 ± 0.007
1995	0.993 ± 0.008	1.004 ± 0.002	0.011 ± 0.009

Tab. 7.4: Corrections to the muon identification efficiency.

The identification efficiency for a control sample of radiative $e^+e^- \to \mu^+\mu^-$ events (figure 7.11) shows no momentum dependency. Therefore the correction determined at high muon momenta is applied as an overall correction to the identification efficiency for the Monte Carlo τ sample. The variation of the efficiency after a linear correction in dependence on the error of the slope provides a systematic error.

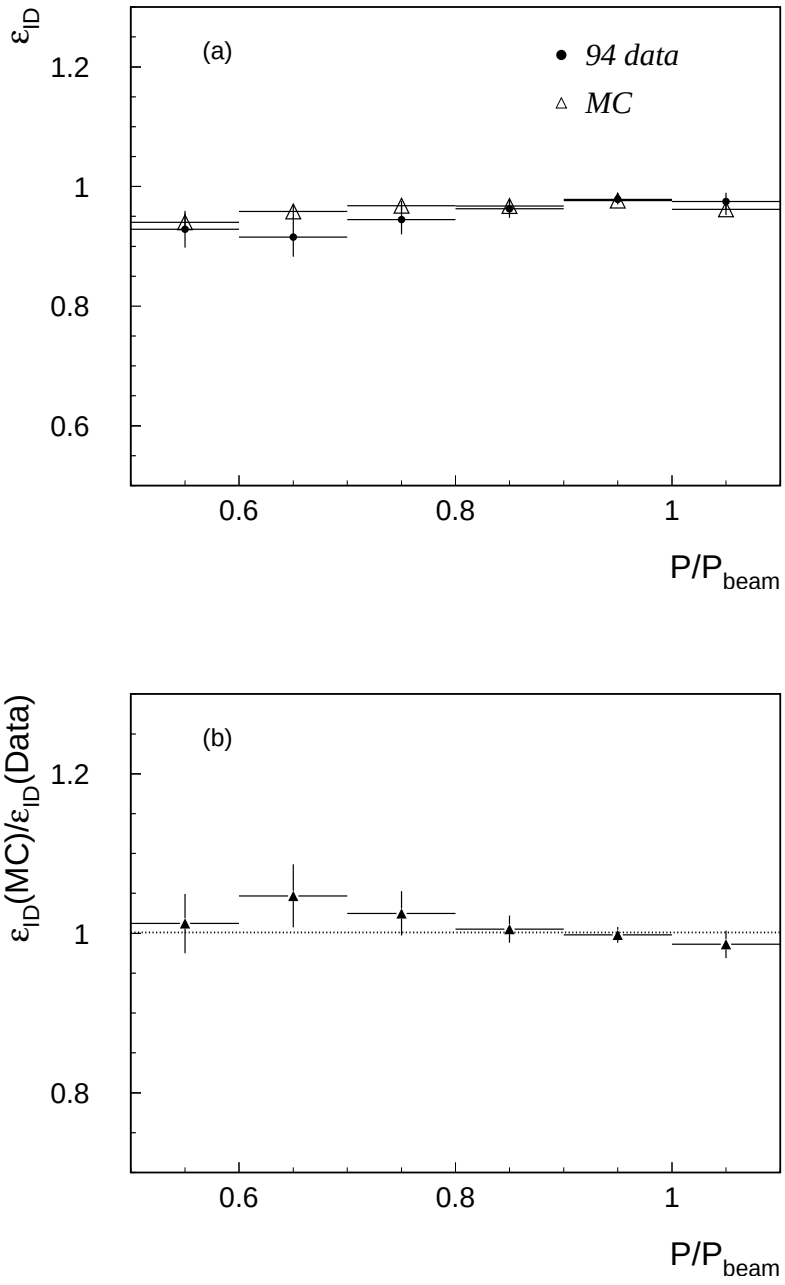

Fig. 7.11: Muon identification for radiative muons from $e^+e^- \to \mu^+\mu^-$ events. The upper figure the identification efficiency for data and Monte Carlo simulation in dependence on the momentum measured in the muon spectrometer. The lower graph gives the ratio of both distributions.

7.3 Systematic Studies

The precision of the measurement relies considerably on the knowledge of the background contributions and identification efficiencies. Therefore their estimates are studied carefully and the following systematic uncertainties are evaluated.

7.3.1 Systematics for the Background Measurements

The background measurements are studied for systematic effects and the uncertainties are evaluated. The background from Bhabha, dimuon, two-photon, hadronic and cosmic muon events are discussed in the successive paragraphs.

Background from $e^+e^- \to e^+e^-$

The described fit of the Bhabha background is based on the assumption that the background passing the τ selection is reproduced well by the simulation. A disagreement could affect the shape of the background distribution used for the fit as well as the fraction of background events used in the fit.

Therefore the spectra for selected Bhabha events in data and in simulation are compared before doing the fit. Cuts on the acoplanarity and the acollinearity similar to those used in the τ selection are applied to include their influence on the resulting spectra for the data and the simulation. Small differences in the order of few percent are observed which are applied as corrections to the spectrum of simulated Bhabha events passing the τ selection.

To increase the sensitivity for the Bhabha background the fit is performed for ECAL energies larger $0.5 \times E_{Beam}$ only. This includes more than 97 percent of the Bhabha background. The fraction of electrons with small ECAL energies has been studied by comparing the simulation and a reference sample of Bhabha data events. Small differences up to 10 percent for the number of such events are obtained. This leads to a maximum uncertainty of 0.3 percent of the fitted background fraction which is very small compared to the error of about 10 percent obtained from the fit.

Background from $e^+e^- \to \mu^+\mu^-$

In analogy to the measurement of the Bhabha background only τ candidates with a momentum measured in the muon chambers larger than $0.6 \times E_{Beam}$ are used for the fit. The amount of muons with a momentum below $0.6 \times E_{Beam}$ is about 35 percent

of the Monte Carlo sample of $e^+e^- \to \mu^+\mu^-$ events passing the τ selection. Using a reference data sample of dimuon events the fraction of such bad measured muons was evaluated to be 8.2 percent in the simulation and 8.6 percent in data. The difference transformed to the selected τ sample yields an error of 1.4 percent for the fitted background fraction. In addition, the inefficiency of the muon chambers is studied for the selected τ data sample. Dimuon events within the τ sample are selected by requiring two MIP's with an CTS momentum larger than 20 GeV each and the tracks with no muon chamber measurement are counted. No difference between the data and the simulation is observed.

The shape of the Monte Carlo spectra for the dimuon events used in the fit was corrected for small deviations taken from a separate dimuon data sample. To consider discrepancies caused by the cuts on acoplanarity and acollinearity from τ selection, these cuts are applied to the reference sample before the spectra are compared.

Background from $e^+e^- \to e^+e^-f\bar{f}$

The scale factors obtained from data luminosity are checked with data. Two-photon event samples are selected from data and the normalisation between data and the simulation are evaluated from the distribution of the difference of the transverse momenta ΔP_{trans}. Deviations of about 10 percent to the expected cross section are found. Then the distribution of ΔP_{trans} is compared for data and simulation in the τ selected sample alternately releasing cuts against two-photon events. Taking the statistical errors into account the discrepancies did not exceed 15 percent. Since the background is small this is taken as an error on the background fractions estimated from the simulation.

Background from $e^+e^- \to q\bar{q}$

Since hitherto at least 12 ECAL clusters were required for the events used to determine the $e^+e^- \to q\bar{q}$ background events with lower multiplicities have so far not been considered. The fraction of events in the reference sample with less than 6 clusters in one hemisphere is estimated to be about 20 percent. Assuming that the distribution of the number of clusters is independent for both hemispheres, the total fraction of events with less than 12 clusters is 4 percent. Therefore an error of 4 percent is added to the fitted amount of $e^+e^- \to q\bar{q}$ events.

Background from Cosmic Muons

The density of cosmic muon events in the band seen in DCA_2 against DCA_1 (figure 5.6) is taken as constant in DCA when evaluating the background rate. Studying the distributions for the DCA shows a slight linear decrease of the number of events with growing DCA. This yields 0.4 percent as relative error on the cosmic muon background rate.

Furthermore the background measurement is checked by releasing the τ selection cuts against cosmic muons and fitting the difference of the time information from the scintillation counters. A fit to the τ data sample was performed with the DCA selected cosmic muon sample and the $\tau\tau$ Monte Carlo simulation for time differences around 5 ns, where cosmic muons are dominant. The fitted cosmic muon rate is 1.05 ± 0.04 times the rate estimated from the DCA band.

Summary for the Background Measurements for the Tau Sample

The observed deviations between data and Monte Carlo distributions have been found to be small compared to the errors of the background fractions. They are assumed to be the same for the data samples for the different run periods. Table 7.5 summarises these uncertainties.

Channel	Uncertainty
$e^+e^- \to \mu^+\mu^-$	0.014
$e^+e^- \to e^+e^-$	0.003
$e^+e^- \to e^+e^-\ \mu^+\mu^-$	0.15
$e^+e^- \to e^+e^-\ e^+e^-$	0.15
$e^+e^- \to e^+e^- q\bar{q}$	0.15
cosmic muons	0.004
$e^+e^- \to q\bar{q}$	0.04

Tab. 7.5: The relative systematic errors on the measured background levels for the τ sample.

Background Measurements for the Leptonic Samples

The determination of the backgrounds in the samples with decays identified as $\tau \to e\bar{\nu}\nu$ and $\tau \to \mu\bar{\nu}\nu$ is based on the background measurements for the τ sample and underly the same systematics. In addition, it implies that the lepton identification for the background is the same in data and Monte Carlo simulation. The background consists of dilepton events of the same lepton flavour as the lepton from τ decay. The lepton identification was studied for these backgrounds using data samples. As it is shown in the next section, only a very small disagreement between data and Monte Carlo simulation was obtained and the systematic effects from the background rates caused by the identification are therefore neglected.

7.3.2 Identification of Leptonic Tau Decays

The statistical error of the identification efficiencies for the leptonic τ decays as estimated from Monte Carlo simulation is taken as systematic error.

Additional systematic errors come from the corrections for the lepton identification efficiencies. One is the statistical error on the correction at high lepton energies which is applied as an overall correction together with the fitted correction slope. The other is caused by the error of the slope. The slope is varied inside these errors and convoluted with the Monte Carlo identification efficiency for the τ sample bin by bin. The total lepton identification is then calculated for the τ sample and its variation taken as the error.

7.3.3 Trigger Efficiency

The total trigger efficiency for $e^+e^- \to \tau^+\tau^-$ events is larger than 99.9 percent [91,92]. A notable influence from the small inefficiency can only arise if the inefficiency affects leptonic τ decays especially. In a conservative way assuming that only events of the same leptonic decay mode are not triggered this leads to

$$\Delta B_l = \frac{0.001}{B_l} = 0.006 \tag{7.7}$$

since any change ΔN_l for the number of leptonic decays contributes to the number of all decays by $\Delta N_l B_l$.

7.3.4 Bias due to Tau Selection

The bias for the leptonic branching fractions results from the correlated cuts applied. Table 7.6 shows the bias for both branching fractions as estimated from the Monte Carlo simulation. The error from Monte Carlo statistics is taken as the systematics.

	1991+92	1993	1994	1995
$\frac{\varepsilon_{\tau\tau}^{sel}}{\varepsilon_{l}^{sel}}$ for $\tau \to e\bar{\nu}\nu$	0.9987±0.0036	1.0024±0.0039	0.9950±0.0027	0.9961±0.0035
$\frac{\varepsilon_{\tau\tau}^{sel}}{\varepsilon_{l}^{sel}}$ for $\tau \to \mu\bar{\nu}\nu$	1.0086±0.0018	0.9970±0.0039	0.9967±0.0027	0.9980±0.0035

Tab. 7.6: Selection bias for the branching fractions as estimated from the Monte Carlo.

In addition the correlated cuts are varied in a range changing the selection efficiency in the order of a few percent. This allows to monitor the stability of the selection against these cuts and provides a test of the background measurements. The variation in the branching fraction is treated as the resulting systematic error.

Furthermore, the influence of the correlated cuts was studied by applying a tight hemisphere tag selection. In this selection the background is suppressed by cuts in the opposite hemisphere mainly, starting with the dilepton preselected sample for the barrel region. The efficiency of this selection is by a factor 0.5 lower than for the selection used for this measurement, while the background fractions are twice as large. Considering the correlations and statistical fluctuations the branching fractions measured from both selections are consistent for each year. This can be interpreted as a confirmation of the applied method to combine hemisphere cuts with correlated ones, and of the understanding of the systematic influence from the correlated cuts.

7.3.5 Hadron Misidentification

The final sample of identified leptonic τ decays contains a small fraction from other τ decays, where the decay particle is misidentified as a lepton and which are mostly hadrons. The fraction of such misidentified decays is estimated from the simulation.

The misidentification is studied applying the lepton identification with looser cuts against the background. The spectra for the variables relevant for these cuts are compared for data and Monte Carlo simulation and the background from misidentified τ decays is estimated by a fit. Deviations in the order of 5 percent are found for different cuts and are included into the systematic error.

The systematic error from the knowledge of 1-prong hadronic τ decays is small since it enters through the misidentification of hadrons into leptons:

$$\frac{\Delta f^{\tau}_{h\to l}\; B_h^{1-prong}\; \Delta B_h^{1-prong}}{B_l}. \tag{7.8}$$

The systematic error is calculated for $\Delta B_h^{1-prong} = 2\%$.

7.3.6 Systematics from Polarisation

The impact of the energy cuts for the branching fractions depends on the τ polarisation. Leptons from negatively polarised τ leptons are affected more by the cuts imposed at high energy (against Bhabha and dimuon events) than those from the opposite polarisation, while low energy cuts remove more frequently leptons from the positively polarised τ leptons. The identification efficiency for leptonic τ decays, $\varepsilon_l^{\pm}$, is obtained for each helicity from a Monte Carlo study and is translated into a systematic error in dependency on the limited knowledge of the τ polarisation:

$$\Delta\varepsilon_l = \frac{|\varepsilon_l^- - \varepsilon_l^+|}{2}\Delta P\ . \tag{7.9}$$

From the error on τ polarisation, $\Delta P = 0.2$, taken from the L3 measurement [89], $\Delta\varepsilon_l$ is calculated. The variation in the branching fraction in dependence on $\Delta\varepsilon_l$ yields the systematic error.

7.3.7 Momentum Range Restriction

The final leptonic samples do not include the full momentum range. The systematic influence of this restriction is estimated from a Monte Carlo study by varying the upper and the lower limit in reasonable ranges. The maximum deviation in the branching fraction is taken as the systematic error.

7.4 Summary for Data Analysis

The background contributions and identification efficiencies, together with their uncertainties, are evaluated for the data samples of the different years. In the next section all the results from data anaylsis relevant for the measurement of the leptonic branching fractions are summarised.

7.4.1 Tau Selection

An overview over all background measurements for the τ samples with their final uncertainties gives table 7.7. The different background contributions are added for each data set, taking the errors as independend from each other. The resulting total background fractions together with the statistics of the selected τ samples summarises table 7.8.

	Background in τ sample [%]			
Channel	1991+92	1993	1994	1995
$e^+e^- \to \mu^+\mu^-$	0.96±0.08	0.97±0.09	0.94±0.05	1.11±0.08
$e^+e^- \to e^+e^-$	1.19±0.14	1.67±0.19	1.16±0.07	1.33±0.11
$e^+e^- \to e^+e^-\ \mu^+\mu^-$	0.03±0.01	0.12±0.02	0.03±0.01	0.14±0.02
$e^+e^- \to e^+e^-\ e^+e^-$	0.15±0.03	0.27±0.04	0.15±0.02	0.29±0.05
$e^+e^- \to e^+e^-q\bar{q}$	0.04±0.02	0.06±0.03	0.07±0.02	0.06±0.03
Cosmic muons	0.04±0.01	0.11±0.02	0.10±0.01	0.17±0.03
$e^+e^- \to q\bar{q}$	0.22±0.05	0.23±0.06	0.24±0.05	0.14±0.01
Total	2.64±0.17	3.42±0.23	2.70±0.10	3.24±0.15

Tab. 7.7: The background contributions for the selected τ sample together with their uncertainties. The total background contribution is the sum for the different backgrounds. The errors are added quadratically.

	1991+92	1993	1994	1995
$N_\tau = 2\,N_{\tau\tau}$	42086	29620	65392	26158
$f_l^{non-\tau}$	0.0264±0.0017	0.0342±0.0023	0.0270±0.0010	0.0324±0.0015

Tab. 7.8: The number of events selected as τ decays from data for the different years, N_τ, and the correction for the fraction of non-τ events, $f_l^{non-\tau}$.

7.4.2 Identification of Leptonic Tau Decays

The background contributions for events identified as $\tau \to e\bar{\nu}\nu$ and $\tau \to \mu\bar{\nu}\nu$ are listed in table 7.9. A summary for the samples of identified leptonic decays is given in

table 7.10 for both decays. The background fractions with their uncertainties are also listed there.

	Background in $\tau \to e\bar{\nu}\nu$ sample [%]			
Channel	1991+92	1993	1994	1995
$e^+e^- \to e^+e^-$	0.51±0.13	0.72±0.18	0.41±0.04	0.42±0.05
$e^+e^- \to e^+e^-\ e^+e^-$	0.92±0.20	1.70±0.34	0.91±0.19	1.68±0.34
Total	1.42±0.24	2.43±0.38	1.32±0.19	2.11±0.34

	Background in $\tau \to \mu\bar{\nu}\nu$ sample [%]			
Channel	1991+92	1993	1994	1995
$e^+e^- \to \mu^+\mu^-$	0.99±0.13	1.34±0.19	0.92±0.07	1.12±0.10
$e^+e^- \to e^+e^-\ \mu^+\mu^-$	0.16±0.06	0.35±0.09	0.16±0.06	0.42±0.11
Cosmic muons	0.14±0.07	0.20±0.09	0.04±0.02	0.06±0.05
Total	1.29±0.16	1.89±0.23	1.11±0.09	1.60±0.15

Tab. 7.9: The background contributions from non-τ events in the samples of identified leptonic τ decays. The upper table is for the decays identified as $\tau \to e\bar{\nu}\nu$, the lower for the decay $\tau \to \mu\bar{\nu}\nu$. The contributions are added for the data sets of the different years separately, taking the errors as independent.

The electron energy measured from the ECAL for the whole data sample of decays identified as $\tau \to e\bar{\nu}\nu$ is shown in figure 7.12 together with the Monte Carlo simulation. Figure 7.13 gives the muon chamber momentum for the final $\tau \to \mu\bar{\nu}\nu$ sample. Good aggrement between data an Monte Carlo simulation is observed for both decay modes.

7.4.3 Systematic Uncertainties

The systematic uncertainties are evaluated independently for the data samples of the different years. Most of them are caused by Monte Carlo statistics or by the statistics of the reference data samples, and therefore uncorrelated. Small correlations are considered for the systematic uncertainties which have similar influence for all years.

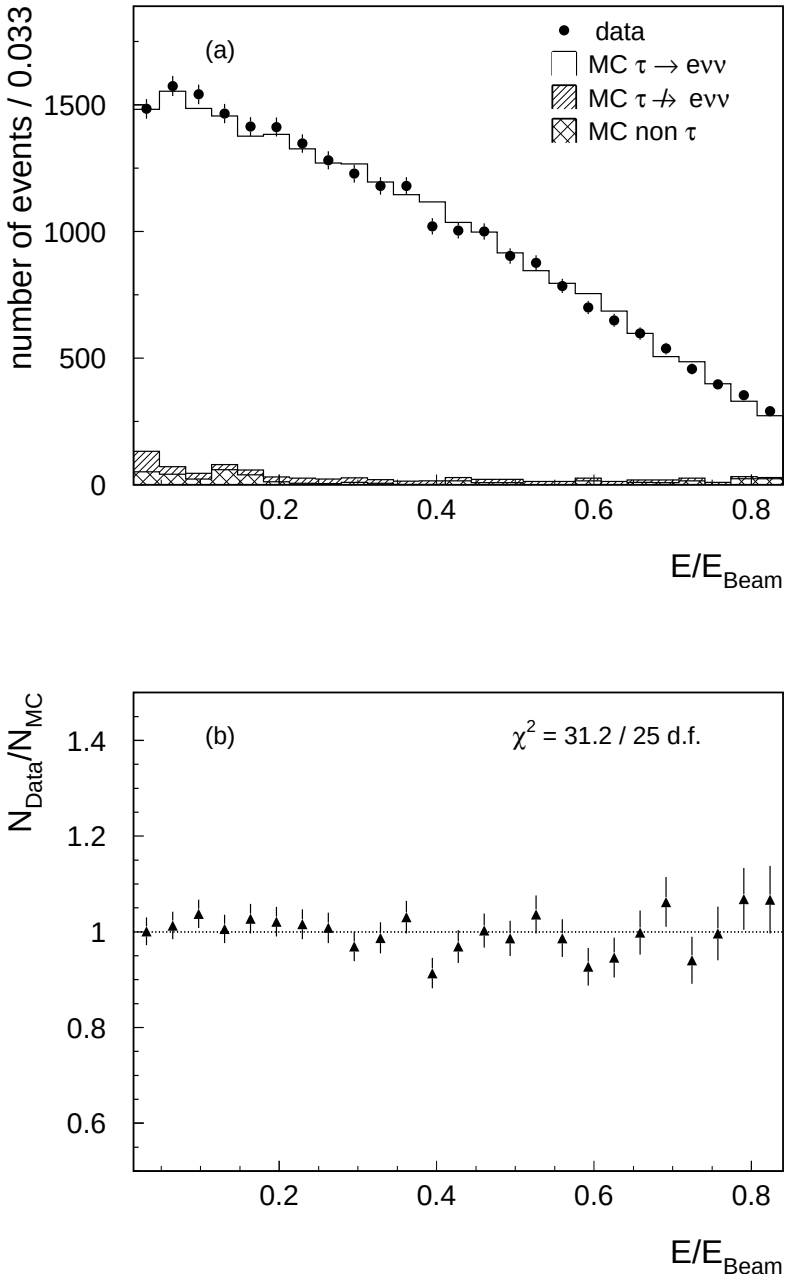

Fig. 7.12: The upper graph shows the energy distribution for events identified as $\tau \to e\bar{\nu}\nu$, for data and for simulation. The ratio of data and Monte Carlo simulation including the background is given in the lower figure. Good aggreement between data and simulation is observed.

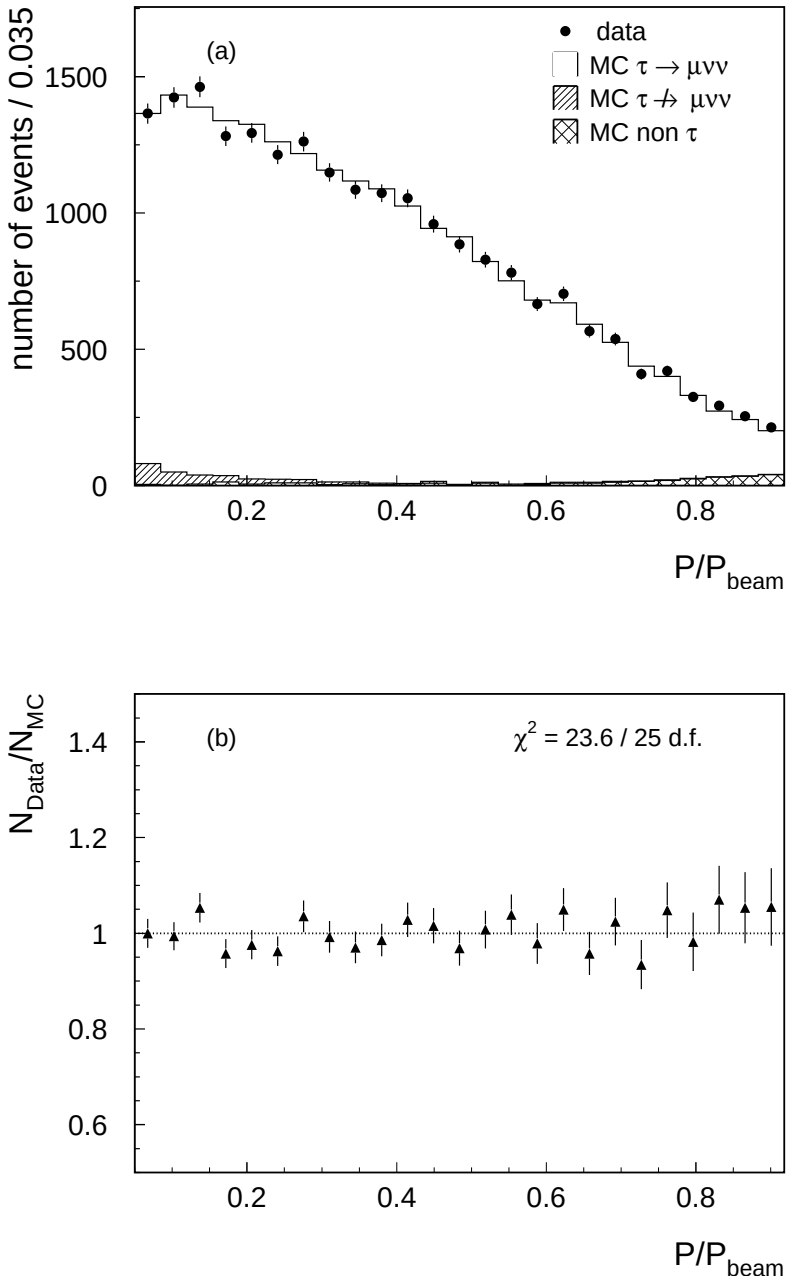

Fig. 7.13: The momentum measured in the muon spectrometer for events identified as $\tau \to \mu\bar{\nu}\nu$ (a) and the ratio between data and Monte Carlo simulation (b). The ratio includes the Monte Carlo simulation for the background and illustrates the good aggreement between data and simulation.

	1991+92	1993	1994	1995
$N_e\ (\tau \to e\bar{\nu}\nu)$	6519	4525	9754	3878
ε_e^{ID}	85.94±0.26	83.62±0.29	83.86±0.17	82.75±0.26
$f_e^{non-\tau}$	0.0142±0.0024	0.0243±0.0038	0.0132±0.0019	0.0211±0.0034
$f_e^{\tau \nrightarrow e}$	0.0204±0.0012	0.0174±0.0011	0.0170±0.0010	0.0176±0.0010
$N_\mu\ (\tau \to \mu\bar{\nu}\nu)$	5682	3984	8554	3289
ε_μ^{ID}	76.22±0.23	77.65±0.24	75.10±0.17	74.54±0.24
$f_\mu^{non-\tau}$	0.0129±0.0016	0.0189±0.0023	0.0111±0.0009	0.0160±0.0015
$f_\mu^{\tau \nrightarrow \mu}$	0.0141±0.0009	0.0138±0.0009	0.0144±0.0009	0.0117±0.0008

Tab. 7.10: The number of decays identified as leptonic τ decays from data for the different data samples, N_l. The corrected identification efficiency, ε_l^{ID}, and the corrections for the background contributions from non-τ events, $f_l^{non-\tau}$, and from other τ decays, $f_l^{\tau \nrightarrow l}$, are given with their uncertainties.

The uncorrelated systematic uncertainties for the measurement of B_e are summarised in table 7.11, and for B_μ in table 7.13. The correlated errors are given in tables 7.12 and 7.14 for both leptonic decay modes.

Furthermore, correlations are evaluated between the systematic uncertainties on B_e and B_μ (table 7.15). They result from the uncertainty on the background fractions in the common τ sample, used for both measurements. The uncertainty on the polarisation is considered as correlated because the polarisation in the simulation is the same for all τ pairs. Furthermore, the influence of the correlated cuts was studied. The cuts were varied and the correlation in the branching fractions B_e and B_μ is evaluated from the Monte Carlo simulation.

Uncorrelated systematic uncertainties for B_e				
Source	1991+92	1993	1994	1995
Background in τ sample	0.031	0.042	0.018	0.025
Background in leptonic sample	0.025	0.048	0.024	0.046
Misidentified τ decays	0.012	0.012	0.008	0.010
Bias from selection	0.064	0.071	0.048	0.062
Lepton identification (MC)	0.028	0.034	0.023	0.029
Correction identification	0.047	0.053	0.027	0.046
Slope id corrections	0.052	0.070	0.031	0.040
Cut on barrel region	0.014	0.035	0.028	0.024
Cut on opening angle	0.015	0.022	0.026	0.030
Cut on acollinearity	0.029	0.032	0.028	0.026
Cut on acoplanarity	0.026	0.035	0.005	0.031
Minimum energy cut	0.061	0.039	0.037	0.029
Maximum energy cut	0.036	0.044	0.039	0.030
Total	0.136	0.160	0.103	0.127

Tab. 7.11: Summary of the systematics for B_e, uncorrelated for the data samples in the different years. All errors are added taking them independent from each other.

Correlated systematic uncertainties for B_e	
Source	Correlated error
Background in τ sample	0.006
Background in leptonic sample	0.035
Misidentified τ decays	0.016
Hadronic 1-Prong rate	0.013
Trigger efficiency	0.006
Polarisation uncertainty	0.003
Total	0.042

Tab. 7.12: Summary of the correlated systematic uncertainties for B_e. The resulting errors for the complete data sample including all years are quoted.

Uncorrelated systematic uncertainties for B_μ				
Source	1991+92	1993	1994	1995
Background in τ sample	0.031	0.040	0.018	0.024
Background in leptonic sample	0.005	0.010	0.005	0.011
Misidentified τ decays	0.011	0.011	0.008	0.009
Bias from selection	0.064	0.068	0.047	0.059
Lepton identification (MC)	0.043	0.043	0.033	0.040
Correction identification	0.031	0.032	0.022	0.036
Slope id corrections	0.064	0.073	0.043	0.057
Cut on Barrel	0.054	0.027	0.014	0.055
Cut on opening angle	0.047	0.028	0.025	0.025
Cut on acollinearity	0.028	0.014	0.028	0.039
Cut on acoplanarity	0.013	0.008	0.015	0.008
Minimum energy cut	0.019	0.014	0.026	0.039
Maximum energy cut	0.007	0.015	0.009	0.025
Total	0.136	0.130	0.093	0.133

Tab. 7.13: Summary of the systematics for B_μ, uncorrelated for the data samples in the different years. All errors are added taking them independent from each other.

Correlated systematic uncertainties for B_μ	
Source	Correlated error
Background in τ sample	0.006
Background in leptonic sample	0.024
Misidentified τ decays	0.012
Hadronic 1-Prong rate	0.013
Trigger efficiency	0.006
Polarisation uncertainty	0.003
Total	0.031

Tab. 7.14: Summary of the correlated systematic uncertainties for B_μ. The resulting errors for the complete data sample including all years are quoted.

Source	ΔB_e	ΔB_μ
Background in τ sample	0.013	0.013
Hadronic 1-Prong rate	0.013	0.013
Polarisation uncertainty	0.003	0.003
Cut on acollinearity	0.012	0.009
Cut on acoplanarity	0.004	0.004
Total	0.023	0.021

Tab. 7.15: Summary of the correlated systematics for both leptonic τ decay modes.

Chapter 8

RESULTS

In this chapter the τ leptonic branching fractions are determined for the different data samples separately and combined into a result for the complete LEP I data sample. This result is interpreted in the context of the Standard Model and limits on the mass of the τ neutrino and the mass of a charged Higgs boson are derived. Finally the measurement is combined with the measurements at the other LEP experiments.

8.1 Results

From the number of selected τ events and identified leptonic decays, together with their relevant efficiencies, background fractions and all systematic uncertainties, the leptonic branching fractions are calculated using equation 4.6. Table 8.1 summarises the results for the different years.

	B_e	B_μ
1991+92	$(17.855 \pm 0.203 \pm 0.143)\%$	$(17.586 \pm 0.217 \pm 0.141)\%$
1993	$(18.180 \pm 0.249 \pm 0.170)\%$	$(17.304 \pm 0.255 \pm 0.137)\%$
1994	$(17.643 \pm 0.165 \pm 0.108)\%$	$(17.390 \pm 0.175 \pm 0.096)\%$
1995	$(17.739 \pm 0.263 \pm 0.136)\%$	$(16.921 \pm 0.276 \pm 0.136)\%$

Tab. 8.1: Measurements of the τ leptonic branching fractions for the different data sets. The first error quoted is statistical, the second the sum of the correlated and uncorrelated systematic errors.

The statistical error is calculated from the number of events in the τ sample, N_τ, and the number of events, identified as leptonic τ decays, N_l :

$$\Delta B_l = \left(\frac{N_l}{N_\tau}\right)^{-1} \cdot B_l \cdot \Delta\left(\frac{N_l}{N_\tau}\right) \ , \tag{8.1}$$

with $\Delta\left(\frac{N_l}{N_\tau}\right)$ being the binominal error on $\frac{N_l}{N_\tau}$. The systematic error includes the uncorrelated and correlated uncertainties.

The measurements for different years are combined to a weighted average of

$$B_e = (17.806 \pm 0.104_{stat} \pm 0.076_{sys})\% \tag{8.2}$$

$$B_\mu = (17.342 \pm 0.110_{stat} \pm 0.067_{sys})\% \ . \tag{8.3}$$

The systematic error is combined by accounting for the correlations.

The χ^2 of the measurements, assuming the average as the true value and including statistical and systematic errors, is $2.3/3\,d.o.f.$ for B_e (figure 8.1) and $2.8/3\,d.o.f.$ for B_μ (figure 8.2). This corresponds to a probability of 48.7% for B_e and 57.6% for B_μ, while from Gaussian statistics one expects 50%. Thus the results for the different samples agree very well.

The result of this measurement is in agreement with previous measurements of the L3 collaboration [93–95]. A gain of precision by about 50 percent is achieved compared to this old analysis. The understanding of systematic effects has significally improved.

8.2 Test of Lepton Universality

The measured branching fractions of the τ allow for a direct test of $e-\mu$ universality in the weak charged current (see section 1.6). Using equation 1.49, and respecting the correlation between the measurements, the ratio of the two leptonic branching fractions leads to:

$$\frac{g_\mu}{g_e} = 1.0007 \pm 0.0051 \ , \tag{8.4}$$

consistent with unity. This result is complementary to the one obtained from pion decays [56]:

$$\frac{g_\mu}{g_e} = 1.0021 \pm 0.0016 \ , \tag{8.5}$$

since pion decays test only the coupling to a longitudinal W, with a helicity equal to zero, because the pion is of spin 0. The leptonic τ decays measure a transverse W, with a helicity of ± 1. This is a consequence of the helicity conservation in weak charged currents.

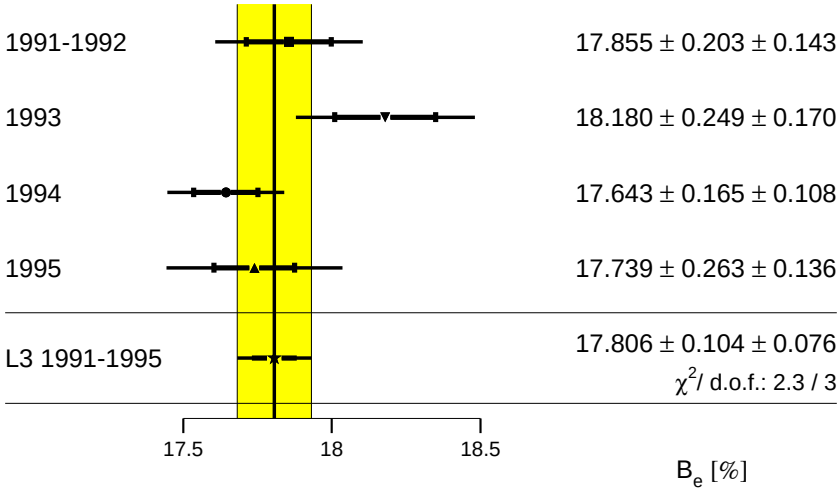

Fig. 8.1: Measurements of the branching fractions of the decay $\tau \to e\bar{\nu}\nu$ for the different data sets and their average. The correlations in the systematic error are taken into account.

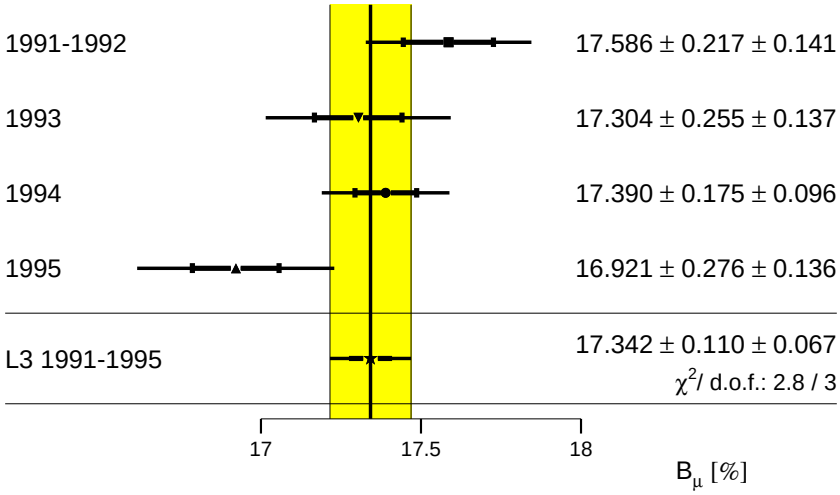

Fig. 8.2: Measurements of the branching fractions of the decay $\tau \to \mu\bar{\nu}\nu$ for the different data sets. The average considers the correlations in the systematic error.

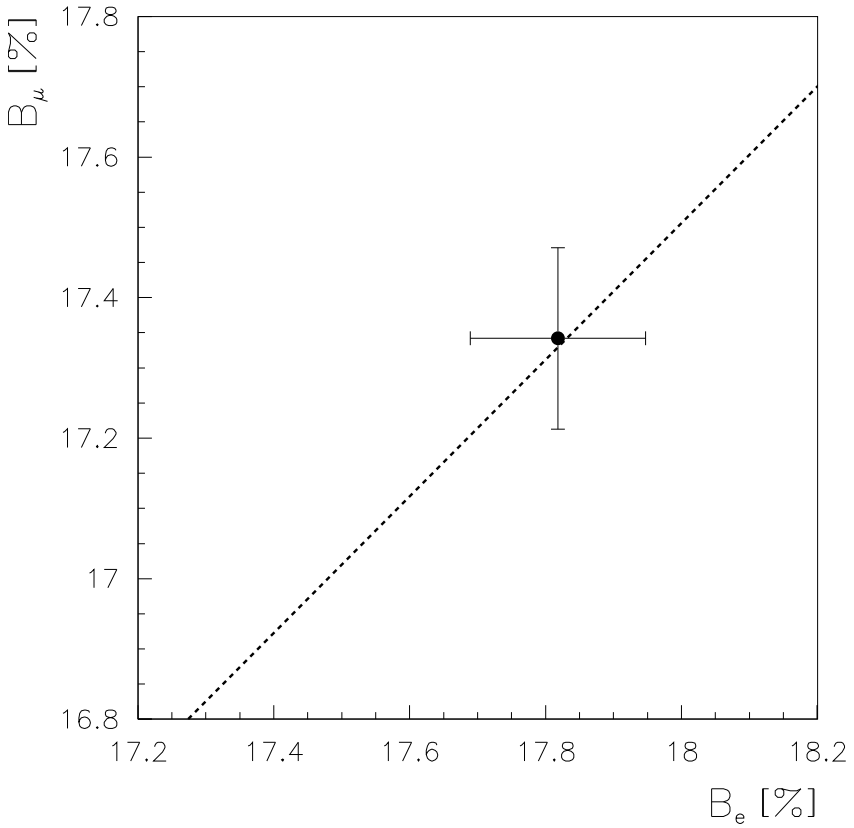

Fig. 8.3: The measured leptonic branching fractions plotted against each other. The line corresponds to the phase space correction.

Since B_e and B_μ are consistent with $e-\mu$ universality, as illustrated in figure 8.3, they are combined into a branching fraction for the decay of the τ into a massless charged lepton, $\bar{B}_l$, correcting for the phase space suppression:

$$\bar{B}_l = (17.818 \pm 0.077_{stat} \pm 0.053_{sys})\% \; . \tag{8.6}$$

The systematic error accounts for the correlation between both branching fraction measurements.

Within the Standard Model, the τ lifetime can be predicted from equations 1.46 and 1.35. Using the universal leptonic branching fraction $\bar{B}_l$ a τ lifetime of

$$\tau_\tau = (290.8 \pm 1.8)\; fs \tag{8.7}$$

is obtained (figure 8.4).

This result is consistent with the direct measurement performed at L3 [52]:

$$\tau_\tau = (293.2 \pm 2.5)\; fs \; , \tag{8.8}$$

and with the world average [4] of τ lifetime (figure 8.5). This indicates that Standard Model is correct.

Together with the world averages of the lepton masses and the muon lifetime [4] a test of the leptonic couplings at the $Wl\bar{\nu}_l$ vertex using equation 1.51 is done:

$$\frac{g_\tau}{g_\mu} = 0.9955 \pm 0.0036_{(B_e)} \pm 0.0043_{(\tau_\tau)} \pm 0.0004_{(m_\tau)}, \tag{8.9}$$

$$\frac{g_\tau}{g_e} = 0.9962 \pm 0.0037_{(B_\mu)} \pm 0.0043_{(\tau_\tau)} \pm 0.0004_{(m_\tau)}. \tag{8.10}$$

The universality $\tau-\mu$ and $\tau-e$ is verified at 6 per mille.

The couplings $G_{\tau l}$, as defined in section 1.5 in analogy to the Fermi constant, are obtained from the branching fractions and the τ lifetime from the L3 measurement to:

$$G_{\tau e} = (1.1611 \pm 0.0065) \times 10^{-5}\,\mathrm{GeV}^{-2} \tag{8.11}$$

$$G_{\tau\mu} = (1.1620 \pm 0.0066) \times 10^{-5}\,\mathrm{GeV}^{-2} \; . \tag{8.12}$$

They are in very good agreement with the Fermi constant G_F, but their errors are nearly 500 times larger.

The world average of the τ lifetime improves the precision of the $\tau-\mu$ and $\tau-e$ universality test to a level of 4 per mille:

$$\frac{g_\tau}{g_\mu} = 1.0010 \pm 0.0036_{(B_e)} \pm 0.0021_{(\tau_\tau)} \pm 0.0004_{(m_\tau)}, \tag{8.13}$$

$$\frac{g_\tau}{g_e} = 1.0017 \pm 0.0037_{(B_\mu)} \pm 0.0021_{(\tau_\tau)} \pm 0.0004_{(m_\tau)}. \tag{8.14}$$

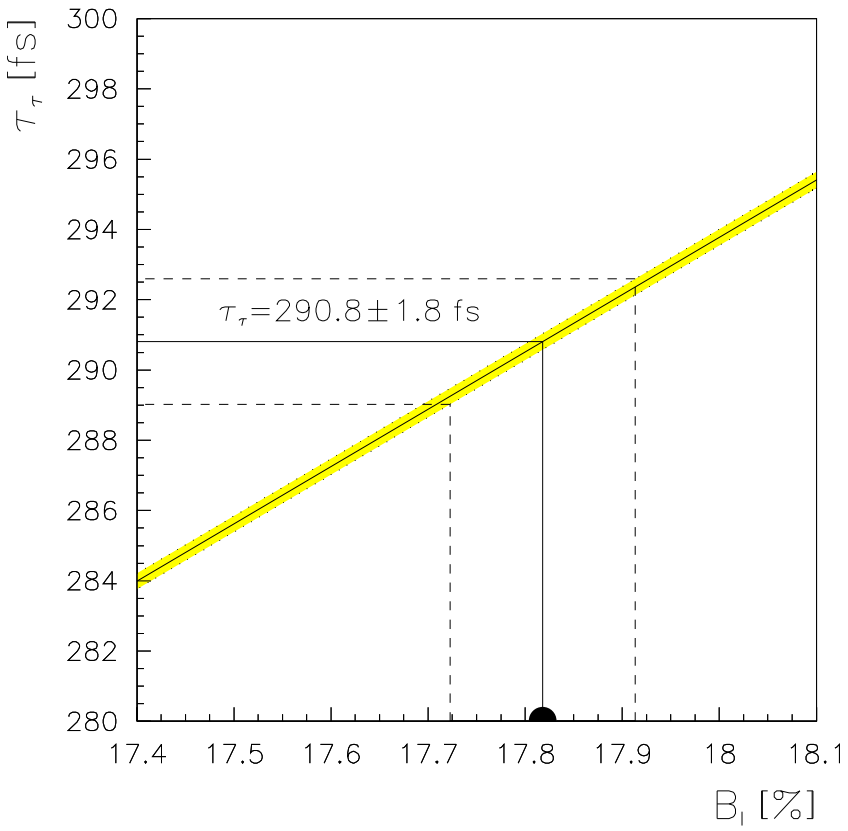

Fig. 8.4: The relation between τ lifetime and leptonic branching fraction. The straight line corresponds to the Standard Model prediction, its width is due to the uncertainty on the τ mass. The measured universal leptonic branching fraction predicts the drawn τ lifetime.

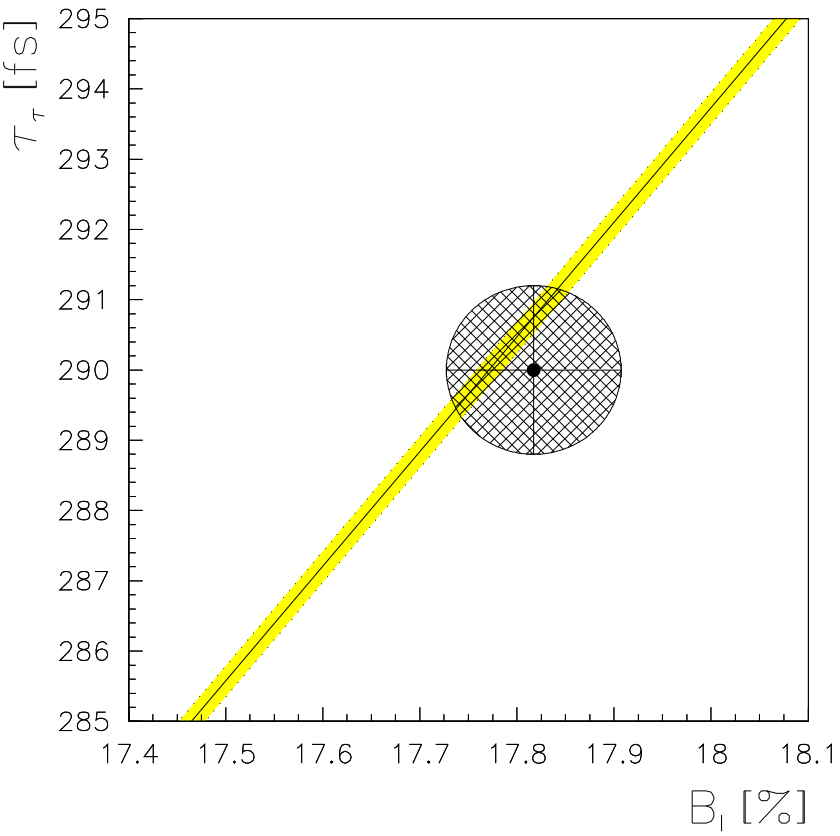

Fig. 8.5: The τ lifetime (world average) plotted versus the measured universal leptonic branching fraction. The straight line corresponds to the Standard Model prediction, its width is due to the uncertainty on the τ mass. The hatched area is the 68% confidence level contour.

8.3 Measurement of α_s

R_τ is calculated from the universal leptonic branching fraction, $\bar{B}_l$:

$$R_\tau = \frac{1}{\bar{B}_e} - 1 - c_f \ , \tag{8.15}$$

with c_f defined in equation 1.50, and $\bar{B}_e = \bar{B}_l \, f(\frac{m_e^2}{m_\tau^2}) = \bar{B}_l$, to

$$R_\tau \ = \ 3.612 \ \pm \ 0.030 \ . \tag{8.16}$$

The strong coupling constant α_s at the τ mass scale is extracted as described section 1.6:

$$\alpha_s(m_\tau) \ = \ 0.324 \ \pm \ 0.009_{exp} \ \pm \ 0.017_{theory} \tag{8.17}$$

where the experimental error comes from the uncertainty on R_τ. The theoretical uncertainties are listed in table 8.2. They are dominated by the renormalisation-scheme (RS) and scale dependences. The scale dependence is taken from [50], while the contribution from RS was estimated in [96].

Source	$\Delta\alpha_s(m_\tau)$	$\Delta\alpha_s(m_Z)$
RS dependence	0.010	0.0011
Scale dependence	0.009	0.0009
K_4 dependence	0.006	0.0007
Non-perturbative contributions	0.005	0.0006
CKM matrix elements	0.005	0.0006
Electroweak corrections	0.004	0.0005
Running $\alpha_s(m_\tau) \rightarrow \alpha_s(m_Z)$	-	0.0003
Total	0.017	0.0019

Tab. 8.2: Theoretical uncertainties on $\alpha_s(m_\tau)$ and $\alpha_s(m_Z)$

The value of $\alpha_s(m_\tau)$ is evolved to the Z mass scale for comparison with other measurements. The running of α_s is described by the renormalisation group equations (see for example [97]). Following the procedure described in [98], $\alpha_s(m_Z)$ is extrapolated from $\alpha_s(m_\tau)$. This procedure has been shown to introduce an uncertainty of 0.0003 [98] to the extracted value of $\alpha_s(m_Z)$, which is

$$\alpha_s(m_Z) \ = \ 0.1191 \ \pm \ 0.0009_{exp} \ \pm \ 0.0019_{theory} \ . \tag{8.18}$$

It is in excellent agreement with the world average [4]:

$$\alpha_s(m_Z) = 0.119 \pm 0.002 \tag{8.19}$$

and supports the running of the QCD coupling constant.

8.4 Mass of the Tau Neutrino

The ν_τ mass is estimated from a comparison of the measured leptonic τ decay rate to the calculated rate as a function of m_{ν_τ}. From the measured leptonic branching fractions and the τ lifetime obtained by L3 the total leptonic decay rate, $\Gamma^{meas}_{e+\mu}$, is obtained:

$$\Gamma^{meas}_{e+\mu} = \frac{B_\mu + B_e}{\tau_\tau} \tag{8.20}$$

$$= (1.20 \pm 0.01) \times 10^{-3} fs^{-1} \tag{8.21}$$

The decay rate is calculated with the m_{ν_τ} dependent correction functions ξ_μ and ξ_e from section 1.6 for the leptonic τ decays. The measured total leptonic τ decay rate and also the prediction as a function of m_{ν_τ} are shown in figure 8.6.

Assuming that the errors on Γ are Gaussian and that $m_{\nu_\tau} \geq 0$, a 95% confidence limit on m_{ν_τ} is defined by the point at which the calculated rate intersects the 1.6 σ contour for the measurement. From the intersection point it follows that:

$$m_{\nu_\tau} < 107 \text{ MeV} \tag{8.22}$$

This indirect limit is significantly higher than the best direct limit of $m_{\nu_\tau} < 18.2$ MeV from a measurement of the ALEPH collaboration [99] using a different method.

8.5 Mass of a charged Higgs Boson

From the measured leptonic branching fractions a limit on the mass of a charged Higgs boson is derived. The ratio g_μ/g_e is predicted from equation 1.60 as a function of $m_H/\tan\beta$ and the χ^2 is calculated for the measured ratio of the couplings.

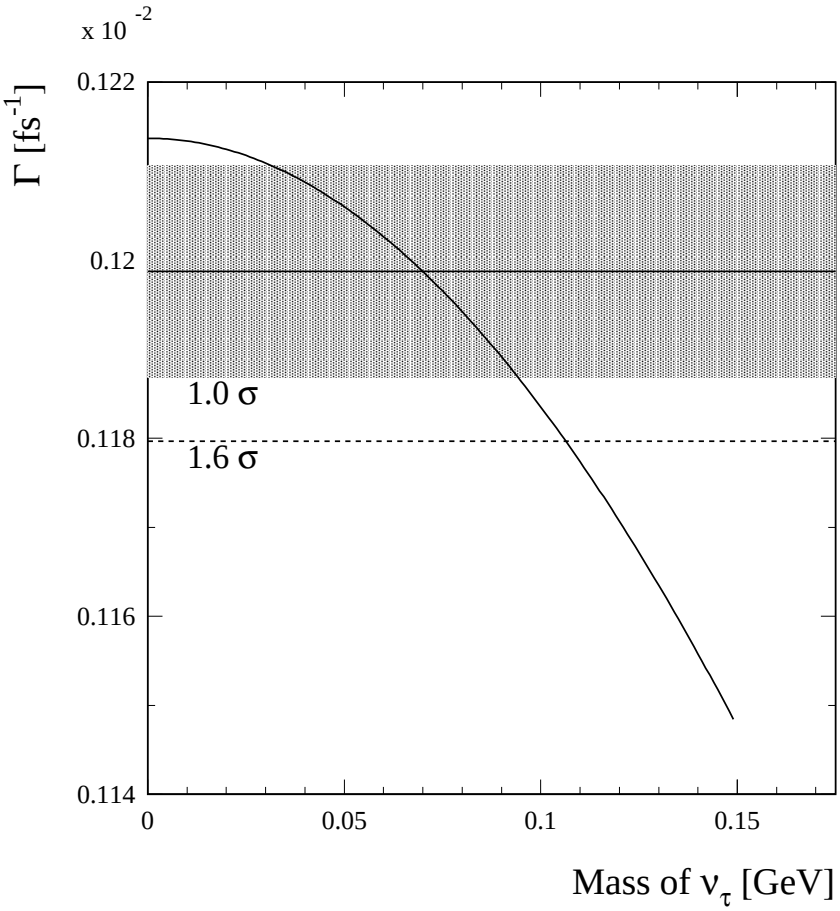

Fig. 8.6: Observed total leptonic τ decay rate displayed as the solid horizontal line. The hatched area corresponds to the ± 1 σ contour and the dashed line indicates the 1.6 σ value. The curve represents the calculated leptonic decay rate as a function of m_{ν_τ}.

A limit on the mass of the charged Higgs is obtained at 95% confidence level to

$$m_H^{\pm} > 1.0 \tan\beta \text{ GeV} \quad . \tag{8.23}$$

It is competitive with direct measurements[1] only for large values of $\tan\beta$.

8.6 Comparison with other Experiments

Although this measurement allows already highly precise tests of lepton universality, the precision of the test can be increased by combining this measurement with measurements at other experiments. Combining the results of the four LEP experiments [56, 101–103] allows to measure the branching fractions with twice as good precision as every single experiment. The central values and the errors obtained by the experiments are in good agreement (figures 8.7 and 8.8), stating the fact that all LEP experiments have the same capability to measure τ leptonic branching fractions.

The combinend result is in good agreement with the world average from [4]:

$$\begin{aligned} B_e &= (17.78 \pm 0.08)\% \\ B_\mu &= (17.32 \pm 0.09)\% \ , \end{aligned}$$

but considerably more precise.

[1] Direct searches at L3 exclude the region of $m_H < 65.5$ GeV for all values of $\tan\beta$ [100].

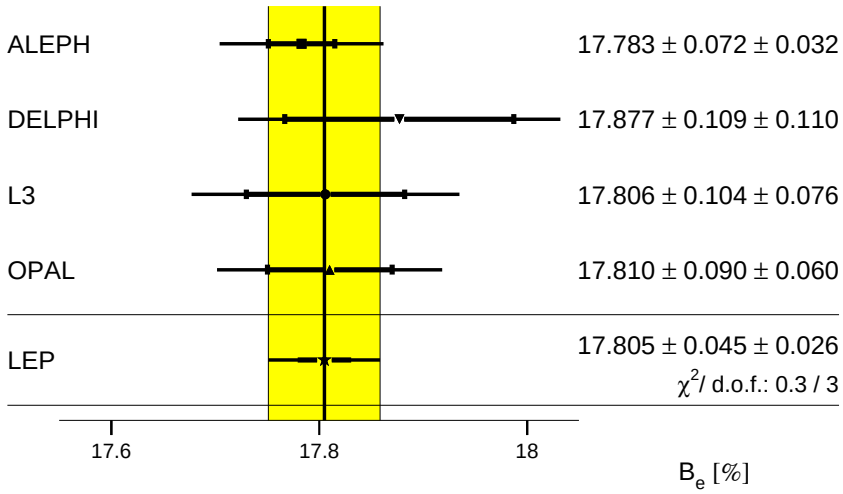

Fig. 8.7: Combination of B_e measurements at LEP. The results for ALEPH, DELPHI and OPAL are taken from [56, 101–103].

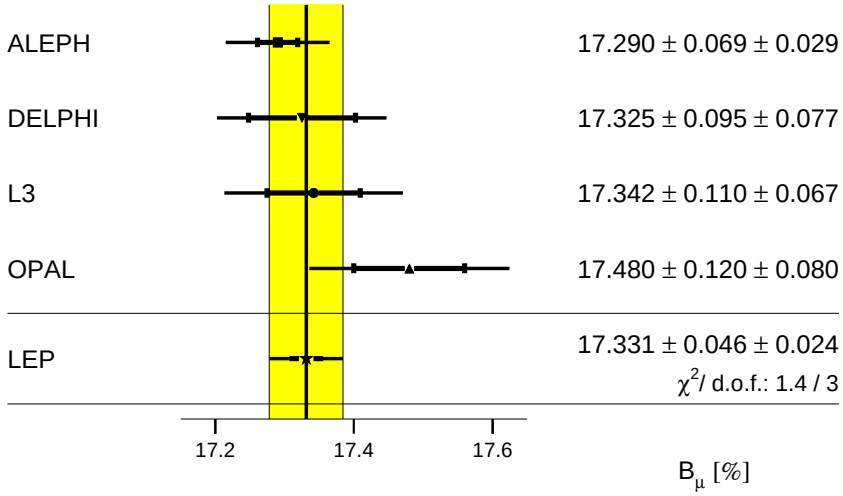

Fig. 8.8: Combination of the B_μ measurements at LEP. The results for ALEPH, DELPHI and OPAL are taken from [56, 101–103].

Chapter 9

SUMMARY AND CONCLUSION

The work presented in this thesis is the first measurement of the τ leptonic branching fractions with the L3 detector using the full LEP I data collected at centre-of-mass energies around the Z resonance. From a sample of 163256 τ pairs produced in the process $e^+e^- \to \tau^+\tau^-$ the decays $\tau \to e\bar{\nu}\nu$ and $\tau \to \mu\bar{\nu}\nu$ are identified and the leptonic branching fractions are obtained:

$$\begin{aligned} B_e &= (17.806 \pm 0.104_{stat} \pm 0.076_{sys})\% \\ B_\mu &= (17.342 \pm 0.110_{stat} \pm 0.067_{sys})\% \ . \end{aligned}$$

The measurement is based on the idea of hemisphere tagging, where the selection criteria are applied to one of the pairwise produced τ leptons only, while the lepton identification is carried out for the remaining τ decay. Together with a careful study of the efficiencies and background fractions on reference data samples the hemisphere tagging reduces systematic errors.

From the ratio of the measured branching fractions an estimate of the ratio between the electron and the muon couplings to the charged weak current is obtained:

$$\frac{g_\mu}{g_e} = 1.0007 \pm 0.0051 \ ,$$

confirming very precisely the Standard Model assumption of unity.

Together with the L3 measurement of the τ lifetime, the universality of the $\tau - e$ and $\tau - \mu$ charged current couplings is tested:

$$\begin{aligned} \frac{g_\tau}{g_\mu} &= 0.9955 \pm 0.0056 \\ \frac{g_\tau}{g_e} &= 0.9962 \pm 0.0057 \ . \end{aligned}$$

Lepton universality in the weak charged current is verified at a level better than 6 per mille.

The τ lifetime, predicted from the measured leptonic branching fractions, is in very good agreement with direct measurements, thus confirming the Standard Model.

From the ratio of the hadronic to leptonic τ decay width, calculated using the measured leptonic branching fraction, a value of the strong coupling constant is extracted:

$$\alpha_s(m_\tau) \;=\; 0.324 \;\pm\; 0.009_{exp} \;\pm\; 0.017_{theory} \;.$$

This value is evolved to the Z mass scale by applying the renormalisation group equations:

$$\alpha_s(m_{\mathrm{Z}}) \;=\; 0.1191 \;\pm\; 0.0009_{exp} \;\pm\; 0.0019_{theory} \;.$$

Both values are in good agreement with other measurements and confirm the running of α_s as predicted from QCD.

A limit for the ν_τ mass is estimated from the total leptonic decay rate m_{ν_τ}:

$$m_{\nu_\tau} \;<\; 107 \text{ MeV} \qquad \text{(at 95\% confidence level)} \;.$$

Finally, the ratio of g_μ/g_e is used to extract a limit on the mass of the charged Higgs boson:

$$m_{H^\pm} > 1.0 \tan\beta \text{ GeV} \qquad \text{(at 95\% confidence level)} \;.$$

This limit is competitive with direct searches for large values of $\tan\beta$.

The measured τ leptonic branching fractions are in good agreement with the world averages, which are dominated by the LEP experiments. Since the LEP I data is almost completely analysed it is unlikely that the measurements of the leptonic branching fractions will improve in the very next future.

New high luminosity e^+e^- colliders with centre-at-mass energies around 10 GeV have already started or will start soon operation. At design luminosities, these experiments expect to collect between 10^7 an 10^8 τ pair events per year. These high luminosities will make it possible to continue precision physics made with τ decays.

LIST OF FIGURES

1.1 The τ lepton as Standard Model laboratory 13
1.2 Tree level Feynman diagram of the process $e^+e^- \to \tau^+\tau^-$. 14
1.3 Feynman diagram for the leptonic τ decay. 17
1.4 The correction ξ_l as a function of m_{ν_τ} 22
1.5 Leptonic τ decay mediated by Higgs exchange. 23

2.1 The LEP site 26
2.2 A perspective view of the L3 detector 28
2.3 The central tracking system 29
2.4 A perspective view of the SMD 30
2.5 The L3 tracking system 31
2.6 The electromagnetic calorimeter 33
2.7 The hadron calorimeter 35
2.8 Layout of a muon spectrometer octant 36
2.9 Illustration of the sagitta method 37

3.1 The electron signature in the L3 detector 45
3.2 The muon signature in the L3 detector 45

4.1 The single hemisphere tagging method 53

5.1 A $\tau\tau$ event seen in L3 57
5.2 Reconstruction of cosmic muons 59
5.3 The maximum opening angle 60
5.4 The acollinearity distribution after preselection 61
5.5 The acoplanarity distribution after preselection 61

5.6 The DCA distribution after preselection 63
5.7 The ECAL bump energy of the leading track 64
5.8 The cut on acoplanarity for loose electrons 66
5.9 Momentum of the most energetic muon triplet 66
5.10 Momentum of the most energetic muon doublet 67
5.11 The ECAL bump energy for electron-like τ decays 72
5.12 The muon chamber momentum for muon-like τ events 72
5.13 The calorimetric energy for the τ sample 73

6.1 $\phi_{\mathrm{CTS}} - \phi_{\mathrm{ECAL}}$ for Bhabha events 76
6.2 $|\phi_{\mathrm{CTS}} - \phi_{\mathrm{ECAL}}|$ for the τ sample 77
6.3 The ratio E^9_{ECAL}/E^{25}_{ECAL} for the Bhabha sample 78
6.4 The ratio $\mathrm{E}^9_{\mathrm{ECAL}}$ /$\mathrm{E}^{25}_{\mathrm{ECAL}}$ for the τ sample 79
6.5 χ^2_{em} for the τ sample 79
6.6 $|\phi_{\mathrm{CTS}} - \phi_{\mathrm{MCH}}|$ for the τ sample 81
6.7 ECAL energy for dimuon events 82
6.8 ECAL energy for τ sample 82
6.9 HCAL energy outside MIP expectation 83
6.10 Energy depositions of Z $\rightarrow \mu^+\mu^-$ events 84
6.11 MIP signal for τ sample 84
6.12 The compatibility between CTS and ECAL measurements 86

7.1 The Bhabha background in the τ sample 90
7.2 The background from $\mathrm{e^+e^-} \rightarrow \mu^+\mu^-$in the τ sample 91
7.3 Energy for high multiplicity τ events. 92
7.4 Identification efficiency for $\tau \rightarrow e\bar{\nu}\nu$. 94
7.5 Electron identification for Bhabha events 95
7.6 Electron identification for $\mathrm{e^+e^-} \rightarrow \mathrm{e^+e^-}$ $\mathrm{e^+e^-}$ events 96
7.7 Electron identification for radiative Bhabha events 99
7.8 Identification efficiency for $\tau \rightarrow \mu\bar{\nu}\nu$ 100
7.9 Muon identification for $\mathrm{e^+e^-} \rightarrow \mu^+\mu^-$events 101

7.10 Muon identification for $e^+e^- \to e^+e^- \mu^+\mu^-$events 102
7.11 Muon identification for radiative $e^+e^- \to \mu^+\mu^-$ events 104
7.12 Energy distribution for events identified as $\tau \to e\bar{\nu}\nu$ 113
7.13 Momentum distribution for events identified as $\tau \to \mu\bar{\nu}\nu$ 114

8.1 Measurements of the branching fractions for $\tau \to e\bar{\nu}\nu$. 121
8.2 Measurements of the branching fractions for $\tau \to \mu\bar{\nu}\nu$. 121
8.3 Universality of the leptonic branching fractions 122
8.4 The τ lifetime predicted from the leptonic branching fraction 124
8.5 The relation between τ lifetime and leptonic branching fraction 125
8.6 Observed total leptonic τ decay rate 128
8.7 Combination of the B_e measurements at LEP 130
8.8 Combination of the B_μ measurements at LEP 130

LIST OF TABLES

1.1 Fundamental fermions in the Standard Model 6

1.2 Gauge bosons of the Standard Model 6

1.3 The fermions in the Electroweak Standard Model 8

1.4 The hadronic τ decay modes 13

4.1 Error of the branching fraction 50

5.1 The dedicated correlated cuts against Bhabha events 65

5.2 The dedicated correlated cuts against dimuon events 68

5.3 The dedicated correlated cut against $e^+e^- \to e^+e^-\ e^+e^-$ 69

5.4 The dedicated correlated cut against $e^+e^- \to e^+e^-\ \mu^+\mu^-$ 70

7.1 Identification efficiencies for $\tau \to e\bar{\nu}\nu$ events 97

7.2 Electron identification efficiency corrections 98

7.3 Identification efficiency for $\tau \to \mu\bar{\nu}\nu$ events 103

7.4 Muon identification efficiency correction 103

7.5 Summary of the background systematics for the τ sample 107

7.6 Selection bias 109

7.7 Summary of the background contributions for the τ sample 111

7.8 Summary of the τ selection 111

7.9 Background for the $\tau \to e\bar{\nu}\nu$ and $\tau \to \mu\bar{\nu}\nu$ samples 112

7.10 Summary for the leptonic τ decays 115

7.11 Summary of the uncorrelated systematics for B_e 116

7.12 Summary of the correlated systematics for B_e 116

7.13 Summary of the uncorrelated systematics for B_μ 117

7.14 Summary of the correlated systematics for B_μ 117
7.15 Summary of the correlated systematics 118

8.1 The τ leptonic branching fraction measurements 119
8.2 Theoretical uncertainties on $\alpha_s(m_\tau)$ and $\alpha_s(m_Z)$ 126

BIBLIOGRAPHIC NOTES

[1] A. Salam and J.C. Ward, Phys. Lett. **13** (1964) 168–171.

[2] S.L. Glashow, Nucl. Phys. **22** (1961) 579.

[3] S. Weinberg, Phys. Rev. Lett. **19** (1967) 1264.

[4] C. Caso *et al.*, The European Physical Journal **C3** (1998) 1 and 1999 off-year partial update for the 2000 edition available on the PDG WWW pages (URL: http://pdg.lbl.gov/).

[5] G. 't Hooft, Nucl. Phys. **B35** (1971) 167–188.

[6] G. 't Hooft and M. Veltman, Nucl. Phys. **B44** (1972) 189–213, Nobel Prize in Physics 1999.

[7] ed. T. Kinoshita, *Quantum electrodynamics*, 1990, Singapore, World Scientific 997 (Advanced series on directions in high energy physics, 7).

[8] N. Cabibbo, Phys. Rev. Lett. **10** (1963) 531.

[9] M. Kobayashi and T. Maskawa, Prog. Theor. Phys. **49** (1973) 652.

[10] P.W. Higgs, Phys. Lett. **12** (1964) 132.

[11] P.W. Higgs, Phys. Rev. Lett. **13** (1964) 508.

[12] The LEP Working Groups for Higgs Boson Searches, *LEPC meeting: Report from the LEP Higgs Working Group. Preliminary combined results from the four LEP experiments, September, 1999.*

[13] E. Gildener, Phys. Rev. **D14** (1976) 1667.

[14] E. Gildener, Phys. Lett. **92B** (1980) 111.

[15] G. Altarelli, *The Standard electroweak theory and beyond*, hep-ph/9811456, 1998.

[16] J. Ellis, *Beyond the standard model for hill walkers*, hep-ph/9812235, 1998.

[17] S. L. Glashow and J. Iliopoulos and L. Maiani, Phys. Rev. **D2** (1970) 1285.

[18] J.J. Aubert and others, Phys. Rev. Lett. **33** (1974) 1404.

[19] J.E. Augustin and others, Phys. Rev. Lett. **33** (1974) 1406–1408.

[20] Y. Tsai, Phys. Rev. **D4** (1971) 2821.

[21] H.B. Thacker and J.J. Sakurai, Phys. Lett. **36B** (1971) 103–105.

[22] M. Bernardini *et al.*, Nuovo Cim. **17A** (1973) 383.

[23] M.L. Perl *et al.*, Phys. Rev. Lett. **35** (1975) 1489.

[24] M.W. Grünewald, Phys. Scripta **53** (1996) 257.

[25] S. Gentile and M. Pohl, Phys. Rept. **274** (1996) 287–376.

[26] J.H. Kuhn, *The Tau lepton: Particle physics in a nutshell*, hep-ph/9812399, 1998.

[27] A. Pich, *Tau physics*, hep-ph/9704453, 1997.

[28] eds. A. Pich and A. Ruiz, *Tau lepton physics. Proceedings, 5th Workshop, Tau 98, Santander, Spain, September 14-17, 1998*, 1999.

[29] J.Z. Bai and others, Phys. Rev. **D53** (1996) 20–34.

[30] eds. G. Altarelli, R. Kleiss, C. Verzegnassi, *Z Physics At Lep 1. Proceedings, Workshop, Geneva, Switzerland, September 4-5, 1989. Vol. 1: Standard Physics*, Geneva, Switzerland: CERN (1989) 453 p.

[31] The LEP Electroweak Working and SLD Heavy Flavour and Electroweak Groups, *A Combination of Preliminary Electroweak Measurements and Constraints on the Standard Model. by M. Acciarri*, Preprint (CERN-EP-99-015), 1999.

[32] W.J. Marciano and A. Sirlin, Phys. Rev. Lett. **61** (1988) 1815.

[33] E. Fermi, Z. Phys. **88** (1934) 161–177.

[34] T. Kinoshita and A. Sirlin, Phys. Rev. **113** (1959) 1652–1660.

[35] A. Sirlin, Rev. Mod. Phys. **50** (1978) 573.

[36] T. Riemann, *Private Communication*, Letter to W. J. Marciano, 1998.

[37] W.J. Marciano, *Tau physics: A Theoretical perspective*, Talk given at 3rd Workshop on Tau Lepton Physics, Montreux, Switzerland, 19-22 Sep 1994.

[38] W.J. Marciano, *Fermi constants and 'New Physics'*, hep-ph/9903451, 1999.

[39] S.M. Berman and A. Sirlin, Ann. Phys. **20** (1962) 20–43.

[40] A. Pich, *Effective field theory: Course*, hep-ph/9806303, 1998.

[41] T. van Ritbergen and R.G. Stuart, *On the precise determination of the Fermi coupling constant from the muon lifetime*, hep-ph/9904240, 1999.

[42] E. Braaten, Phys. Rev. Lett. **60** (1988) 1606.

[43] E. Braaten, Phys. Rev. **D39** (1989) 1458.

[44] F. Le Diberder and A. Pich, Phys. Lett. **B286** (1992) 147–152.

[45] E. Braaten and S. Narison and A. Pich, Nucl. Phys. **B373** (1992) 581–612.

[46] E. Braaten and C. Li, Phys. Rev. **D42** (1990) 3888–3891.

[47] A.L. Kataev and V.V. Starshenko, Mod. Phys. Lett. **A10** (1995) 235–250.

[48] M. Neubert, Nucl. Phys. **B463** (1996) 511–546.

[49] R. Barate *et al.*, Eur. Phys. J. **C4** (1998) 409.

[50] K. Ackerstaff *et al.*, Eur. Phys. J. **C7** (1999) 571.

[51] M. Nakahata, Nucl. Phys. Proc. Suppl. **76** (1999) 425.

[52] A. Colijn, *Measurement of the tau lepton lifetime. Doctoral Thesis*, to be published in Phys. Lett., 1999, NIKHEF.

[53] A. Stahl, Nucl. Phys. Proc. Suppl. **76** (1999) 173.

[54] B. McWilliams and L. Li, Nucl. Phys. **B179** (1981) 62.

[55] H.E. Haber, *Can the higgs sector be probed in tau lepton decays?*, Proceedings of Tau Charm Workshop, Stanford, CA, May 23-27, 1989.

[56] B. Stugu, *Summary on tau leptonic branching ratios and universality*, hep-ex/9811048, 1998, Talk given at 5th Workshop on Tau Lepton Physics (Tau '98), Santander, Spain, September 14-17, 1998.

[57] G.-A. Voss ed. by H.B. Newman, T. Ypsilantis, NATO Asi Series. Series B, Physics **352** (1996) 465–485.

[58] M. Tigner, Nuovo Cim. **37** (1965) 1228–31, Letter to the editor.

[59] LEP Design report, CERN-LEP/TH/84-01 **II** (1984).

[60] LEP Design report, CERN-LEP/TH/83-29 **I** (1983).

[61] D. Decamp *et al.*, Nucl. Instrum. Meth. **A294** (1990) 121–178.

[62] P. Aarnio *et al.*, Nucl. Instrum. Meth. **A303** (1991) 233–276.

[63] L3 collaboration, B. Adeva *et al.*., Nucl. Instrum. Methods **A 289** (1990) 35.

[64] K. Ahmet *et al.*, Nucl. Instrum. Meth. **A305** (1991) 275–319.

[65] L3 collaboration, *Technical Proposal*, 1983.

[66] M. Acciarri *et al.*, Nucl. Instrum. Meth. **A351** (1994) 300–312.

[67] A. Adam *et al.*, Nucl. Instrum. Meth. **A348** (1994) 436.

[68] F. Beissel *et al.*, Nucl. Instrum. Meth. **A332** (1993) 33.

[69] K. Deiters *et al.*, Nucl. Instrum. Meth. **A323** (1992) 162.

[70] R. Sumner, Nucl. Instrum. Meth. **A265** (1988) 252.

[71] J. A. Bakken *et al.*, Nucl. Instr. Meth. **A254** (1987) 535.

[72] C. Caso *et al.*, Eur. Phys. J. **C3** (1998) 156.

[73] O. Adriani *et al.*, Nucl. Instrum. Meth. **A302** (1991) 53–62.

[74] G. Chiefari *et al.*, Nucl. Instrum. Meth. **A277** (1989) 187.

[75] B. Adeva *et al.*, Nucl. Instrum. Meth. **A323** (1992) 109.

[76] M. Fabre, *The dimuon mass resolution of the L3 experiment at LEP and its depence on the muon spectrometer alignment, Doctoral Thesis*, 1992, ETH-Zürich.

[77] U. Uwer, *Messung der Myonpaarproduktion auf der Z-Resonanz, Doctoral Thesis*, 1994, RWTH-Aachen.

[78] I.C. Brock *et al.*, Nucl. Instrum. Meth. **A381** (1996) 236–266.

[79] S. Myers, *The LEP collider, from design to approval and commissioning, Nov 26, 1990*, Presented at CERN Accelerator School: The LEP Collider from Design to Approval and Commissioning, Geneva, Switzerland, Nov 26, 1990, CAS: CERN accelerator school, 6th John Adams Memorial lecture.

[80] R. Bizzarri *et al.*, Nucl. Instrum. Meth. **A283** (1989) 799.

[81] P. Bagnaia and R. Bizzarri and F. Cesaroni and S. Gentile and G. Lunadei, Nucl. Instrum. Meth. **A323** (1992) 528.

[82] R. Bizzarri, F. Cesaroni, S. Gentile, G. Lunadei, M. Fukushima and T. Hebbeker, Nucl. Inst. Meth. **A 317** (1992) 463.

[83] P. Bene *et al.*, Nucl. Instrum. Meth. **A306** (1991) 150–158.

[84] S.P. Beingessner *et al.*, Nucl. Instrum. Meth. **A340** (1994) 322–327.

[85] C. Dionisi *et al.*, Nucl. Instrum. Meth. **A336** (1993) 78.

[86] S. Jézéquel and Y. Karyotakis, *Results of the χ^2_{BGO} method for the selection of the electromagnetic bumps*, L3 Internal Note 1272, 1992.

[87] The L3 detector simulation is based on the GEANT 3 program. (R. Brun *et al.*, CERN report DD/EE/84-1).

[88] W.T. Eadie, D.Drijard, F.James, M.Roos, and B.Sadoulet, *Statistical Methods in Experimental Physics*, 1971, North-Holland.

[89] M. Acciarri *et al.*, Phys. Lett. **B429** (1998) 387.

[90] C. Caso *et al.*, Review of Particle Physics, Eur. Phys. J. **C3** (1998) 1.

[91] S. Wynhoff, *Messung der Tau-Paarproduktion mit dem L3-Detektor bei LEP*, 1997, RWTH Aachen, Doctoral Thesis.

[92] L. Malgeri, *Misura della sezione d'urto e dell'asimmetria di carica del processo e+e- to tau+tau-(gamma) nell'esperiment o L3 al LEP. Doctoral Thesis*, 1999, University Rom.

[93] O. Adriani and others, Phys. Rept. **236** (1993) 1–146.

[94] L3, Tau leptonic branching fractions from L3, 1994, Talk given at 3nd Workshop on Tau Lepton Physics (Tau 94), Montreux, Switzerland, 19-22 September.

[95] L3, Measurement of the Branching Ratios of the Tau into Leptons with the L3 detector at LEP, 1996, Talk given at 4th Workshop on Tau Lepton Physics (Tau 96), Colorado, USA, 16-19 September.

[96] P.A. Raczka, Phys. Rev. **D57** (1998) 6862–6870.

[97] H. Arason and others, Phys. Rev. **D46** (1992) 3945.

[98] G. Rodrigo and A. Pich and A. Santamaria, Phys. Lett. **B424** (1998) 367–374.

[99] ALEPH collaboration, Nucl. Phys. Proc. Suppl. **66** (1998) 214.

[100] A. Kopp, *Search for Higgs Bosons using the L3 Detector at LEP. Doctoral Thesis*, 1999, DESY Zeuthen.

[101] H. Videau *et al.*, *Measurement of the tau leptonic branching ratios at LEP I*, Preprint, ALEPH, 1999, CERN-OPEN-99-258.

[102] DELPHI collaboration, P. Abreu *et al.*, Eur. Phys. J. **C10** (1999) 201.

[103] OPAL collaboration, G. Abbiendi *et al.*, Phys. Lett. **447** (1999) 134–146.

ACKNOWLEDGEMENTS

Even if I, naturally, had to do the work of this thesis, it is based on the effort of the many people which were and are the L3 collaboration. A few of these people I want to thank in particular.

My special thank goes to T.Hebbeker, my research supervisor from the Humboldt University in Berlin, for his assistance. I thank my advisor W.Lohmann for encouraging me to start this analysis and for his support over the whole time. He was always open to my problems. I am indebted to DESY for giving my the possibility to work at the L3 experiment and to stay at CERN for a long time.

I would like to thank all people from the τ analysis group. I benefit from their effort to understand the L3 detector for its use in e τ physics. In particular I thank Ivan Korolko. His experiences were enormously helpful when I started this measurement. I want to thank Auke Pieter for collaborating in a minimal Tau working group.

I am grateful to all my colleagues from DESY Zeuthen and Humboldt University for their support and continuing interest in my analysis. The good private contact to the other PhD students helped me to solve many problems and was always very encouraging.

Thanks to my parents and especially to Michèle. I will never try her patience with writing a PhD thesis again.

Selbständigkeitserklärung

Hiermit erkläre ich, daß ich diese Dissertation selbständig erarbeitet und verfaßt habe und keine anderen als die angegebenen Hilfsmittel verwendet habe.

Frank Ziegler